

**3-DIMENSIONAL DYNAMICS OF THE
GALACTIC BULGE**

3-DIMENSIONAL DYNAMICS OF THE GALACTIC BULGE

Proefschrift

ter verkrijging van
de graad van Doctor aan de Universiteit Leiden,
op gezag van de Rector Magnificus prof. dr. P. F. van der Heijden,
volgens besluit van het College voor Promoties
te verdedigen op woensdag 24 maart 2010
te klokke 16.15 uur

door

Mario Humberto Soto Vicencio

geboren te Santiago, Chile
in 1979

Promotiecommissie

Promotor:	Prof. dr. K. Kuijken	(Sterrewacht Leiden)
Co-promotor:	Dr. J. Lub	(Sterrewacht Leiden)
Co-promotor:	Dr. R.M. Rich	(UCLA)
Overige leden:	Prof. dr. T. de Zeeuw	(ESO - Sterrewacht Leiden)
	Prof. dr. M. Franx	(Sterrewacht Leiden)
	Dr. A. Brown	(Sterrewacht Leiden)
	Dr. H. Zhao	(St. Andrews)

Para mi Boni, la Latoncita,
la Xime, la Doshi, la Vieja y el Manuel.

Contents

1	Introduction	1
1.1	An historical overview	1
1.2	Modern conception of the Milky Way	8
1.2.1	The Milky Way as a barred galaxy	8
1.2.2	Bar evolution	11
1.2.3	Modeling the dynamics of the Milky Way	12
1.3	This thesis	13
1.4	Future prospects	16
2	Radial Velocities for 6 bulge fields: Procedures and results	21
2.1	Introduction	22
2.2	Project	23
2.3	Observations and procedures	24
2.3.1	Proper motions	24
2.3.2	Radial Velocities	24
2.3.3	Zero-point Velocity Corrections	33
2.4	Analysis	34
2.4.1	Velocity results in fields close to the galactic minor axis and off-axis fields	34
2.5	Conclusions	41
3	Evidence of a Metal Rich Galactic Bar from the Vertex Deviation of the Velocity ellipsoid	45
3.1	Introduction	46
3.2	Analysis	47
3.3	Discussion	50
4	A Schwarzschild model for three minor-axis fields	53
4.1	Introduction	54
4.2	Modeling technique	56
4.2.1	Formulation	56
4.3	Deprojecting the bulge density distribution from the COBE map once again	57
4.3.1	Deprojection by analytical bars	58

4.3.2	Potential formulation	61
4.3.3	Orbit library	63
4.4	Schwarzschild Models	66
4.4.1	Proper motions and Photometric parallax	67
4.5	Results of the Schwarzschild technique	68
4.6	Summary and Future Work	76
4.6.1	Future improvements in the model	79
4.A	Building the COBE/DIRBE image	84
4.B	Deprojection by multipolar expansion	85
5	Stellar proper motions in three off-axis galactic bulge fields	89
5.1	Introduction	90
5.2	Observations	92
5.3	Proper motion measurements	94
5.4	Analysis	98
5.4.1	NGC 6656 results	102
5.4.2	A bulge sample kinematically selected	104
5.5	Conclusions	106
	Outlook	109
	Nederlandse samenvatting	111
	Resumen en Español	116
	Curriculum Vitae	123
	Acknowledgments	124

CHAPTER 1

Introduction

The history of the development of the understanding of the Milky Way as a galaxy, is also the history of the mankind's knowledge in astronomy. Many discoveries and advances that for many years seemed to concern topics not directly related to our galaxy, turned out to be important contributions to our knowledge of the Milky Way in the end. Nowadays, in spite of the enormous advances in theory and techniques, the Milky Way still maintains some of its secrets. In this chapter, we deliver a short review of the history of discoveries more directly related with the Milky Way, and the principal actors involved on it.

1.1 AN HISTORICAL OVERVIEW

From Galileo to Sapley's model of the galaxy

The name "Milky Way" given to our galaxy, comes from the literal translation of the Latin "Via Lactea", which is precisely in Greek the word for *galaxy*. The early conceptions of the Milky Way took a more solid consistency when Galileo, helped by his reinvention of the telescope during the XVIIth century, was able to resolve for the first time the Milky Way into separate stars. Until then, the Milky Way was thought to be nebulous structure. The fact that the Milky Way was an association of stars, did not have a strong bearing in the Aristotelian cosmology, which was the general conception of the epoch. Nevertheless, in spite of this change in the ideas driven by the new evidence, it was not until the next century that these new ideas about the Milky Way prompted another significant change.

Thomas Wright from Durham, in the mid eighteenth century, was a clockmaker who taught himself practical astronomy effectively enough to teach navigation and to work as a land surveyor. In 1742, Wright published '*Key to Heavens*' a volume explaining his ideas of the Universe. Nevertheless, it was not until 1750 that he presented his most influential work, *An Original Theory or New Hypothesis of the Universe*. Wright always tried to maintain a strong religious dimension in his models. The heavens, according to him, were the proof of God's magnificent work.

In his model of 1750, the observed Universe was thought to be a combination of two

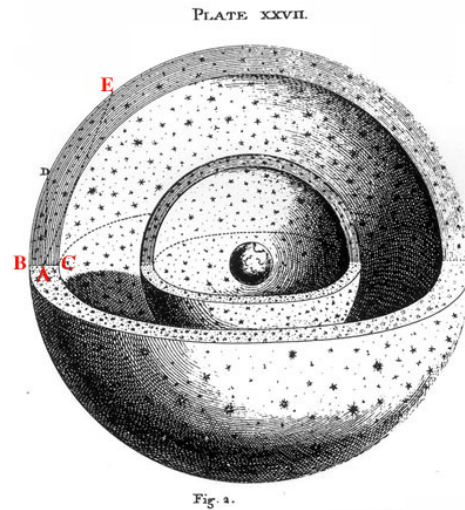


Figure 1.1: Wright's model of the Milky Way. *An original Theory of the Universe* (1750).

thin concentric spherical shells (Fig. 1.1). Stars were distributed over these spherical shells, and thus, according to the viewing angle we could see some of observed characteristics of the Milky Way. The Sun in Wright's model was located halfway in the shell and hence looking along a tangent to the shell we would see a high concentration of stars, the sky in that direction would be filled with faint distant stars until just a diffuse glow was visible. On the other hand, an observer looking inwards or outwards in the thin portion of such universe, would see a sky sparsely populated in that direction. Hence, this model explained, to some extent, some of the observed properties of the Milky Way. The spherical symmetry for Wright was a natural consequence of God's handiwork. In addition, he postulated a divine center of the Universe, which was the point around which the stars, including the Sun, moved in orbits. It was this movement which prevented the collapse of the Universe under gravitation. Wright considered his model just one of the many possible. Other models he proposed pursued the idea of the spherical shells, but this time simplified to rings, which reproduced in a better way the observed properties of the Milky Way at the time. However, in all these models he maintained his religious conception of the divine center.

Wright later in his life changed many of his ideas about the Milky Way, this was illustrated in his manuscript "*Second thoughts*". It seems that he received a profound impression of different physical processes after the earthquake of Lisbon in 1755. And thus he changed his explanation of the Universe to an analogy of the earth's interior, with new stars as new volcanoes, and the Milky Way appearance as a result of a side-real flow of lava.

In spite of the change in his ideas in "*Second thoughts*", many of the Wright's initial concepts in his models were followed. Immanuel Kant (1704-1804) learned through a review of Wright's books. Kant, inspired by this review, which misunderstood some fundamental points of Wright's models, formulated his own ideas in *Universal Natural History and Theory of the Heavens*. The universe envisioned by Kant consisted of a disk of stars similar to the ring model of Wright. Kant also incorporated additional small el-

lenticular luminous patches, which at the time were known as “nebulous stars”. Kant’s model however did not explain the observed apparent absence of movements of stars. On the other hand, Kant considered that the normal matter as the Sun and planets might be created by condensation from primordial matter; where gravitational force played an important role allowing the thin diffuse matter to condense. Matter could thus form disks, and subsequently, larger bodies as the Sun, which in turn would evolve until it explodes and returns to the initial state of diffuse matter, in a cyclical process. Therefore, in Kant’s universe matter had a non-stationary state, which was against the philosophical point of view at the time.

Similarly to Kant’s ring model, Johann Heinrich Lambert (1728-1777) in his work *Cosmologische Briefe*, considered the Milky Way to be a convex lenticular structure, where the Sun and its neighborhood stars were just one of the many subsystems of the complete structure. At the same time, the Milky Way was part of a higher hierarchical system where many Milky Ways were included. Wright’s and Kant’s are essentially philosophical models, which were the response to the scarce scientific evidence of the Milky Way’s nature at the time. Lambert, on the other hand, who was a good mathematician, tried to find empirical equations to support his view of the universe for many years.

The first scientific research on the shape and size of the Universe which produced empirical evidence of the Milky Way’s structure was carried out by William Herschell, at the end of the eighteenth century. Herschell, who had the mightiest telescope of his time, first turned to the study of nebulae, discovering to his delight, that many of them were resolvable into multiple stars. He later discovered that many of the stars non-resolved were actually luminous gas. These results, which evidenced associations of stars in many nebulae, agreed well with the idea of gravitation drawing matter together and forming irregular patterns of stars as the ones observed.

In order to extend his understanding of the structure of the Milky Way, Hershel, by means of systematic methods, carried out a survey which consisted of extensive counts in 683 regions of the sky, these star counts he called “star-gauges”. His aim was to obtain an estimation of the shape of the Milky Way. Hershel, in the absence of knowledge on stellar distances made two important assumptions: he assumed that he could see the borders of the system, and that the stars in the latter were uniformly distributed. Even though Hershel knew his assumptions were just approximations, he believed they were enough to produce an acceptable representation of the Milky Way (see Fig. 1.2).

Notwithstanding, as the techniques of Hershel improved, he realized that many more stars were visible in each star-gauge, and therefore a uniform distribution was not possible. He found that stars were preferentially distributed in two opposite regions of the sky. Similarly, he found nebulae having the brightest patch in the middle and stars in resolvable clusters getting closer in the middle. Thus, later in his life, Hershel re-examined many of his postulates based on his early work. He recognized a preferred plane in which clusters of stars seemed to group. The star gauges of Hershel were continued by Otto Struve and also his own son John Hershel, who catalogued multiple new stars, nebulae and clusters, including observations in the southern hemisphere.

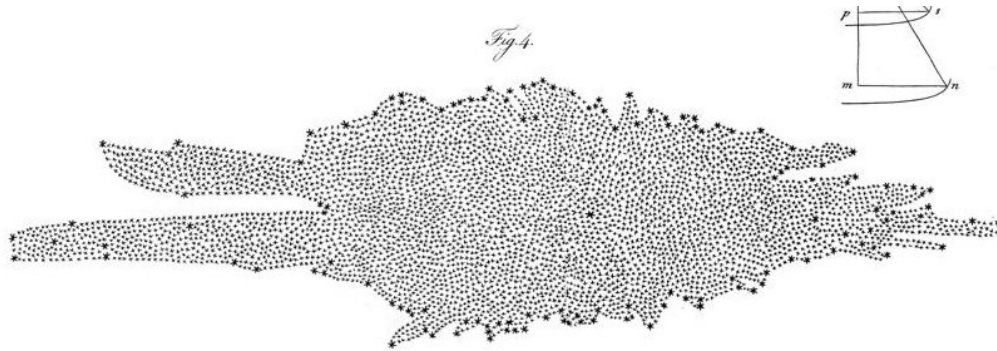


Figure 1.2: Hershel's model of the Milky Way based on star-gauges (M. Hoskin, *William Herschel and the Construction of the Heavens*, Oldbourne: London 1963).

Struve and John Hershel reached similar conclusions, particularly that the Sun was slightly to the north of the galactic plane.

William Parsons in 1845, armed with a superior telescope with a 72-inch mirror (more powerful than Hershel's) was able to resolve many of Hershel's nebulae a spiral structure. In addition, in some of these systems he was able to resolve individual stars. These observations supported the idea of "island universes" outside of our own galaxy and equivalent to it. The spiral shape, on the other hand, suggested rotation around a central axis, a hypothesis without proof until the beginning of the twentieth century.

At the end of the nineteenth and the beginning of the twentieth century the advent of photographic plates considerably improved the quality of observations. Photographs allowed the detection of thousands of individual objects in a single plate and the study of faint objects, never observed in detail before. Thus, taking advantage of the new technical development, Kapteyn, von Seelinger and van Rhijn started a plan to study 200 selected regions of the sky. Their study consisted of an international cooperation to collect plates in order to obtain stellar counts, brightness estimations and spectral classifications; this was the *Durchmusterung* catalogue. Kapteyn, von Seelinger, and van Rhijn used the information in the catalogue to produce a model of the Milky Way by assuming average distances for stars with the same apparent brightness levels. However, they were aware this last assumption probably was only statistically valid. Kapteyn's model made two more assumptions, apparent brightness falls off as the inverse of the square of the distance and the interstellar medium is completely transparent. The latter was a serious mistake, which perturbed significantly the determined structure of the model. Thus, the *Kapteyn Universe* was a flattened stellar system 10 kpc in diameter, and 2 kpc in thickness, where the Sun was located near the center.

Kapteyn soon realized that his model was extremely dependent on the assumption of a transparent interstellar medium. Any kind of absorption of the stellar light by an unknown medium would yield a misinterpretation of the distances. Absorption would make stars look dimmer and therefore they would seem to be farther than they actually are. The combined effect on the model would make the complete galaxy extend beyond its real limits. Aware of this serious dependence in his model, Kapteyn initiated many

studies in order to detect any possible interstellar absorption. Nevertheless, his results were inconclusive, and thus Kapteyn convinced himself that absorption if present was at least negligible and that his model was right to a reasonable degree.

Harlow Shapley was a young astronomer at Mount Wilson Observatory when he started to study globular clusters in 1914. Globular clusters are easily observed at great distances from the Sun due to their great brightness and appearance. Also, many of them are located at large distances above or below the galactic plane which make them less affected by the high absorption on the plane. Soon after he started, in 1915, Shapley noticed that globular clusters were inhomogeneously distributed over the sky. This distribution was symmetrical in galactic latitude below and above the galactic equator and favoured a particular direction, where globular cluster were evidently concentrated. Shapley realized that this distribution was characteristic of globular clusters, and thus he reasoned that if globular cluster, due to their size, were a important structural elements in the galaxy, they should be representative markers of the structure of the Milky Way. Hence, the apparent distribution of globular clusters must be a clear indication of the location of the Sun, which could not then be close to the center of the galaxy, as the Kapteyn Universe claimed, but rather quite far from it. The distances used by Shapley were obtained from the apparent brightness of variable stars as Cepheids, for which intrinsic brightness was known. Initially, accordingly to the size of the Kapteyn model, the distances found for the clusters placed them well beyond the limits of the galaxy. Shapley at first resolved this paradox by the combination of two systems, where the globular cluster were members of a second larger distribution than the galaxy. He later changed this position and boldly claimed that these globular clusters must be coupled to the Milky Way's structure and therefore the galaxy should be 10 times bigger than the size predicted by Kapteyn. This claim caused many controversies, since the Kapteyn Universe was already generally accepted. Thus, both models were disputed for several years by the astronomers. Shapley's estimated size for the Milky Way was somewhat too large mainly because of his assumption of negligible interstellar absorption.

Most of the opposition to Shapley's model was rooted in the belief that spiral nebulae were galaxies similar to the Milky Way. Heber D. Curtis from the Lick observatory was one of those antagonist to Shapley's ideas, he argued that if the spiral nebulae were galaxies of the size proposed by Shapley, they would necessarily have been inconceivably distant. Since there was no evidence that they were so distant, Shapley's conception had to be wrong. The discovery of novae in spiral nebulae by George Ritchey in 1917 gave for first time the possibility to obtain reliable estimations of the distances to the spirals. Where these distances clearly placed the spirals outside the limits of the Milky Way, Curtis calculated a typical distance of 1 Mpc for spiral nebulae. But while novae were used by Curtis to support the island universe concept and the Kapteyn model dimensions for the Milky Way, new proper motion results in novae were used against the latter. Because Adriaan van Maanen, in 1916, calculated the proper motions for several spiral nebulae and found, that if the these spiral were as distant as proposed by Curtis, their velocities were extremely large. Thus, two clearly opposite positions in astronomy coexisted at the time. Those favouring Shapley's model of the Milky

Way, which held that the dimensions of the Milky Way were directly related to the distribution of globular clusters, and those favouring Curtis' view, which supported the Kapteyn Universe dimensions and considered the spiral nebulae as extragalactic structures.

In this scenario both antagonist positions crashed in the "*great debate*" in the National Academy for Sciences in 1920. In it, Shapley and Curtis debated his respective positions about the size of the Milky Way and the nature of spiral nebulae. Even though the debate did not settle any of the questions addressed, it helped to bring to the attention of the scientific community the main problems of each theory. However, in the absence of crucial evidence, the opposing sides were not reconciled.

A few years after the debate, finally the nature of spiral nebulae was settled. Because Edward Hubble in 1923 could resolve with the new 100-inch telescope at Mount Wilson the outer regions of M31 and M33. And these regions proved to be very similar to those of group of stars previously resolved. Then when Cepheids stars were identified in both M31 and M33, a reliable distance estimation was possible by means of the Cepheid brightness-period relation. Thus, a value of 300 kpc was calculated for the distance to M31 and M33 .

After Shapley's model: Oort and Lindblad

At the same time, Jan Oort who dedicated several years to the study of high velocity stars, found several facts which were difficult to reconcile with Kapteyn's Universe. The distribution of high velocity stars seemed to have a clear asymmetry above 62 km/sec, where below that value random directions dominated. Under the Kapteyn Universe these high velocity stars could just belong to a different structure, dynamically decoupled from the galaxy. On the other hand, the limit of 62 km/sec implied an average radial velocity of 15 km/sec and a average mass of $5 M_{\odot}$. Another difficult fact to reconcile with Kapteyn's theory was that globular clusters, which typically have high velocities, could not be gravitationally bound to a galaxy as small as the one proposed by Kapteyn. Consequently, since globular clusters were very massive, it seemed quite unlikely that they would be created at a rate enough to replenish those escaped due to the high velocities, and the small escape velocity of the galaxy in Kapteyn's model. All this led to Oort to infer that the systematic high velocities in stars, an also in clusters, were associated with an intrinsic rotation around the galactic center.

It was Bertil Lindblad, a Swedish theorist, who connected all the facts in a coherent picture. Lindblad in 1926 proposed a model for the galaxy opposed to Kapteyn, in which the galaxy could be divided in several subsystems, each one of them with a particular rotation velocity, symmetric with respect the same galactic center. This differential rotation was responsible for the velocities observed in high velocity stars, globular cluster and RR Lyrae variables. Thus, the sun belonged to a subsystem which rotated in almost circular orbits around the galactic center with velocities around 200-300 km/sec. And therefore, all those so-called low-velocity stars, were actually stars in the same subsystem and probably in the solar neighborhood.

Soon after Lindblad's model was published, Oort found abundant observational data which supported the predictions in it (Oort 1927; 1928). Similarl to the explana-

tion of the low-velocity stars, he considered the high-velocity stars as members of a subsystem which essentially rotated at low velocity with respect to the galactic center, and at the same time have a large velocity difference with respect to the Sun. In addition, Oort calculated the consequences of galactic rotation in the solar neighborhood by means of some constants which reflected the observed radial velocities and proper motions in the galaxy. Other astronomers also found similar evidence in other samples. J.S. Plaskett and J.A. Pearce proved that movements in O and B type stars were consistent with the rotation of the Lindblad-Oort model. Subsequently Shapley's model of the Galaxy, and therefore the model of Lindblad and Oort, was generally accepted. However, in spite of the evidence, two important discrepancies in Shapley's model remained, the proper motions of spiral nebulae, and the scales and distances in Shapley's model. The key to the latter was the long sought absorption.

Hubble solved the inconsistency of proper motions in spirals in 1935, by re-measuring the original van Maanen data and adding new plates to his analysis. The measurements, carried out by himself, Baade and Nicholson, were in direct disagreement with van Maanen results. The conclusion was that van Maanen results were an artifact of the proper motion measurement, which was extremely complicated with the technology of the epoch. Hence, one of the principal arguments against the extragalactic nature of the spiral nebulae was over.

There was the general suspicion that some mechanism of absorption might be present in observations, the apparent structure of the Milky Way showed voids or obscure regions in which almost no stars were detectable. These areas devoid of stars were dynamically difficult to explain, since they implied the existence of numerous tunnel-shaped openings in the Galaxy. E.E. Barnard accumulated numerous plates showing such dark patches and lanes in the Milky Way at the beginning of the twentieth century. A majority of astronomers by 1920 accepted the presence of large clouds of obscuring matter in the galaxy, the matter of discussion then was the distribution of such matter. Indirect evidence of absorption appeared when Johannes Hartmann in 1904 noted that in a rapidly revolving binary star, δ Orionis, the ionized calcium lines Ca II did not participate in the generalized Doppler shift of the rest of the spectrum. Vesto M. Slipher found similar "stationary lines" in several other stars and thus concluded that these lines, stationary when measured with respect to the local system of stars, must have an interstellar origin outside the Solar System.

However, direct evidence of general absorption was not published until 1930 by R.J. Trumpler. Trumpler was an expert in globular clusters, and during his research had used two methods to determine distances to the clusters. The first method concerned the measurement of brightness and colour for the stars in the cluster by means of their spectral types. Then by plotting apparent brightness versus spectral type and comparing this plot with well known relations of intrinsic brightness versus spectral type (Hertzsprung-Russell diagram), for stars in the solar neighborhood, he was able to make estimations of the distance to the cluster. The second method, consisted of the inverse relation between distance and apparent size of the cluster, where he assumed that all the clusters analyzed had almost equal linear diameter, and therefore their angular size was simply a distance effect. The problem that faced Trumpler was that both

measures of distance were inconsistent. Clusters with large distances had angular diameters larger than expected. Tumbler discarded the possibility that clusters increased their size with the distance, and assumed that some kind of interstellar absorption of light had to exist. Finally he calculated that if the latter alternative was correct, an absorption of 0.67 mag/kpc was expected. In addition he proved the consistency of his argument with the observed increase in reddening of stars at any given color with the increase of distance.

Another important discovery in the picture of spirals (which were at this point accepted as peers of the Milky Way) was the separation in stellar populations. The notion of stellar populations was introduced by Walter Baade in 1944. Baade studied the nucleus of the spiral M31, its companions M32 and NGC 205 and two more ellipticals. He realized that the brightest stars in the spheroidal central region of M31 were red giants, in contrast to the dominating blue supergiants found in arms. Hence, Baade defined two distinct stellar populations: "*population I*", which consisted of young objects associated with spiral structures and therefore preferentially located in arms; and *population II*, which consisted of objects associated with the spheroidal component of the galaxies or globular clusters. Examples of population I are objects of a wide range of ages, such as young hot stars in OB associations, Cepheids, dust lanes and ionized Hydrogen regions. Population II, on the other hand, are mainly associated with the old stars found in globular clusters, haloes and bulges.

Finally, the discovery in 1940 of the 21-cm radio emission line of neutral Hydrogen, originating in the interstellar medium, has been used to map the rotation and structure of the Hydrogen in the galaxy. The structure of neutral atomic Hydrogen has been used as a tracer of galactic structure (e.g. Binney et al. 1991), and thus is of key importance to understanding the dynamics of the galactic center.

The picture of the Milky Way reached from the discoveries and technical advancements described in this section is one of a spiral galaxy as many others observed. This simple statement has less than 70 years of general consensus as we have seen, albeit, it does represent just the general characteristics of the Milky Way. This incomplete picture is still under development, and as we will see in the next section, many secondary features have been unveiled in the last years.

1.2 MODERN CONCEPTION OF THE MILKY WAY

1.2.1 The Milky Way as a barred galaxy

De Vaucouleurs (1964) was the first to suggest that the Milky Way is actually a barred galaxy. De Vaucouleurs was led to this conclusion after a detailed comparison with others spiral galaxies using 21-cm emission line data. The spiral multiplicity of the Milky Way resembled more closely that of barred galaxies. However, the highest deviation from an axisymmetric potential is observed in the center of the galaxy, and therefore it is in the galactic center where most of the bar features should be sought. Peters (1975), suggested a model for the inner regions of the galaxy which could reproduce the 3 kpc arm and the excess of velocity observed in emission of HI in the so-called

forbidden regions. This excess of velocity of $\sim 135 \text{ km sec}^{-1}$ could hardly be expected in an axisymmetric potential. Thus, the model suggested by Peters involved gas flowing along concentric elliptical streamlines such as might be caused by a bar structure. Nevertheless, in spite of the encouraging results just described, the use of the 21-cm emission line implies some disadvantages, such as low spatial resolution and diffuse 21-cm continuum emission. This can be partially solved by using emission lines from the less abundant abundant molecules, such as CO, CS, or OH. Binney et al. (1991) generated a model using the 21-cm, CO, and CS line information. In their model, the gas flow results showed a marked bar structure in the galactic center, with a corotation radius of $r = 2.4 \pm 0.5 \text{ kpc}$, a bar pattern speed of $63 \text{ km sec}^{-1} \text{ kpc}^{-1}$, and a bar inclination of $\phi_{bar} = 16 \pm 0.2^\circ$, with the closer end in the first galactic quadrant. According to the model, the CO emission arises in the places where gas is obliged to migrate from the $x1$ family of orbits to $x2$, which produce shocks that can be recognized in the (l, v) diagram. The $x1$ family of orbits are prograde along the bar, while $x2$ are perpendicular to the bar structure. Similarly, the ring of molecular gas detected was associated to the bar's outer Lindblad resonance, and the regions of low gas density inside 3.5 kpc with corotation. In addition, the advancement in the picture of the galactic bulge extends to other features. The centre itself which is associated with SgrA*, a radio source known for a long time, has been in the last decade proven to harbour a supermassive black hole of $(3.6 \pm 0.3) \times 10^6 M_\odot$ (Eisenhauer et al. 2005). The suspicion about the presence of a black hole in the galactic center had remained for years, proper motion measurements in the galactic center (even to radius as small as 0.01 pc) showed a excess of mass density of $\sim 10^{12} M_\odot \text{ pc}^{-3}$ (Ghez et al. 1998). Since a stellar cluster could not be responsible for such high mass, therefore, a black hole arose as the logical alternative. Eisenhauer et al. (2005), through detailed near-IR imaging spectroscopy, were able to obtain very accurate radial velocities and proper motions for 6 stars in the central $0.5''$, the orbits of these stars were consistent with the effect of a supermassive black hole.

Near infrared observations are generally the natural choice for studies of the galactic bulge, this is due to the diminished effect of extinction at those wavelengths compared with bluer filters. Several project have taken advantage of this characteristic to obtain reliable data of the galactic bulge. The Infrared Astronomical Satellite (IRAS), launched in 1983, yielded the first survey of the galactic bulge at these wavelengths. A few years later, the Infrared Telescope (IRT), flown aboard the Space Shuttle in 1985 as part of the Spacelab 2 mission, scanned a large fraction of the sky in several infrared wavelengths with a resolution of $\sim 1^\circ$. Its results were used by Kent, Dame & Fazio (1991) to obtain the three dimensional luminosity distribution of the Milky Way from a $2.4 \mu\text{m}$ map of the northern Galactic plane. Their results, however, were just fitted with axisymmetric distributions. On the contrary, Blitz & Spergel (1991) found abundant evidence for a galactic bar in the Matsumoto et al. (1982) IR data. The bar modeled was in the first galactic quadrant (the tip of the long end) and was consistent with previous predictions by Sinha (1979) and Liszt & Burton (1980), who first postulated a tilted bar to explain the observed kinematics of HI and CO. Blitz & Spergel (1991), however, were not able to constrain the tilt of the bar with their data. The most spectacular results regarding the galactic bar so far come from the Cosmic Background Explorer (COBE)

satellite. The COBE satellite produced low angular resolution maps of the Galactic bulge at 1.25, 2.2, 3.5 and 4.9 μm obtained from the Diffuse Infrared Background Experiment (DIRBE) instrument (Weiland et al. 1994). In such maps, after correction for extinction and subtraction of an empirical model for the galactic disk, clear asymmetries arose, which were consistent with a triaxial bulge. Similarly, Dwek et al. (1995), also using COBE DIRBE images, characterized the morphology and determined the infrared luminosity and mass for the galactic bulge. They adopted several triaxial analytical functions to represent the volume emissivity of the source, finding that a barlike structure provided the best fit to the data compared to axisymmetric bulge models. This Gaussian-type bar with a “boxy” geometry was aligned with the galactic plane, but rotated with its near-end in the first galactic quadrant at an angle of $20^\circ \pm 10^\circ$ with respect to Galactic center - Sun line, and axis ratio of $1 : 0.33 \pm 0.11 : 0.23 \pm 0.08$. In addition, combined with HST information, this bar model produced a photometric determination for the mass of the bulge of $\simeq 1.3 \times 10^{10} M_\odot$. Subsequent research focused on the COBE-DIRBE images produced deprojections of the 3-dimensional distribution of the bulge using several different techniques. Binney, Gerhard & Spergel (1997), used a non-parametric deprojection algorithm (Lucy’s method) for this purpose. Assuming 8-fold symmetry their model produced a bar with axis ratio 5:3:2 and a length of $\sim 1.8 kpc$, which in turn implies a corotation radius of $\sim 3 kpc$. More recently, Bissantz & Gerhard (2002), generated a new 3-D luminosity distribution for the inner Milky Way using a non-parametric penalized maximum-likelihood algorithm of deprojection. The algorithm also used as constraints the apparent magnitude (line-of-sight) distributions of clump giants, and included arms. This model thus led to a longer bar than previous deprojections ($\sim 3.5 kpc$), with axis ratio of 1:(0.3-0.4):0.3, and a bar inclination of $20^\circ \leq \phi_{bar} \leq 25^\circ$.

Star counts have also been used in the last years to disentangle some important bar parameters. Benjamin et al. (2005), used a catalog of ~ 30 million mid-infrared sources, taken by the space telescope *Spitzer*, to determine the distribution of stars in Galactic longitude, latitude, and apparent magnitude. It was found that the simplest structure which justified the data was a linear bar of half-length $\sim 4.4 kpc$ and bar inclination $\phi_{bar} = 44^\circ \pm 10^\circ$. The apparent contradiction between the galactic bar at $\phi_{bar} \simeq 20^\circ$ or $\phi_{bar} \simeq 40^\circ$, which results from the different techniques, seems to be settled by the works of Lopez-Corredoira et al. (2007) and Cabrera-Lavers (2008). They have also analyzed infrared stars counts in the galactic center, and established that two structures seem to coexist in the bulge, a triaxial bulge roughly extending until $|l| \leq 10$, and a thin, elongated bar of dimensions $7.8 \times 1.2 \times 0.2 kpc$. Hence, the galactic bulge still seems to keep many of its secrets.

Microlensing (Alcock et al. 1995) has also been a source of information of the mass and velocity distribution of the galactic bulge. Microlensing occurs when a mass (the lens), presumably a stellar mass, crosses the line of sight of another observed star (the source). On galactic scales, multiple lensed images are separated by a few miliarcseconds, and therefore are rarely resolvable. However, the flux amplification effect in the observed star is easily observable and allows the determination of the masses involved in some cases. Even though these events are rare, the regular observation of millions

of stars allows the detection of hundreds of them every year. The microlensing optical depth is the probability that a source star at a certain distance from us is lensed, depending only on the mass density along the line of sight to this star. Thus, optical depth can be used as a diagnostic of the bulge structure. Paczyński (1994) showed that the value found in the galactic bulge for the optical depth $\tau = (3.3 \pm 1.2) \times 10^{-6}$ is three times higher than the value expected for an axisymmetric bulge. Therefore, he explained the optical depth with a bar about 15° from the line of sight. Discrepancies between newer measurements of the optical depth and the values predicted for Milky Way's models are still found.

1.2.2 Bar evolution

A considerable fraction of the total of disk galaxies is barred ($\sim 50\%$). Bars are then an important feature, which often appear during the evolution of some galaxies. Normally, in external galaxies the bar component is easily identifiable when the galaxy is face-on, or close to it. Even in a edge-on or end-on line of sight (the end of the bar in the line of sight) a bar will produce features in the bulge which can be detected. Thus, the abundant information collected in these bar galaxies can give us important clues about the evolution of our own galaxy.

Distinctive components can be separated from the light distribution of spiral galaxies, where customary tools in the classification of the bulges are the Sersic index, flattening and color. The components thus recognized are normally a disk, a bulge and/or a bar, depending on the classification. An interesting example of detection of bars by different observational techniques is the work of Kuijken & Merrifield (1995), where direct kinematical evidence of the bar is obtained from the line of sight velocity diagram (LOSVD). In those diagrams, bulges containing a bar show a distinctive "eight-shape", which is derived from the transition between bar orbits. Gas orbits can not intersect themselves, and as a result, there will be gaps in the LOSVD when a bar is present. Nowadays three different kind of bulges can be distinguish in the literature, the distinction in these bulge types is not only related to their external shape, but also to the underlying formation history that has led to the present state. Hence, the three types of bulges are: classical, boxy/peanut, and disky (Athanasoula 2005). Classical bulges are believed to be formed from gravitational collapse or hierarchical mergers of lesser objects, which occurs generally early and before the formation of the disk. These bulges closely resemble elliptical galaxies in their kinematics, radial profiles and stellar populations. Thus, old stellar populations and elliptical shapes dominate in these bulges. Boxy/peanut bulges on the other hand, are the natural consequence of bar evolution. A bar is formed in the disk presumably from an initial perturbation in the disk. The evolution of the orbit families in the bar produces later the bar buckling in which some orbits reach sometimes high latitudes, the projection of these high-latitude stellar families give the characteristic boxy/peanut shape. According to N-body simulations (e.g. Combes et al. 1990, Athanasoula 2003, and references therein) the evolution of the bar and its exchange of matter with the inner disk causes the stellar populations to be mixed up in the bulge/bar structure and the inner disk when the radius is simi-

lar. Nevertheless, the majority of the bulge/bar population age should be higher than those in the disk even though the bar instability can trigger some local star formation. Finally, disk-like bulges (or pseudo-bulges) combine some features of bars and disks. They seem to be formed in a similar way as the boxy/peanut bulges, from an instability in the preexisting disk. However, in this case it is the bar torque which drives gas to the inner disk. Thus, an inner disk is formed which extends until the inner Lindblad resonance, where a ring can also be formed. The new disk will accumulate mass and will trigger some star formation in the central part of the disk. In the end, a sizeable disk is formed. The properties of these bulges can sometimes be the ones expected in disk systems. They can contain a significant population of young stars and considerable amounts of gas. These two characteristics are more pronounced than in the two other types of bulges.

All this leads to a complicated picture of bar evolution, which can not easily be simplified. Moreover, the scenario of bar destruction due to the exchange of angular momentum with the inner disk, which in N-body simulations makes the bar more massive and slow until it destroys itself, as been proposed as a cyclical process (e.g. Combes 2007). In this process of destruction and reformation of bars in the center of galaxies gas seems to play a crucial role.

1.2.3 Modeling the dynamics of the Milky Way

A self-consistent model which agrees with the dynamical and photometric data in the galactic bulge has been a difficult goal to achieve. The scarcity of suitable data, and the technical problems involved have seriously restricted the number of models applied to the galactic bulge.

One of the few is Kent's model (Kent 1992), which assumes a constant mass-to-light ratio in order to turn the luminosity model described in Kent, Dame, & Fazio (1991) into a mass model and potential. The Milky Way is assumed to be an oblate isotropic structure with a black hole in its center. The results of this model successfully reproduced a variety of stellar velocity dispersions, however, it was unable to reproduce the observed HI and CO rotation curve at small radius.

Schwarzschild (1979; 1982) formulated a technique which has been specially useful in the modeling of the Milky Way. The Schwarzschild technique, consists of the calculation of a suitable orbit library derived from a potential, which in turn is consistent with the density distribution of the galaxy studied. Armed with the orbits integrated in the potential, the phase-space distribution function is fitted by a Non-Negative-Least-Square algorithm (NNLS) to a set of observables. One of the main difficulties (as we will see in Chapter 4) of the Schwarzschild technique in barred galaxies is to define a library representative of the phase-space. This is due to the inability to determine the three integrals of motion of the barred potential, these are quantities conserved during the orbit trajectory, which are extremely useful to constrain the library to realistic orbits.

Zhao (1996), successfully applied the Schwarzschild technique in a self-consistent model for the Milky Way's bulge. Zhao's input information for the model included

the COBE-DIRBE deprojection by Dwek et al. (1995) and a set of different observations which consisted of radial velocities and proper motions in Baade’s Window (Sadler et al. 1996, and Spaenhauer et al. 1992 respectively), radial velocity and dispersions at the $(8^\circ, 7^\circ)$ field (Minniti et al. 1992) and $(-1^\circ, 2^\circ)$ field (Blum et al. 1994, 1995), the overall solid-body rotation curve from bulge stellar traces as Miras, SiO masers, OH/IR stars, and planetary nebulae (Dejonghe & Habing 1992). Zhao’s model yielded a best fit with a 7% difference with the input density distribution, and reproduced reasonably well other observables, such as the velocity dispersion. A considerable fraction of the orbits found in the best fit of the model were found to be chaotic, however regular orbits contributed most of the mass to the bar/bulge.

By contrast to Zhao’s model, a completely different technique was applied in Englmaier & Gerhard (1999). The latter used a sophisticated hydrodynamical code to model the gas flow inside ~ 10 kpc radius. The potential consisted of a multipolar expansion of the deprojection described in Binney, Gerhard & Spergel (1997), and therefore from the COBE-DIRBE image. The model was able to reproduce many gas dynamical features with its four-armed spiral structure. In addition, an interesting bar radius of $R_{\text{bar}} \sim 3.5$ kpc and bar inclination of $\phi_{\text{bar}} \sim 20^\circ - 25^\circ$ were found.

Häfner’s dynamical model (2000) came back to Schwarzschild’s galaxy building technique. A similar approach to Zhao’s model was applied to the construction, combining a distribution function depending on classical integrals (regular orbits) and non-classical integrals (irregular orbits). Thus, the Schwarzschild technique was used to distinguish between the real distribution function and one generated only by the classical component. Similarly to the two previous models, Häfner’s model fitted the 3-dimensional mass density of Binney, Gerhard & Spergel (1997), obtained from the deprojection of the COBE-DIRBE surface photometry. In addition, he included the kinematical data from the fields Baade’s Window, the $(8^\circ, 7^\circ)$ field (Minniti et al. 1992), the last two used in Zhao’s model also, and also the $(12^\circ, 3^\circ)$ field. This model used a library containing 22168 regular orbits and succeeded in fitting the available data inside 3 kpc with reasonable accuracy. Most of the deviation from the input density occurred outside corotation. At the same time, a map of microlensing optical depth of the galactic center was generated.

1.3 THIS THESIS

This thesis, as its title announces, is about the 3-dimensional movements of stars in the galactic bulge, and the physical and structural implications derived from the stellar kinematics observed. Our approach to solve the endless problem of the uncertainties in the actual structure of the galactic bulge is based on the constraints on the phase-space distribution function defining the inner kiloparsecs of the galaxy. Thus, in order to obtain suitable bulge constraints, we have used the two techniques that can deliver such information, radial velocities and proper motions.

Every chapter of this thesis correspond to different stages in a project which attempts to unveil the structural properties of the galactic bulge through the study of regions with low foreground extinction. These regions, commonly named “windows”,

have historically been the natural solution to the fierce extinction due to the disk dust layer, which obscures the central regions of the galaxy. The complete project includes the observation of 10 fields across the galactic bulge: 3 fields at the center, close to the galactic minor axis; three more at positive longitudes, on the near end of the bar; and 4 more in the far-end of the bar, at negative longitudes. The project was originally intended to be entirely in the realm of the kinematics and dynamics, and therefore has little constraints related with abundances. However, we have not left this entirely unattended, as we explain below. This project is still on-going. The results of this thesis will be complemented in the near future with new information derived from the fields on the far-end of the bar. The work presented here deals with the fields close to the galactic minor axis and at positive longitudes.

In **Chapter 2** we report on ~ 3200 new radial velocities, which have been obtained in 6 low foreground extinction windows of the galactic bulge. Our radial velocities were obtained using the VIMOS-IFU camera which allowed us to construct radial velocity cubes in each case. The importance of those cubes is related with the preexisting HST images in those fields (e.g. Kuijken & Rick 2002; Kuijken 2004), obtained from the HST archives. The IFU cubes, combined with the refined spatial information from the HST WFPC2 images, were used to disentangle the spectral information of each star using a new deconvolution algorithm. The results of this process are the stellar spectra in the positions indicated by the HST images. The spectra thus obtained by the new technique reach accuracies typically of $\sim 30 \text{ km/sec}$, which is several times smaller than the observed velocity dispersion of the galactic bulge $\sim 110 \text{ km/sec}$ (Rich 1988; Sadler 1996), and therefore suitable for the study of dynamics, as we will see in chapter 4. The bulge density rapidly drops once we move off-axis. Consequently, for the three minor axis fields we collected ~ 2000 radial velocity measurements, while ~ 1200 such measurements were obtained for the three off-axis fields. In the case of the three minor-axis fields *Sagittarius I*, *Baade's Window*, and *near NGC 6558* it has been possible to go one step further and combine the new radial velocities with the proper motions of Kuijken & Rich (2002). Hence, we have constructed a small subsample of stars per field with well determined 3-Dimensional kinematic information. The results of this subsample highlight very clearly a distinction between the different populations present in the color-magnitude diagram (CMD) of each field. Main sequence, turn-off and Red Giant Branch (RGB) stars show a clear vertex deviation which can be directly related with a signature of triaxiality of the galactic bulge. On the other hand, bright blue main sequence stars beyond the turn-off show velocity ellipsoids inconsistent with the determined bulge populations. Thus, the bright blue main sequence stars in these fields seem to be strongly dominated by a disk population. At the same time, it has been observed that the signature of triaxiality decreases when moving off the plane, being weaker for field *near NGC 6558*, which has the lowest latitude ($b \sim -6^\circ$). The latter gives us an important clue about the extent of the galactic bar and the influence of its potential on the inner kpc of the galaxy.

Spaenhauer et al (1992) was one of the first to obtain a reliable proper motion catalog for stars of the galactic bulge. Their work made use of plates taken several decades apart to obtain 432 proper motions for a sample of stars in Baade's Window.

This sample was the starting point for subsequent studies which determined low resolution abundances in many of the stars originally measured (Terndrup et al. 1995; Sadler et al. 1996). In **Chapter 3** we have explored this sample, which in addition to 3-Dimensional kinematics, count with calibrated abundances. The original low resolution abundances were recalibrated using the high resolution abundance scale by Fulbright et al. (2006). Thus, armed with a sample with 3-dimensional kinematics and suitable abundances, we have studied the velocity ellipsoids derived from several selection criteria. We found a significant vertex deviation in the metal rich population ($[Fe/H] > -0.5$), which did not appear in the metal poor subset. When analyzing the sample more closely as a function of metallicity, a sudden transition in the kinematics is found around $[Fe/H] = -0.5 dex$, from an apparently isotropic oblate disk to a bar. Similarly, a shallower trend toward lower vertical velocity dispersion (σ_b) at higher abundances was found.

Chapter 4 presents the development of a new Schwarzschild model for the Milky Way's bulge. The model has been constructed to reproduce the distribution of proper motions and photometric parallaxes for the three minor axis fields in the project. For each field we selected a subsample of turn-off and main sequence stars in order to build the target (set of constraints) which is going to be fitted. In addition to the proper motions and photometric parallax, a density profile has been crucial to obtain a reasonable set of constraints. This density profile has been provided by the COBE-DIRBE images (Arendt et al. 1994; Weiland et al. 1994) of the galactic bulge. Several deprojections of the COBE images by different techniques were performed. In chapter 4 from an initial analytical deprojection with several free parameters we chose one particular bar model which was added to our set of constraints. This simple bar model consisted of a bar, a disk and a cuspy component. The bar model was used in turn to build a consistent potential with a multipolar expansion, where each orbit forming part of each model was integrated for approximately ~ 10000 rotational periods. A grid of 25 self-consistent Schwarzschild models was run, each one corresponding to a different combination of two important bar parameters, the bar pattern speed Ω_b , and the bar inclination ϕ_{bar} . Results of this set of models show an apparent degeneracy in the best χ^2 , which appears for bars at $30 - 40 km sec^{-1} kpc^{-1}$ of bar pattern speed and bar inclinations of 0° or 40° . To break this degeneracy we introduced in the results the information provided by the radial velocities in chapter 2. Including the radial velocity information we could establish a best bar model which has a reasonable agreement with recent determinations of the galactic bar using other techniques (e.g. Benjamin et al. 2005). Our best bar model, on the other hand, produces a significant number of stochastic (chaotic) orbits, which accounts for a high percentage of the overall mass. Whether the latter is an artifact of the model or is a real effect of the structure and mass concentration applied we can only discern by improving the constraints of the target.

Finally, in **Chapter 5** we report ~ 11000 new proper motions for the fields at positive longitudes Field 4-7 ($l, b = 3.58^\circ, -7.17^\circ$), Field 3-8 ($l, b = 2.91^\circ, -7.96^\circ$), and Field 10-8 ($l, b = 9.86^\circ, -7.61^\circ$). These proper motions, with a time-baseline of 8-9 years, have been calculated using a modification of the Anderson & King (2000) approach, originally intended for observations in WFPC2 with a suitable dithering pattern in

each epoch. The dithering is used to solve the undersampling of the Point Spread Function (PSF) of the images. Thus, the modifications of the original method correct part of the problems derived from the absence of dithering in the first epoch. This is done by means of an algorithm which refines iteratively the PSF from the stars in each image starting from an analytical model. Another relevant difference between these proper motions and those of the minor-axis fields is related to the instruments used in each epoch. While minor-axis epochs were always observed with WFPC2, the proper motions in chapter 5 consist of a combination of WFPC2 and ACS WFC for first and second epoch respectively, which implied small modifications to the procedure. The results of these stellar proper motions show a remarkable similarity with those of the fields close to the galactic minor axis (Kuijken & Rich 2002), where mean μ_l behaviour can be directly related with the intrinsic rotation of the bulge. The latter means that even at the longitudes of the new fields we are able to observe a considerable fraction of bulge stars. Consistently, a distance effect can be seen in the velocity dispersions, stars lying farther away tend to show a smaller dispersion. A more refined search of changes in the velocity ellipsoid as a function of the distance did not produce significant differences, which also agrees with a previous study in Sagittarius-I using ACS WFC proper motions (Clarkson et al. 2008). Thus, the information provided for these fields in the near-end of the bar will provide unique constraints on our model in the near future.

1.4 FUTURE PROSPECTS

This thesis, as we have mentioned in the previous section, is embedded in a project which includes 4 more fields in addition to the ones discussed here. There are several aspects of this work which are susceptible to being improved; the galactic bulge being such a vast subject, in theory it is possible/desirable to include a huge number of additional information in order to obtain a group of constraints that would tell us more about the structure and the history of the galactic bulge. Nevertheless, we can point out what we think are the most urgent modifications or improvements which would optimize future efforts on this project.

Chapter 2 explains the techniques and the implications of our new radial velocities (RV) in 6 fields of the galactic bulge, which map the center and the near end of the bar. New observations for the fields at negative longitudes, at the far-end of the bar are expected to be completed. Observation time in those far-end bar fields has been granted for 2009 in HST, after ACS WFC is repaired. With the second epoch of the proper motions completed, it would be possible to plan the respective VIMOS-IFU observations.

In Chapter 4 we explain the scope of our current Schwarzschild model. The model, in its present stage of development, is able to predict the distribution of radial velocities (RV), but does not include any constraint from RV. All the constraints come from density, proper motions, and photometric parallax. Even though it is still possible to combine the information of the RV with the proper motion and parallax, this combination would not have a physical meaning unless the χ^2 of the model has a physical

meaning. Thus, the optimal procedure is to include the RV data directly in the model as a new set of constraints. The latter procedure would require a smoothing of the RV data, which represents a much smaller population. Despite this, we believe it is a reasonable assumption to consider the RV population as representative as the proper motion population, as long as we maintain the same constraints by the CMD and keep a reasonable ratio between RV and proper motion stars. Similarly, a more evident modification of the model, implies the expansion of it to include the new fields at positive longitudes. This would increase the maximum number of constraints in a factor of $7/4 = 1.75$. At the same time, we would urge the testing of other techniques of deprojection. Our current density profile makes use of a deprojection from a simple bar model which assumes eight-fold symmetry and just three components; in the future we would like to include additional features in the density profile that would break in some cases such symmetry, like arms and a dark halo. Similarly, gravitational stability in the best fit model must be addressed. A consistent N-body model is under development.

In Chapter 5, we have presented new proper motions in three new fields in the near-end of the bar. The procedure, as we already explained, consisted of combined observations by HST WFPC2 and ACS WFC for first and second epoch respectively. New observations, on the other hand, for the four fields in the far-end of the bar will be done with ACS WFC for the first and second epoch. ACS WFC in both epochs will provide a much better positional accuracy, which in turn will require some changes in the procedure (Anderson & King 2006). PSF variation across each image and local flux variations must thus be included in the procedure.

The project, of which this thesis forms a part, will continue. Once it is completed, it will provide significant insights into the bulge structure from the perspective of kinematics and dynamics. Several other projects with the same goal are currently on-going. The Bulge Radial Velocity Assay (BRAVA), and the VVV VISTA survey (Variables in the Via Lactea), are current examples of a vigorous topic which awaits with high expectations the first results of Gaia during the next decade.

REFERENCES

- Anderson, J., & King, I.R. 2000, *PASP*, 112, 1360
- Anderson, J., & King, I.R. 2006, ACS Instrument Science Report 2006-01 (Batimore: STScI)
- Arendt et al. 1994, 425, L85
- Athanassoula, E. 2003, *MNRAS*, 341, 1179
- Benjamin, R.A., et al. 2005, *ApJ*, 630, L149
- Berendzen, R., Hart, R., Seeley, D. 1976, "Man Discovers the Galaxies", Science History Publications
- Binney, J., Gerhard, O.E., Stark, A.A., Bally, J., Uchida, K.I. 1991, *MNRAS*, 252, 210
- Binney J., Gerhard O.E., Spergel D. 1997, *MNRAS*, 288, 365
- Bissantz N., Gerhard O. 2002, *MNRAS*, 330, 591

- Blitz, L., Spergel, D.N. 1991, 379, 631
- Blum, R.D., Carr, J.S., DePoy, D.L., Sellgren, K., Terndrup, D.M. 1994, ApJ, 422, 111
- Blum, R.D., Carr, J.S., DePoy, D.L., Sellgren, K., Terndrup, D.M. 1995, ApJ, 449, 623
- Combes, F., Debbasch, F., Friedli, D., Pfenniger, D. 1990, A&A, 233, 82
- Combes, F. 2007, IAUS, 235, 19C
- Clarkson, W. et al. 2008, ApJ, 684, 1110
- de Vaucouleurs, G. 1964, IAUS, 20, 88D
- Dejonghe, H., Habing H.J. 1992, Proc. IAU Symp. 153, Galactic Bulges. Kluwer, Dordrecht.
- Dwek, E., et al. 1995, ApJ, 445, 716
- Englmaier, P., and Gerhard, O. 1999, MNRAS, 304, 512
- Fulbright, J. P., McWilliam, A., & Rich, R. M. 2006a, ApJ, 636, 821
- ent, S.M. 1992, ApJ, 387, 187
- Kent, S.M., Dame, T.M., Fazio, G. 1991, 378, 131
- Kuijken, K., & Rich, R.M. 2002, AJ, 124, 2054
- Liszt, H.S., & Burton, W.B. 1980, ApJ, 236, 779
- López-Corredoira, M., Cabrera-Lavers, A., Mahoney, T.J., Hammersley P.L., Garzón, F., González-Fernández, C. 2007, AJ, 133, 154
- Cabrera-Lavers, A., González-Fernández, C., Garzón, F., Hammersley P.L., López-Corredoira, M. 2008, A&A, 491, 781
- Matsumoto, T., et al. 1982, in *The Galactic Center*, ed G.Riegler & R.Blandford (New York: American Institute of Physics)
- Mihalas, D., Binney, J. 1981, "Galactic Astronomy: Structure and Kinematics", W.H. Freeman and Company
- Minniti, D., White, S.D.M., Olszewski E., Hill, J. 1992, ApJ, 393, L47
- North, J. 1994, "The Fontana History of Astronomy and Cosmology", Fontana Press
- Paczyński, B., Stanek, K.Z., Udalski, A., Szymanski, M., Kaluzny, J., Kubiak, M., Mateo, M., Krzeminski, W. 1994, ApJ, 435, L116
- Pfenniger D. 1984, A&A, 141, 171
- Oort, J.H. 1927, Bull. Astron. Inst. Netherlands, 3:275
- Oort, J.H. 1928, Bull. Astron. Inst. Netherlands, 4:269
- Peters III, W.L. 1975, ApJ, 195, 617
- Rich, R.M. 1988, AJ, 95, 828
- Sadler, E.M., Rich, R.M., Terndrup, D.M. 1996, AJ, 112 171
- Sinha, R.P. 1979, in *The Large Scale Characteristics of the Galaxy*, ed. W.B. Burton (Boston:Reidel), 341
- Spaenhauer, A., Jones, B.F., Withford, E. 1992, AJ, 103, 297
- Schwarzschild, M. 1979, ApJ, 232, 236
- Schwarzschild, M. 1982, ApJ, 263, 599

-
- Terndrup, D.M., Sadler, E.M., Rich, R.M. 1995, *AJ*, 110, 1174
Weiland, J.L., et al. 1994, *ApJ*, 425, L81
Zhao, H.S., Spergel, D.N., Rich, R.M. 1994, *AJ*, 108, 2154
Zhao, H.S. 1996, *MNRAS*, 283, 149

CHAPTER 2

Radial Velocities for 6 bulge fields: Procedures and results

M. Soto, R.M. Rich, K. Kuijken
to be submitted

The detailed structure of the galactic bulge still remains uncertain. The strong difficulties of obtaining observations of stars in the galactic bulge have hindered the acquisition of a kinematic representation for the inner kpc of the Milky Way. The observation of the 3-d kinematics in several low foreground extinction windows can solve this problem. We have developed a new technique, which combines precise stellar HST positions and proper motions with integral field spectroscopy, in order to obtain reliable 3-d stellar kinematics in crowded fields of the galactic center. In addition, we present results using the new techniques for six fields in our project. A significant vertex deviation has been found in some of the fields in agreement with previous determinations. This result confirms the presence of a stellar bar in the galactic bulge.

2.1 INTRODUCTION

The Milky Way bulge is the nearest example of a bulge/spheroidal population that we can observe. Its closeness allows us to resolve stellar populations and the associated kinematics, something which is not possible in external galaxies. Even though many data have been gathered, a detailed unified picture of the galactic bulge including abundances, stellar populations and kinematics is far from being completed.

One of the main difficulties is the location of the Sun inside the disk dust layer, which limits observations to a few windows where the foreground dust extinction is relatively low. In addition, populations in these windows are projected on top of each other, complicating the analysis. Disk and bulge components overlap in the color-magnitude diagram specially near the turn-off (Holtzman et al. 1998), hampering a selection based on photometric criteria alone.

In spite of these limitations, important information has been gathered over the years. One of the pioneering studies of the kinematics of the galactic bulge was that of Spaenhauer et al. (1992), who measured proper motions for ~ 400 stars from photographic plates obtained in 1950 and 1983. This proper motion sample was the basis for subsequent abundance and radial velocity studies of the original proper motion sample (Terndrup et al. 1995, Sadler et al. 1996). Zhao et al. (1994) combined the results of these studies with those obtained previously by Rich (1988, 1990), and compiled a small subsample of 62 K Giants with 3-d kinematics and abundances. In spite of its small size the subsample showed a significant vertex deviation, a signature of barlike kinematics. This result has recently been confirmed with a larger sample of ~ 300 stars (this thesis, chapter 3). de Vaucouleurs (1964) had originally suggested that our galactic bulge was actually barred, based on the similarity of its spiral structure with other galaxies with strong bars. Nevertheless, direct stellar signatures of the barlike structure had not been found before.

In addition to models of the stellar distribution (e.g. Zhao et al. 1996a) gas observations and hydrodynamical models also have been used to study the galactic bulge (e.g. Englmaier & Gerhard 1999). Many of these models rely on three dimensional deprojections of the galactic bulge derived from the COBE DIRBE images (Dwek et al. 1995) whose results showed asymmetries consistent with a stellar bar in the galactic center. Even though all analyses agree on the rough orientation of the bar, complete agreement about the values of the parameters which would define this bar, such as rotational bar pattern speed or position angle has not been reached yet. For example, values for the angle between the bar's major axis and our line of sight to the galactic center have ranged from $\sim 20^\circ$ in the first galactic quadrant (e.g. Binney et al. 1991) to 44° in a recent new determination by Benjamin et al. (2005) using Spitzer infrared star counts.

Understanding the bulge kinematics requires understanding the gravitational potential that drives the orbits (Kuijken 2004, henceforth K04). Once the kinematics are understood, they can be correlated with stellar population information to build a picture of the galaxy evolution and bulge formation scenario.

In order to improve our knowledge of the stellar kinematics in the bulge region we have embarked on a project to obtain three-dimensional velocities for a large sample

of bulge stars, by combining HST proper motions measurements with VIMOS spectroscopy.

In this paper we present integral-field (IFU) spectroscopic measurements for six bulge fields that have HST proper motion measurements: three fields on the minor axis (Kuijken & Rich 2002, henceforth KR02; KR04) as well as three fields at positive longitudes. We have combined the IFU data cubes with photometric information in a new procedure designed to work in crowded fields; the technique combines the precise HST photometry and IFU spectroscopy to optimize the spectral extraction.

Stellar kinematics involves the measuring the phase-space distribution function. This phase space generally has three degrees of freedom. By providing 4-6 coordinates per star (the two proper motions, two sky coordinates, a distance determination by means of a main sequence photometric parallax, and a radial velocity for a subsample of bright stars) we will overconstrain the phase-space distribution in order to allow us a reliable determination of the orbit structure.

The outline of this paper is as follows. In section 2 we will briefly explain the project of which the work presented in this paper is a part, section 3 is an account of the observations and the methods involved in each case. Section 4 contains the results of our analysis. Finally section 5 is the summary and conclusions for this work.

2.2 PROJECT

The HST data archive contains a treasure in WFPC2 images taken during the nineties. This wealth of images can be used to find suitable first epoch fields for proper motion work; we have chosen ten for this project, our criteria: low foreground extinction, good exposures, and spread in l and b . Hence, the HST archive has provided us with first epoch observations in six fields at $l \sim 0$, and $l > 0$; in addition, we have established four fields at $l < 0$ in order to target both ends/sides of the bar/bulge. The goals for each field are the acquisition of color magnitude diagrams, accurate astrometry, and radial velocities for as many stars as possible.

Figure 2.1 shows all the fields for this project. HST archive images were primarily used to set first epoch proper motion exposures in several low extinction bulge regions, close to the galactic minor axis and at positive longitudes. These initial fields were complemented more recently with observations in four more fields at negative longitudes. Thus, this project strategically spans a wide range of bulge locations, sampling a significant stellar population at the center and both sides of the bulge/bar. Consequently, the proper motion results published in KR02 and K04, represent the first important piece of kinematic information on this project, which we continue here. The complete HST programme described before, which points to proper motions, photometry and parallax distances has been more recently combined with a spectroscopic VLT programme in the same fields, this spectroscopic information, and the techniques involved are the subject of this paper, where Table 2.1 shows the coordinates of each field.

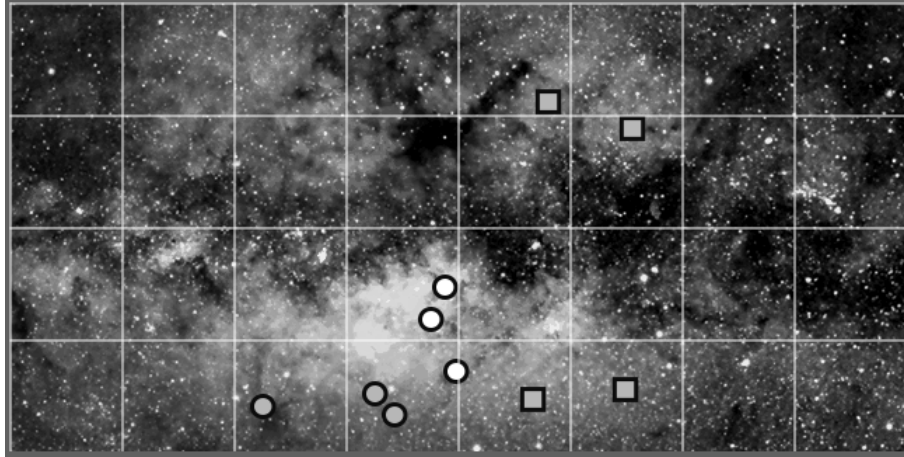


Figure 2.1: Fields in the Galactic Bulge observed for this project, superimposed on an optical map, from longitude $+20^\circ$ to -20° , and latitude -10° to $+10^\circ$. White and grey circles correspond to fields for which proper motion and radial velocity measurements have been completed. Data sets for the four fields at negative longitudes (grey squares) have not been completed so far.

2.3 OBSERVATIONS AND PROCEDURES

2.3.1 Proper motions

First epoch photometric observations with WFPC2 for all the fields used in this paper were obtained from the Hubble Space Telescope data archive. In the case of the three fields close to the galactic minor axis (near $l = 0^\circ$) second epoch observations over a time baseline of 6 years have resulted in accuracies better than 1 mas/yr, which corresponds to errors below 30 km/sec at the distance of the bulge, significantly smaller than the velocity dispersion of the bulge of 100 km/sec. Even longer time baselines for the fields at positive longitudes were used (8-9 years) as Table 2.1 shows. First and second epochs were taken with WFPC2 for fields close to the galactic minor axis, conversely fields at positive longitudes used a combination of WFPC2 and ACS for first and second epoch respectively. The latter fields thus had to include small differences in the procedure to take into account the instrument change (e.g. the shearing of ACS images with respect to WFPC2).

Table 2.1 shows epochs and positions of the proper motion data with WFPC2 and ACS. Proper motions were measured using a modification of the Anderson & King (2000) procedure, which consists of a combination of PSF reconstruction and PSF core fitting (KR02). A more detailed account about the proper motion measurements can be found in KR02 and it will not be repeated here.

2.3.2 Radial Velocities

The procedure to obtain the spectrum of each star in these crowded fields consists of two main steps, the extraction of the spectra for each fiber/pixel in the IFU field, and

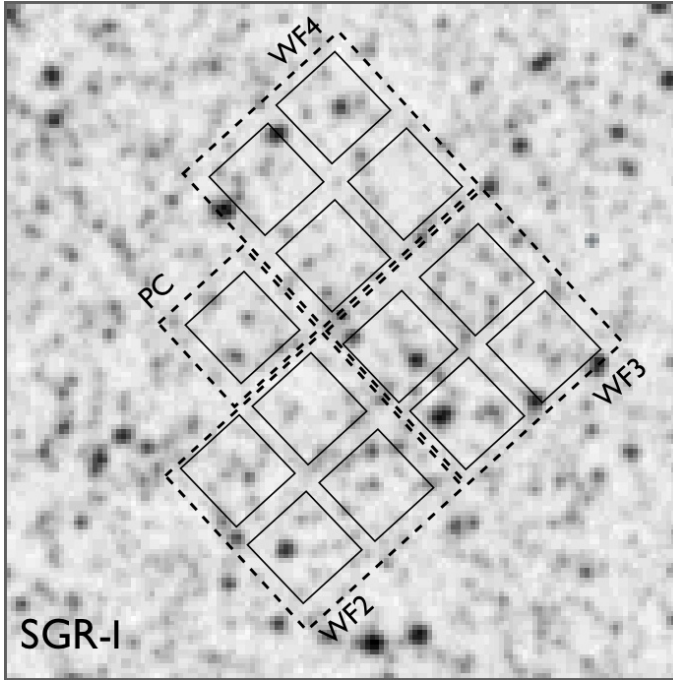


Figure 2.2: Finding chart for one of our fields, *Sagittarius-I*, using an image from 2MASS. Each small square (solid line) corresponds to each one of the VIMOS IFU fields. Dashed squares correspond to PC, WF2, WF3 and WF4 HST fields superimposed on the same image.

the extraction of the star spectra from the IFU data cube. During the second step we will combine the spectroscopy with the information yielded by HST imaging.

The VLT VIMOS Integral Field Unit (IFU) has a $27'' \times 27''$ field of view in high resolution ($R \sim 2050$) which allows spectra to be taken on a 40×40 grid simultaneously. Thus, this instrument allows to target a high number of bulge stars in every exposure with a high spectral accuracy (a spectral dispersion of $0.56 \text{ \AA}/\text{pixel}$), where the blue

Table 2.1: Radial Velocity and Proper-Motion Fields.

Field	PM Epoch	PM Instrument	(l,b)	α, δ (J2000.0)
Baade's Window	1994 Aug	WFPC2	(1.13, -3.76)	18 03 10, -29 51 45
	1995 Sep	WFPC2		
	2000 Aug	WFPC2		
Sgr-I	1994 Aug	WFPC2	(1.26, -2.65)	17 59 00, -29 12 14
	2000 Aug	WFPC2		
NGC 6558	1997 Sep	WFPC2	(0.28, -6.17)	18 10 18, -31 45 49
	2002 Aug	WFPC2		
Field 4-7	1995 Jul	WFPC2	(3.58, -7.17)	18 22 16, -29 19 22
	2004 Jul	ACS/WFC		
Field 3-8	1996 May	WFPC2	(2.91, -7.96)	18 24 09, -30 16 12
	2004 Jul	ACS/WFC		
Field 10-8	1995 Sep	WFPC2	(9.86, -7.60)	18 36 35, -23 57 01
	2004 Jul	ACS/WFC		

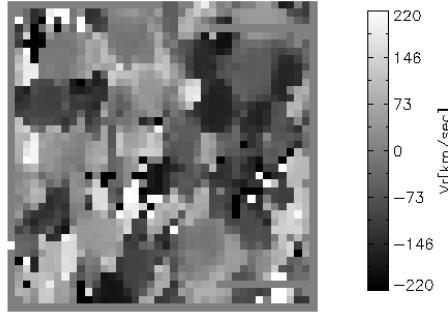


Figure 2.3: Velocity field for one of our IFU observations in Baade' window. The velocity for each pixel/fiber has been calculated using cross-correlation, where each fiber corresponds to $0.66''$. The VIMOS-IFU instrument allows clearly to distinguish between adjacent stars with different kinematics.

Table 2.2: Summary of Radial Velocity Observations .

Field	1 st run (2003)	2 nd run (2006)	3 rd run (2007)	Total IFU Fields	Stars with Rad. Vel.
Baade's Window	5	5	4	14	965
Sgr-I	5	6	5	16	962
NGC 6558	5	5	4	14	766
Field 4-7	0	8	3	12	664
Field 3-8	0	10	3	13	466
Field 10-8	0	9	4	13	756

filter used has a wavelength range spanning from 4150 to 6200 Å. We used this instrument to target our HST fields, which can each be covered by 13 VIMOS pointings (4 per WF chip and 1 per PC, as Figure 2.2 illustrates for Sagittarius-I). Each IFU pointing was exposed for 2×1000 sec, which has allowed us to resolve approximately 80 stars per IFU field. The spectra yield 30 km s^{-1} radial velocity precision, which is well-matched to the transverse velocity accuracy from our proper motions (better than 1 mas/yr , equivalent to $\sim 30 \text{ km s}^{-1}$ at 8 kpc distance), and sufficient to resolve the velocity dispersion in the central parts of the Galaxy, which is about 100 km s^{-1} .

In addition to the regular science images containing the information about our six HST fields, we included regular observations of dark bulge regions to subtract them from the science images as sky, we will refer to this later in this section. Standard stars were observed as well, for use as templates in the cross-correlation process for the determination of the velocities. The overall observation time for all the spectral observations was 17, 50 and 45 hours for our three observing runs respectively. Table 2.2 summarizes the VIMOS IFU observations for the six fields presented in this paper. In Table 2.2 the numbers under every "run" column correspond to the number of IFU fields observed in that run. All data was taken in service mode with seeing conditions constrained at a maximum of $0.8''$.

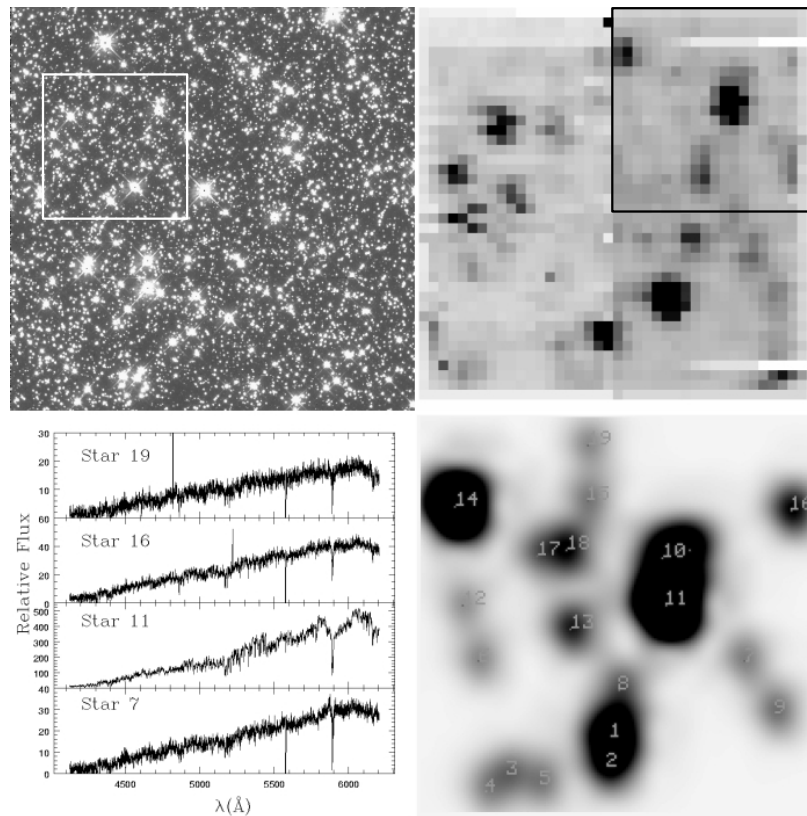


Figure 2.4: Steps during the process to build a star spectrum from the spectral cube. The top left figure corresponds to one of our observations with HST WF2 in Baade’s window, the white square corresponds to the area covered by one of the VIMOS IFU images (top right). In the IFU field the first quadrant is enclosed, its respective convolved image produced during the deconvolution process to check the detection of stars in the first quadrant appear at the bottom right. Finally some examples of the spectra extracted by this process are shown at the bottom left.

Data cube organization and Radial velocity measurements

VIMOS IFU raw data are complex to reduce and calibrate. Fiber spectra extraction was carried out using the ESO pipeline for VIMOS IFU data. Programs GASGANO¹ and

¹available at <http://www.eso.org/observing/gasgano/>

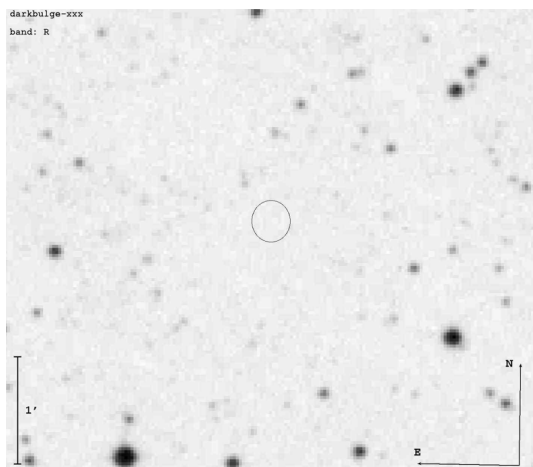


Figure 2.5: Finding chart of one of our darkbulge fields (circle in the middle) over a 2MASS image. Darkbulge fields have been used during the sky subtraction in VIMOS IFU fields.

ESOREX² were used to manage the VIMOS IFU recipes³ (Details about methods and procedures of the recipes can be found in VIMOS pipeline User's Guide and Gasgano User's Manual). The recipes used during our processing were *vmifucalib* and *vmifuscience*.

The final product of the VIMOS IFU recipes are the spectra extracted and wavelength calibrated in one image that includes all the spectra for each quadrant in the IFU field.

An important problem to be considered in spectroscopic reduction is related to the sky subtraction, which has not been implemented by the VIMOS pipeline (VIMOS Pipeline User's Guide 7.23.11). We have tried two approaches. The first is basically the same recommended by the VIMOS Pipeline User's Guide. We took the 20 spectra with lowest signal per quadrant (which means 5% of the total) and averaged them (taking care to reject dead fibers). The combined spectrum was considered as sky and subtracted from the rest of the fibers. This way of proceeding is extremely risky and could change the results that we seek by subtracting a flux level too high (or too low) from the reduced spectra. The second method involves exposures of nearby highly extinguished 'dark bulge' fields, whose spectra, appropriately scaled mimic the sky contribution to the stellar fields as Figure 2.5 shows.

Both processes were extensively tested to check their influence on our radial velocity results; we found no significant differences for both procedures, typically below 3 km s^{-1} in the final velocity measurements per fiber. Given the reliability of our extraction we have preferred to use the sky extraction by dark fields in our fields.

Once the spectra were reduced we assembled them into spectral data cubes. In addition to the regular calibrations, we produced for each IFU field, a response map to check the normal behavior of the fibers through the field. Dead fibers or lost traces are easily highlighted in this way.

The last step is the radial velocity measurement per fiber in each IFU field. The measurement of radial velocities was made in all cases using a cross correlation us-

²available at <http://www.eso.org/observing/cpl/download.html>

³available at <http://www.eso.org/observing/gasgano/vimos-pipe-recipes.html>

ing the IRAF task *fxcor* (Tonry & Davis 1979) with a template standard star. Before the cross correlation some zones of the spectra were masked; for instance the atmospheric emission line due to OI at 5577.5 Å; or the interstellar absorption NaD lines at 5889 Å. The latter lines are particularly strong in K2-3 III Giants, and can easily bias the correlation with our template to calculate velocities or a possible spectral type classification. An example of the velocity field calculated with the procedure here described for one of our IFU fields in Baade's window appears in Figure 2.3, and clearly shows distinct colored zones which correspond to different stars at different velocities. Extracting this information optimally is the subject of the next section.

Deconvolution

As shown in Figure 2.4, the bulge fields are very crowded, and therefore, a reliable technique to correct IFU spectra cubes for blending is absolutely necessary. Fortunately, our HST images allow us to know precisely where the stars are. This information makes feasible the optimal extraction of star spectra from the IFU cubes.

The first step to carry out the deconvolution process is a coordinate transformation from HST to IFU coordinates, which is performed using the standard IRAF tasks *daofind* and *geomap*. Since not all the stars observed in the HST image are detected in the IFU field, a threshold magnitude for the HST list stars must be given. In the case of the fields SgrI, and BW, for which we have F555W observations, this limiting magnitude was set at $V(F555W)_{lim}=21$ mag. Similarly, for fields NEAR NGC6558 (which is actually located close to NGC 6558), Field 4-7, Field 3-8, and Field 10-8 the limiting magnitude is $V(F606W)_{lim}=20-20.5$ mag, depending of the particular crowding in the IFU field. Using this limiting magnitude we avoid the deconvolution of the complete list of stars detected in the HST image, where naturally a large fraction of them are beyond the detection limit of the VIMOS IFU observations.

Armed with a magnitude-limited list of HST proper motions, positions, and magnitudes, we have produced a procedure which accounts for defects in the HST list to separate the fluxes of as many stars as possible from the VIMOS IFU spectral cube. Thus, the HST list, once cleaned from spurious stars due to failures in the DAOFIND detection procedure at 20σ , is used to perform the deconvolution of the stellar spectra in the IFU cube. The deconvolution requires a precise IFU PSF and the HST positions in the IFU field. Simultaneously, a convolved image using the HST magnitudes and positions and the IFU PSF is created during the deconvolution process. This convolved image yields an estimation of blending for each star which is used to select stars with a limited amount of blending for the final list of stars with radial velocities after the deconvolution. Hence, once stars have been deconvolved from the IFU-cube from a HST cleaned list, we can measure our radial velocities.

This deconvolution procedure can be described in more detail as follows: With the final list of cleaned HST stars lying in the respective IFU field and the PSF of the latter we can estimate the contribution of a star s to each pixel i , which defines the model,

$$P_i = \sum_s F_s C_{si}, \quad (2.1)$$

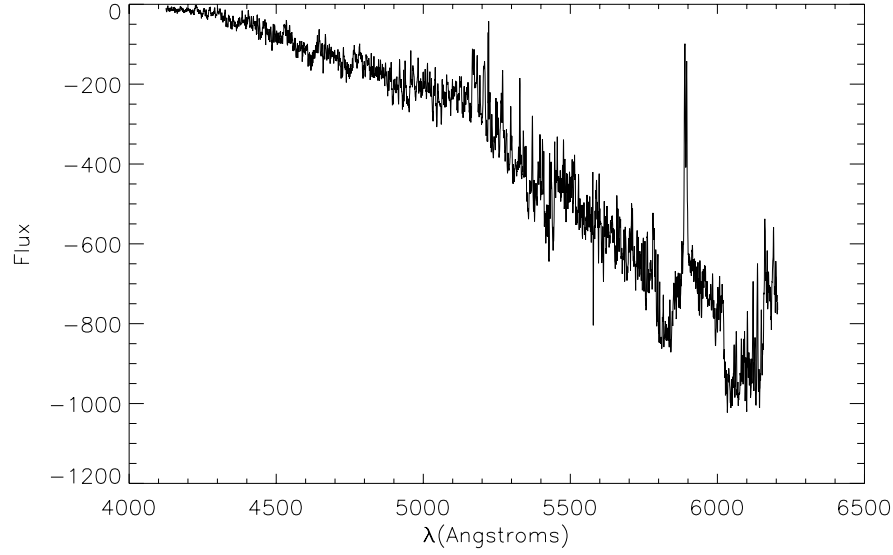


Figure 2.6: Example of the result of using a wrong PSF during the deconvolution. This is the deconvolved spectrum for the HST position in the star 11 in Figure 2.4 obtained using a modified PSF. The flux overestimation in a neighbor star by the PSF produces, when the system is solved, a negative solution for this star. A correlation can not be established with these distorted spectra in the radial velocity measurements.

where P_i is the flux in each pixel, F_s is the flux in the star s and C_{si} corresponds to the contribution of that star s to the pixel i obtained using the IFU PSF.

$$\chi^2 = \sum_i (P_i(\text{observed}) - P_i(\text{model}))^2 \quad (2.2)$$

$$= \sum_i (P_i(\text{observed}) - \sum_s F_s C_{si})^2, \quad (2.3)$$

which can be solved by requiring

$$\frac{\partial \chi^2}{\partial F_s} = 0 \quad \forall s. \quad (2.4)$$

This results in the matrix showed in eq. 2.5

$$\sum_{s'} F_{s'} \left(\sum_i C_{si} C_{s'i} \right) = \sum_i P_i C_{si}, \quad (2.5)$$

which defines a square system. The solution of this matrix for each slice of the IFU data corresponds to the flux solution to that wavelength for each star; repeating the procedure in every slice of the cube we are able to reconstruct the spectrum of each star.

This technique, simple in theory, might yield a singular matrix in some cases, when stars are too close of each other in the HST image, and therefore can not be resolved in

the IFU image. Furthermore, saturation and bleeding would augment the probability of obtaining a singular matrix in eq. 2.5, as these effects produce multiple DAOFIND detections around saturated spots. In order to avoid a singular matrix during the deconvolution procedure, we have implemented several solutions, which we describe below: (1) Due to the differences in the pixel scale and resolution between the HST WFPC2 and the VIMOS IFU image (pixel scale is 0.05" for PC, and 0.1" for WF, while each pixel/fiber is 0.66" in VIMOS-IFU) it is expected that in many cases more than one HST star will fall in one single IFU pixel. Even in those cases, the fluxes of two stars in the same IFU pixel can be separated as long as they can be resolved as single stars using the IFU PSF and the HST positions. The IFU PSF has a typical FWHM in our observations of 1.8 pixels. Thus, we have found realistic to set a minimum blending radius for the stars in the HST list, stars closer than 0.01 IFU pixel-scale have been considered as one during the deconvolution, where fluxes have been added in those cases. (2) Similarly, false detections due to bleeding and saturation in the HST list are discarded by comparing with the positions of stars in the IFU field, crossing both lists, we identify the HST star position which is closer to the position detected in the IFU field, discarding the rest of the detections in the HST list inside an avoidance radius. Typically an avoidance radius of $0.5 \times \text{FWHM}$ of the IFU PSF has been used. (3) Nevertheless, in spite of the two procedures just described, false DAOFIND detections in the HST list have eventually appeared during the deconvolution. These false stars in the HST list were particularly common in long exposures, where saturation and bleeding in bright stars left saturation many pixels away of the central position of the star. In order to solve this we have devised a simple local procedure which iteratively compares the convolved image generated by the HST position, magnitudes, and the IFU PSF with the real IFU field image; stars in the HST list with fluxes $2 \times \text{background}$ of a ratio image (real IFU image divided by a simulated IFU convolved image) are rejected and marked as false stars to generate a new convolved image and a new loop. This iterative process rapidly converges and effectively cleans of false stars due to saturated pixels the HST list of stars. (4) Finally, once the deconvolution is performed, a final selection is carried out, as we mentioned before. This last selection is intended to avoid stars which are blended, mixing different populations, which due to our radial velocity measurement technique, would deliver an average velocity as a result. Hence, we measure as many velocities as possible in single stars. Only stars in which the central positions had at least 70 % of the total flux of the pixel were finally selected. An example of this process and its results is illustrated in Figure 2.4.

A limitation of our technique is related to the PSF construction. The IFU field is small as we have already mentioned, which combined with the area covered for each fiber (0.66"), allows only a few detections in each IFU exposure (~ 40 -80 typically, in normal conditions, with the four quadrants working). This small number of detections often produces a heavily undersampled PSF, which is critical in the deconvolution, where this PSF is used as a model to estimate the flux of every star.

During the development of our procedure each PSF was carefully obtained. The result of using a wrong PSF produces a flux overestimation of some stars. The result of this overestimation is negative fluxes in stars in the neighborhood of some bright stars

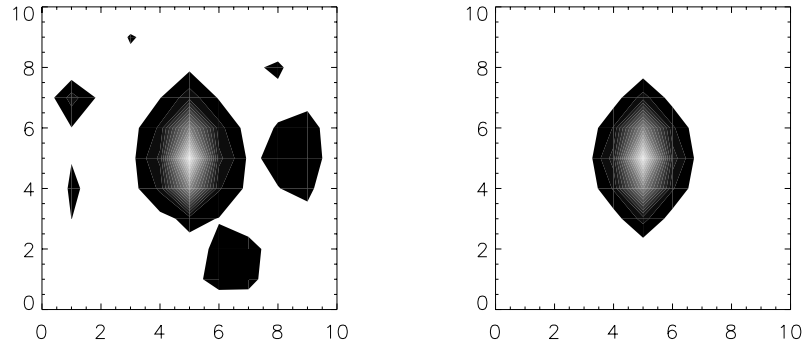


Figure 2.7: Example of procedure to “refit” a IFU PSF. The undersampling of the IFU PSF is fixed by a new fitting procedure which gives more weight to central pixels in order to avoid background noise and contamination by neighbor stars. The new PSF is used during the deconvolution process.

which, when projected to all the wavelengths in the spectral cube corresponds exactly to the spectrum of the neighbor bright star inverted as it is shown in Figure 2.6. A similar result is obtained when many HST positions are located in the proximity of a very bright star, which is a typical failure of photometric detection in bright saturated stars. In all these cases it is not possible to obtain a reliable radial velocity measurement for these inverted spectra. Limited solutions implemented in our code, and already described, relate and compare the stars detected in the HST and VIMOS IFU field in order to solve the crowding. The undersampling of the IFU PSF on the other hand requires additional information. In order to improve this undersampled IFU PSF we performed, a Gaussian “refitting” of the IFU PSF generated by IRAF tasks, where several PSF models were tested. The PSF fit gives more weight to central pixels, where differences in background flux between original and refitted PSF were typically of the order of 3% and did not show significant consequences in the final velocity results. An example of the latter procedure is shown in Figure 2.7, and a summary of all radial velocity measurements for our the six fields is indicated in table 2.2.

An alternative deconvolution

Since deconvolution and cross-correlation are both linear operators, they can be carried out in any order. Thus, an equivalent procedure to deconvolve the cross-correlation function (CCF) obtained from the velocity measurements of all fibers in the quadrant has been implemented. The procedure separates the contributions of the flux of each star in each pixel in the CCF data cube in the same way that spectra for all the stars are deconvolved from the spectra data cube. Consistency between the velocity results using both methods has been proven. Figure 2.8 shows the CCF from the same star in both cases; the maximum in the deconvolved CCF is found at the same pixel position, where each pixel corresponds to 31.78 km/sec. Thus, the deconvolution needs to be run on just a few pixels around the velocity zero channel. At high spectral resolution

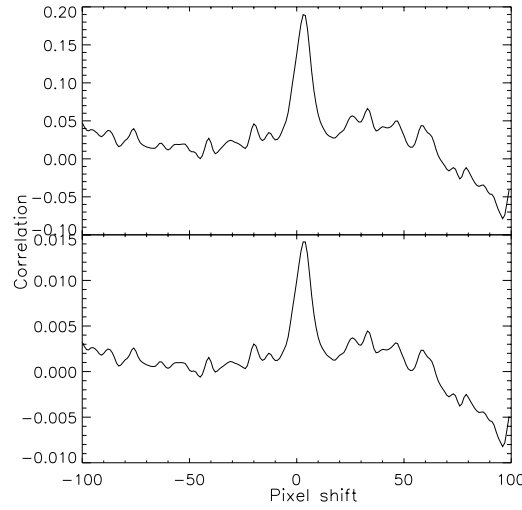


Figure 2.8: Cross-correlation function for one of the stars in Baade’s Window field. (*Top*) Obtained from the velocity measurement of the deconvolved spectrum. (*Bottom*) Obtained directly from the deconvolution of the CCF data cube

the CCF deconvolution could be an interesting way to deblend data cubes spectrally.

Saturation not only affected our deconvolution procedure by adding false stars in the HST DAOFIND, also it affected the estimation of the amount of blending, and therefore the final selection of stars in the IFU spectral cube. The problem of saturation affecting the values of the magnitudes, was specially significant in NEAR NGC 6558 and the three off-axis fields, which count with first epoch HST observations originally intended for the study of faint stars, and therefore with long exposure times. The latter problem was partially solved with the calculation of m_{814} aperture photometry magnitudes from short exposures (50 sec.) of the ACS second epoch images. This was possible only for the three off-axis fields Field 4-7, Field 3-8, and Field 10-8. Consistency of the velocity results has been checked using both magnitudes, showing no differences and therefore allowing us to avoid many misidentification, after the deconvolution in these fields.

2.3.3 Zeropoint Velocity Corrections

Our data combine three observing runs as Table 2.2 shows. In order to check the reliability and performance of our technique we repeated in each observing run one of our fields in Sagittarius-I. *Sgr1-pc* has a reasonable crowding, with a lack of very bright stars, and represents a typical example of the performance of VIMOS IFU during our bulge observations.

Each year’s observations were analyzed with the same HST master list, and reduced independently. Figure 2.9 shows a comparison of the radial velocities obtained. A small but significant offset is evident between the observing seasons. Even though the origin of these deviations has not been identified completely, we have corrected

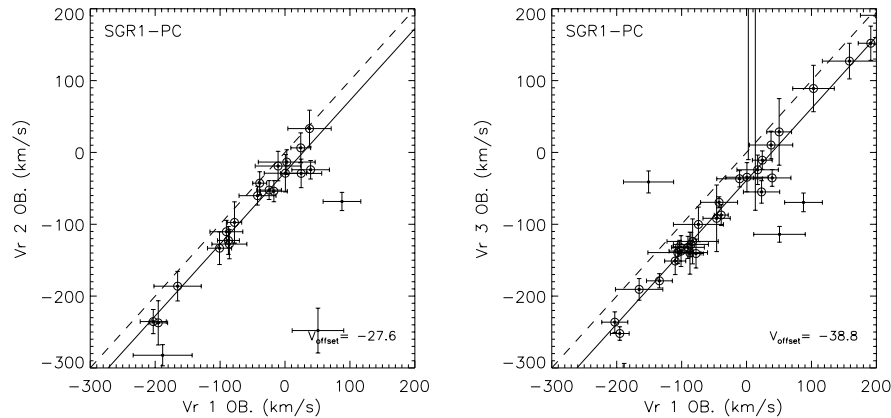


Figure 2.9: Velocity zeropoint determination for second and third run IFU fields. IFU field *Sgr1-pc* velocity results have been compared between the first and second observing run (*left*), and first and third (*right*). The fit in each case is iterative, rejecting stars beyond 40 km s^{-1} of a slope 1 linear fit. Those stars selected in the final iteration are enclosed by a circle.

them in each case. Thus, a zeropoint offset has been added to the observations of the second and third observing runs, of 27.6 and 38.8 km s^{-1} respectively. One possible explanation to this problem could be related to our standard star HD157457, which corresponds to a star in a double system, and therefore susceptible to velocity changes over periods comparable to the time elapsed between our observing runs. Consequently, standard star observations have been cross correlated, comparing their measured velocities with respect to the first run. The latter test delivered similar differences to those found fitting the zeropoint of measurements in *Sgr1-pc*. It has been also checked that this zeropoint is not an artifact particularly related to one of the observations in *Sgr1-pc*. An additional field in Sagittarius-I, *Sgr1-WF2d* which was partially repeated in the third run concords with the offset first found in *Sgr1-pc*.

2.4 ANALYSIS

2.4.1 Velocity results in fields close to the galactic minor axis and off-axis fields

Table 2.3 and Figure 2.10 show our velocity results. We only selected ~ 3200 radial velocities for these plots, which correspond to stars with velocity errors $\leq 50 \text{ km s}^{-1}$. Gaussian fits have been calculated for each velocity distribution, where FIELD 10-8 required a bimodal fit since it corresponds to the sum of the distribution of NGC 6656 (also known as M22) and (presumably) bulge stars in the field.

Our three minor axis fields Sagittarius-I, Baade’s Window and NEAR NGC 6558, which target denser parts of the bulge, account for the majority of the results (~ 2000 radial velocities), while the rest (~ 1000 radial velocities) are more or less equally distributed between the off-axis fields FIELD 4-7, FIELD 3-8, and FIELD 10-8. Sagittarius-I

Table 2.3: Radial Velocity Distribution and Gaussian fit parameters.

Field	N_{stars}	Centre (km s^{-1})	σ (km s^{-1})	Kurt
Baade's Window	781	2	130	0.065
Sgr-I	773	1	123	0.009
NGC 6558	563	-11	72	2.328
FIELD 4-7	488	11	84	2.132
FIELD 3-8	289	-12	60	4.295
FIELD 10-8 ^a	193(381)	-34	96	1.324
FIELD 10-8 ^b	231(381)	-149	17	5.203

^aDistribution of field stars

^bDistribution from NGC 6656 stars in FIELD 10-8.

and Baade's Window have high velocity dispersions, which agree well with previous determinations in BW (Soto et al. 2007, McWilliam & Rich 1994, Sadler et al. 1996) and the galactic rotation and velocity dispersion curves based on K-giants and M-giants (Minniti 1996, and Rich et al. 2007, respectively) at several longitudes (Figure 2.11). However, there are clear differences between these two distributions, BW clearly does not resemble a Gaussian as accurately as Sagittarius-I. Thus, in spite of its closeness, both fields seem to represent slightly different kinematic populations inside the galactic bulge. On the other hand, NEAR NGC 6558 shows a small dispersion compared with the other two minor-axis fields, and it is under the curve of velocity dispersion of the galaxy. Conversely, NEAR NGC 6558 agrees with the bulge rotation curve. In addition, the three minor axis fields show a clear dispersion gradient in galactic latitude. Consistently, kinematic differences between these fields were also seen in proper motions (K04).

In our off-axis fields we found that Field 4-7 and Field 3-8 seem to show a reasonable agreement with the bulge rotation curve. Conversely, FIELD 10-8 does not show a good agreement. This apparent disagreement in the latter field might be caused by strong contamination by non-bulge stars (mainly cluster), or by poor statistics. Therefore, in order to avoid some of the possible contamination by cluster stars in Field 10-8, we have used for the galactic rotation curve the respective Gaussian fit value. This Gaussian fit value for the dispersion agrees well with the galactic rotation curve. Other authors have previously explored contamination rates in Field 10-8. (Minniti et al. 1996)

A key aim of our work is to derive space motions for a large sample of bulge stars, combining radial radial velocities and proper motions. As shown in KR02 main-sequence stars below the turn-off show a proper motion drift consistent with a foreground disk population rotating in front of the bulge, whereas red giants show kinematics representative of the bulge population as a whole. We attempt to remove foreground stars via cuts in the CMD as it is shown in Figure 2.12.

Unfortunately, no such cuts could be applied to the NEAR NGC 6558 field, for

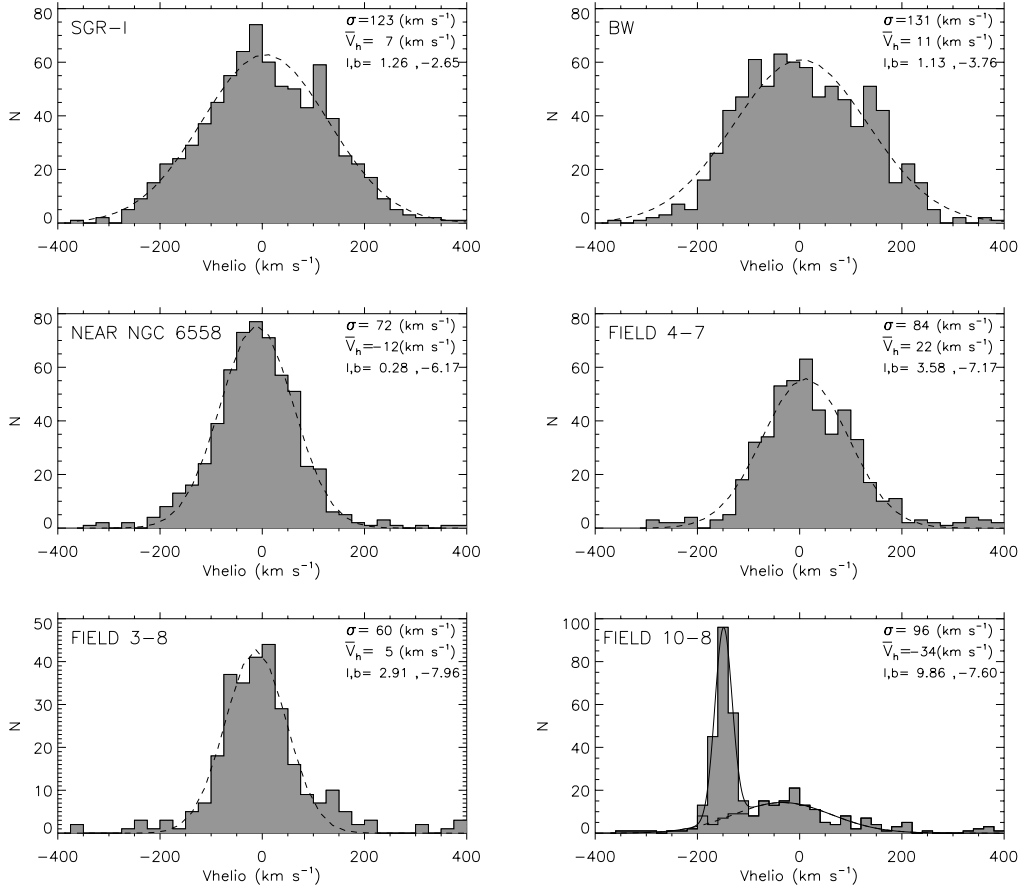


Figure 2.10: Velocity histograms for our six fields. A Gaussian fit has been performed in all the cases.

which no suitable archival first epoch images are available, giant and turn-off stars appear saturated on the respective CMD. Hence proper motions are only available for fainter stars in this field. We expect disk contamination to be a minor problem at the latitude of this field. Our three minor-axis fields, whose results we analyze here, SGR-I, Baade’s window and NEAR NGC 6558 lie close to the galactic minor axis. An axisymmetric bulge should produce at those longitudes velocity ellipsoids aligned with the line of sight. Therefore, any deviation of that alignment in the velocity ellipsoid or vertex deviation is a clear signature of a non-axisymmetric bulge.

Specifically, a vertex deviation should appear in the correlation of transversal proper motion μ_l and the radial velocity V_r . Although this correlation will be affected by line of sight projection and bulge shape, a significant correlation should be a robust bar indicator. We therefore computed the dispersion tensor σ_{ij}^2 . Eigenvalues and eigenvectors of the dispersion tensor correspond to the axis ratio and direction of the axis of the ellipsoid, while the center is given by the velocity first moments. These calculations have been summarized in Table 2.4 and plotted in Figure 2.13. Values σ_r , σ_l and σ_b are the eigenvalues of the velocity ellipsoid and r_S is the Spearman correlation coefficient. Errors on these calculations have been estimated using Bootstrap Montecarlo

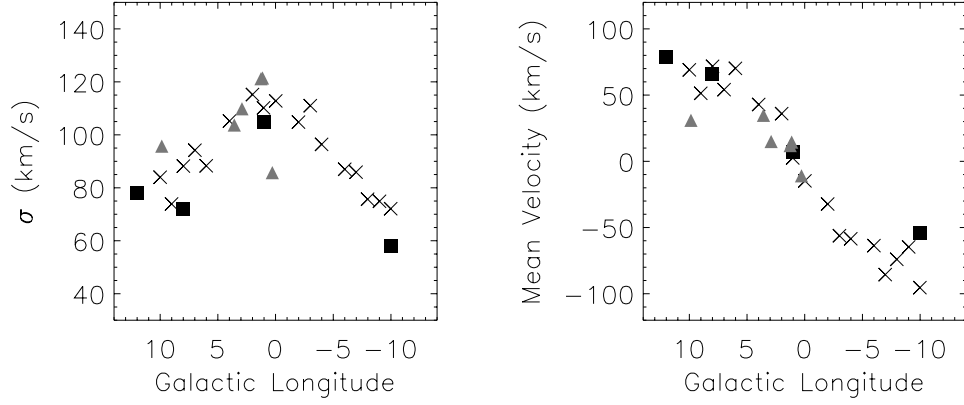


Figure 2.11: Velocity Dispersion σ and Mean Velocity from K-giants by (Minniti 1996) (squares), M-giants by (Rich et al. 2007) (crosses), and our fields (triangles) as a function of the galactic longitude.

Table 2.4: Velocity ellipsoids for galactic minor-axis fields

Field	σ_r km s ⁻¹	σ_l km s ⁻¹	σ_b km s ⁻¹	r_S	Prob(r_S) ^a	l_v ^b deg	N ^c	N _{rej} ^d
Sgr-I	143±3	135±3	109±3	-0.182	2e-5	-39±6	560	9
BW	142±3	118±3	104±5	-0.285	5e-13	-43±4	618	11
NGC 6558	79±4	110±4	109±5	-0.108	0.094	-17±7	242	12
Sgr-I (turn-off)	154±4	142±4	113±4	-0.170	6e-4	-34±7	397	8
Sgr-I (RGB)	112±6	117±6	99±5	-0.200	0.010	-42±9	163	2
Sgr-I (blue-MS)	200±8	124±9	172±9	-0.036	0.740	-7±8	86	5
BW(turn-off)	146±3	119±3	105±5	-0.292	1e-11	-41±6	514	9
BW(RGB)	114±7	114±7	101±6	-0.242	0.013	-40±14	104	1
BW(blue-MS)	108±8	132±10	90±9	-0.155	0.190	-21±7	73	1

^aProb(r_S) corresponds to the significance of the correlation r_S

^bVertex angle

^cTotal number of stars selected

^dNumber of rejected stars during clipping procedure

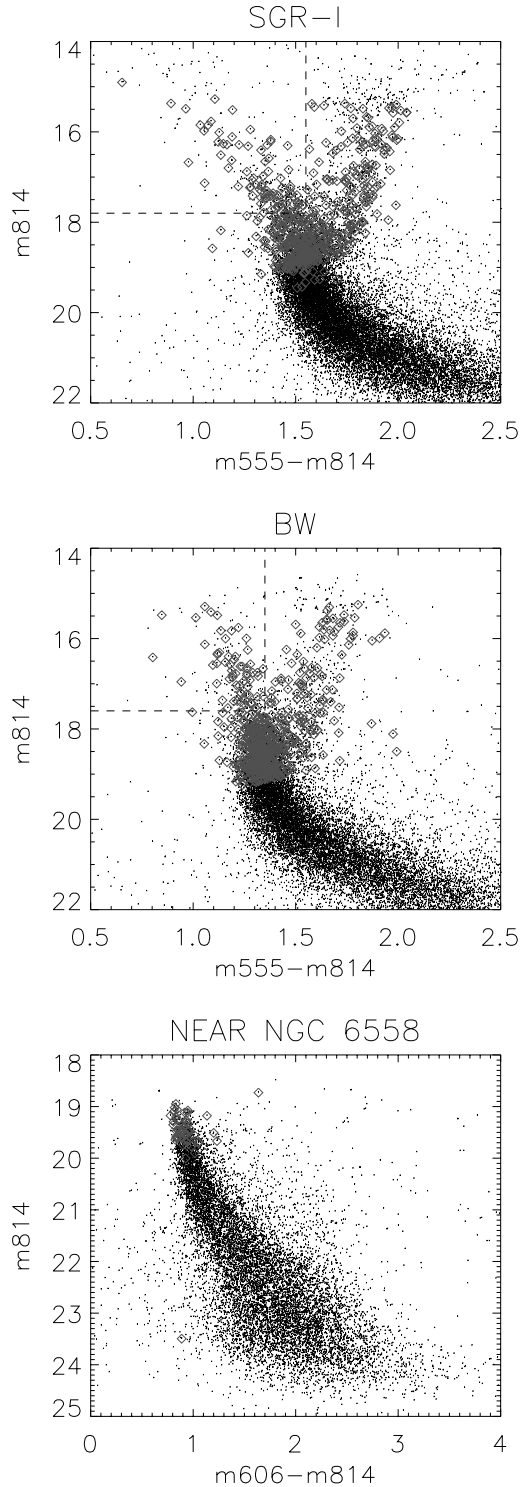


Figure 2.12: CMD for the three minor-axis fields. IFU detections (open squares) have been highlighted over HST detections in each field. Dotted lines in the blue end of the main sequence for Sagittarius-I and Baade's Window fields mark the region in the CMD excluded from bulge analysis due to its proper motions; these are consistent with a foreground population in front of the bulge.

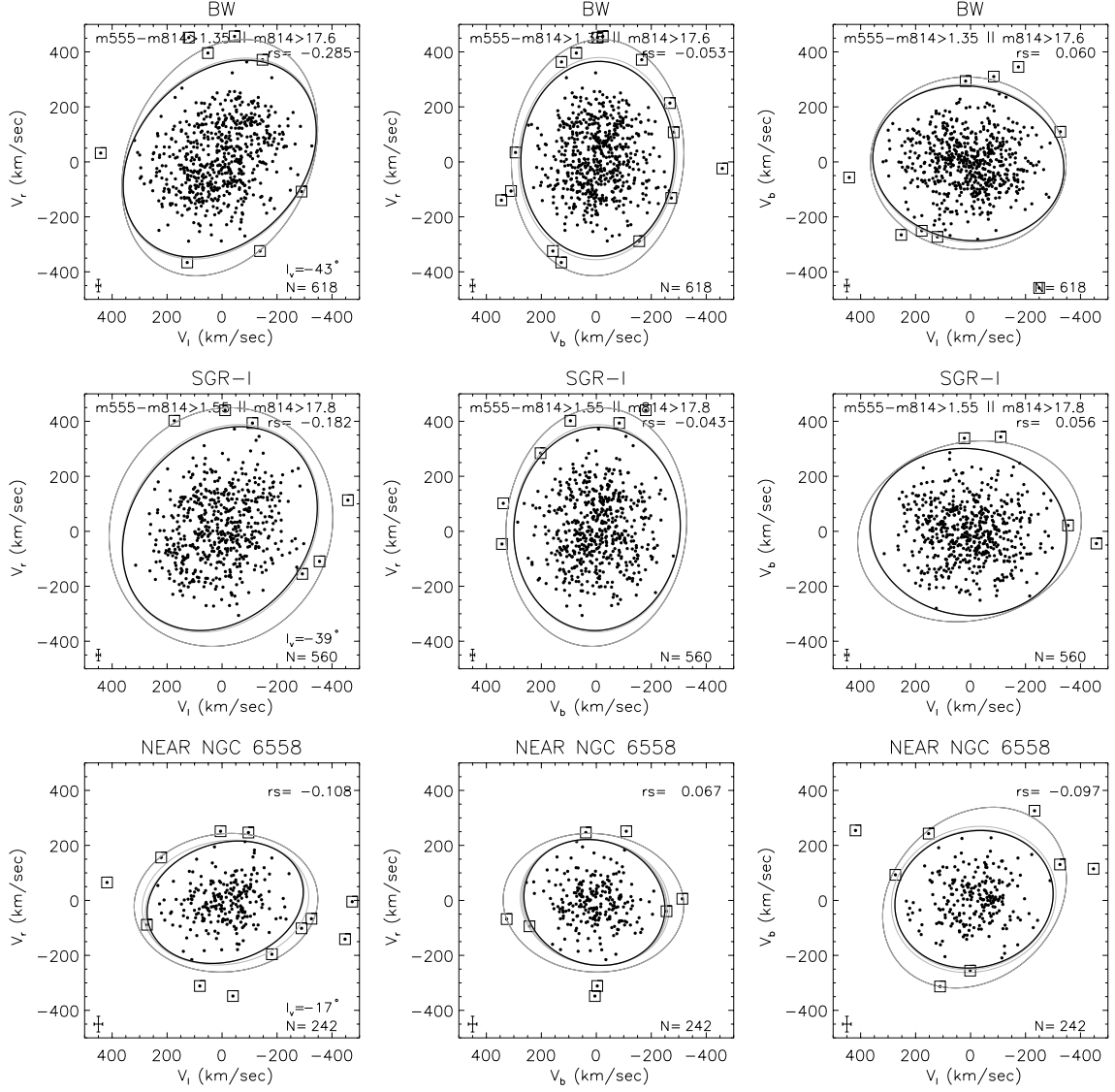


Figure 2.13: Velocity ellipsoids for our minor-axis fields. Correlation between V_l and V_r can be related with bulge triaxiality. The color-magnitude selection has been the same shown in Figure 2.12 and numbers of the cuts are shown in every plot when present (e.g. for Sagittarius-I the selection is $[m555-m814 > 1.55 \text{ or } m814 > 17.8]$, which includes turn-off and RGB stars). An iterative clipping algorithm to reject stars outside 3.0σ of the velocity ellipsoid was used to rid the sample of stars with a kinematic behavior different than the majority. Each figure includes all the velocity ellipsoids to illustrate the convergence of the method. Enclosed points are those rejected for the final velocity ellipsoid for which the parameters found have been included in Table 2.4. A significant correlation has been found in our three minor-axis fields, Baade's window, Sagittarius-I and NEAR NGC 6558.

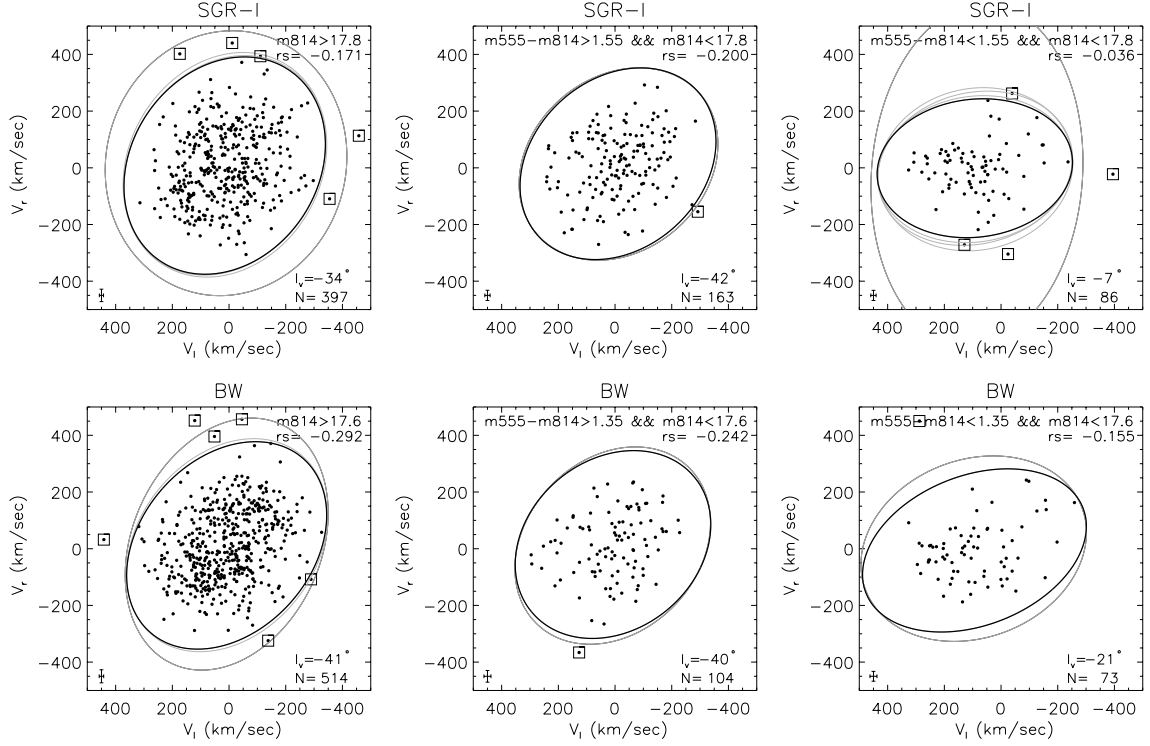


Figure 2.14: Baade's Window and Sagittarius-I velocity ellipsoids for radial velocities (V_r) and transversal proper motion (V_l), divided by population. The region selected is indicated in each plot, and correspond (from left to right) to turn-off, RGB and blue-end of the main sequence.

simulations with 100000 iterations.

The stars shown in Figure 2.13 were selected in the CMD with the same cuts as before. An iterative clipping algorithm was used to derive robust dispersions. Figure 2.13 includes all the iterative velocity ellipsoids, and points within squares are the stars rejected during the process. The values in Table 2.4 are those found in the last velocity ellipsoid. We find a strong correlation in our three minor-axis fields; the vertex deviations are virtually the same for the BW and SGR-I, -43° and -39° respectively, and -17° in NEAR NGC 6558. Similarly the Spearman correlation coefficient r_s shows significant correlation in the three fields, the significance ($\text{Prob}(r_s)$) shows a probability over 99.9% that correlations are real in SGR-I and BW. The latter probability decreases to 91% in the case of NEAR NGC 6558 in agreement with the vertex angle results. Thus, we have a clear trend of an increasing vertex deviation towards the galactic plane in the minor-axis.

Our results agree with previous studies of giants in Baade's window. Even though our selection lacked metallicities, which have been mentioned as a relevant parameter to separate between disk and bulge populations (Minniti 1993, Zhao et al. 1994), the agreement with such samples with well establish metallicities would support our selection criterion. Zhao et al. (1994) analyzed a subsample of 62 stars with metallicities, radial velocities (Rich 1988, 1990) and proper motions from the original sample of 400 K and M giants by Spaenhauer et al. (1992). In the case of Zhao et al (1994),

only a vertex deviation was found in the metal rich population of his small sample (39 stars). More recently, the original proper motions by Spaenhauer et al. have been complemented with radial velocity and metallicity measurements (Terndrup et al. 1995, Sadler et al. 1996) allowing us to have ~ 300 stars with well defined 3-D kinematics and abundances. The result of this increased sample has been consistent with the preliminary Zhao results (Soto et al. 2007) showing a significant vertex deviation only for the metal rich stars. Moreover, the sample of K giants shows a remarkable agreement in l_v with our own sample of turn-off and main sequence stars, where the angles found are -34° and -41° respectively.

On the other hand, our ellipsoids sometimes show larger dispersion than those found in Zhao, Spergel, & Rich (1994). It can be argued that this increase in dispersion might be caused by contamination by halo or disk stars. By contrast to the Zhao, Spergel, & Rich (1994) small subsample, selected by abundances, our selection criterion is far more general (only based on the CMD and proper motion information). The Halo population has been found to be ubiquitous through inner fields of the Milky Way, as it has been observed in BW and M22 fields before (Spaenhauer et al. 1992, Minniti et al. 1996). The signatures of a slowly-rotating component would tend to enlarge the dispersion observed. Thus, a contamination by non-bulge stars seems to be reasonable in our sample which has primarily avoided disk contamination using CMD cuts. Furthermore, contamination by Halo stars should be expected to increase in other fields where bulge does not dominate.

As an additional exercise, we have explored the velocity ellipsoids for Sagittarius-I and BW, dividing the sample in turn-off, blue-end of the main sequence and red giant branch. In order to separate those populations, we have used the same limits in color and magnitudes as before to exclude disk stars. Table 2.4 and Figure 2.14 show these ellipsoids. Turn-off selection from the color-magnitude cuts concentrate most of the stars in both samples, repeating the distribution observed in Figure 2.13. Similarly, RGB velocity ellipsoids follow the same trend as expected by KR02 binned CMD. At the same time, bright blue main sequence stars show no significant correlation in both fields, where the velocity ellipsoids have converged to vertex angles of $\sim 10^\circ$ as would be expected by a foreground population in front of the bulge. All this evidence suggest that our method has successfully isolated the bulge population kinematically, avoiding foreground disk contamination and highlighting bar features. Furthermore, the fact that the vertex angle decreases at higher latitudes gives us some clues about the extent of the dynamical influence of the bar feature in the galactic bulge. We are in the process of incorporating this information into a detailed dynamical model of the bulge/bar.

2.5 CONCLUSIONS

We have described in this paper the procedures and results of a study which aims to identify a significant signature of the stellar bar in several windows with low foreground extinction in the galactic bulge. Radial velocities have been derived from ~ 110 hours of VLT VIMOS-IFU observations.

We have proven that our new methods which combines the information from HST

photometry, proper motions, and IFU spectroscopy makes feasible the detection of the 3-D kinematics of bulge stars. The radial velocity procedure, based on a deconvolution in the spectral IFU cube using HST positions and a IFU PSF have allowed us to obtain more than ~ 3200 stellar radial velocities.

Our large amount of data, combined with the proper motion information already presented in KR02 and K04, have allowed the detection of a significant vertex deviation in our three minor-axis fields, Sagittarius-I, BW and NEAR NGC 6558. The fact that the bar presents its strongest signature in the first two fields decreasing in the lower latitude field NEAR NGC 6558, delivers valuable information about the extent of the bar feature and must be intrinsically related to the detailed structure of the galactic bulge.

This project is still in progress, to the six fields with radial velocities and the proper motion in the three central fields, we will soon add proper motion for our three off-axis fields. Four additional fields with radial velocities and proper motion at negative longitudes have been planned. Thus, our project will sample both ends of the bar obtaining robust constraints in the characteristic bulge parameters. Moreover, a self consistent Schwarzschild model to disentangle the kinematic information in these ten fields is under development. In the end, we expect to determine a detailed picture of the stellar bar and its parameters using the radial velocities and proper motions in our fields.

REFERENCES

- Anderson, J., & King, I.R. 1999, *PASP*, 111, 1095
Anderson, J., & King, I.R. 2000, *PASP*, 112, 1360
Athanasoula, E. 2005, *MNRAS*, 358, 1477
Benjamin, R.A., et al. 2005, *ApJ*, 630, L149
Binney, J., Gerhard, O.E., Stark, A.A., Bally, J., Uchida, K.I. 1991, *MNRAS*, 252, 210
Cudworth, K.M. 1986, *AJ*, 92, 348
Dwek, E., et al. 1995, *ApJ* 445, 716
Englmaier, P., and Gerhard, O. 1999, *MNRAS*, 304, 512
Holtzman, J.A., Watson, A.M., Baum, W.A., Gillmair, C.J., Groth, E.J, Light, R.M., Lynds, R., & O'Neill, E.J., Jr. 1998, *AJ*, 115, 1946
Kuijken, K., Merrifield, M.R., *ApJ*, 443, L13
Kuijken, K., & Rich, R.M. 2002, *AJ*, 124, 2054 (KR02)
Kuijken, K. 2004, *ASPC 317: Milky Way Surveys: The Structure and Evolution of our Galaxy*, Eds. D. Clemens, R. Shah, and T. Brainerd, 310 (K04)
Minniti, D. 1993, *IAUS 153: Galactic bulges*, Eds. Herwig DeJonghe and Harm Jan Habing, 315
Minniti, D. 1996, *ApJ*, 459, 175
Rich, R.M. 1988, *AJ*, 95, 828

-
- Rich, R.M. 1990, *ApJ*, 362, 604
- Rich, R.M., Reitzel, D.B., Howard, C.D., Zhao, H. 2007, *ApJ*, 658, L29
- McWilliam, A., Rich, R.M. 1994, *ApJS*, 91, 749
- Sadler, E.M., Rich, R.M., Terndrup, D.M. 1996, *AJ*, 112, 171
- Spaenhauer, A., Jones, B.F., Withford, E. 1992, *AJ*, 103, 297
- Schwarzschild, M. 1979, *ApJ*, 232, 236
- Schwarzschild, M. 1982, *ApJ*, 263, 599
- Soto, M., Rich, R.M., Kuijken, K. 2007, *ApJ*, 665, L31
- Terndrup, D.M., Rich, R.M., Sadler, E.M., 1995, *AJ*, 110, 1774
- Tonry, J., & Davis, M. 1979, *AJ*, 84, 10
- Zeballos, H., Soto, M., Kuijken, K, Rich, R.M. 2008, (in preparation)
- Zhao, H.S., Spergel, D.N., Rich, R.M. 1994, *AJ*, 108, 2154
- Zhao, H.S., Rich, R.M., & Spergel, D.N. 1996, *MNRAS*, 282, 175
- Zhao, H.S. 1996, *MNRAS*, 283, 149
- Zoccali, M., et al. 2006, *A&A*, 457, L1

CHAPTER 3

Evidence of a Metal Rich Galactic Bar from the Vertex Deviation of the Velocity ellipsoid

M. Soto, R.M. Rich, K. Kuijken

2007, ApJ, 665, L31

We combine radial velocities, proper motions, and low resolution abundances for a sample of 315 K and M giants in the Baade's Window $(l, b) = (0.9^\circ, -4^\circ)$ Galactic bulge field. The velocity ellipsoid of stars with $[\text{Fe}/\text{H}] > -0.5$ dex shows a vertex deviation in the plot of radial versus transverse velocity, consistent with that expected from a population with orbits supporting a bar. We demonstrate that the significance of this vertex deviation using non-parametric rank correlation statistic is $> 99\%$. The velocity ellipsoid for the metal poor ($[\text{Fe}/\text{H}] < -0.5$) part of the population shows no vertex deviation and is consistent with an isotropic, oblate rotating population. We find no evidence for kinematic subgroups, but there is a mild tendency for the vertical velocity dispersion σ_b to decrease with increasing metallicity.

3.1 INTRODUCTION

The galactic bulge is the nearest example of a bulge/spheroidal population. A factor of 100 closer than M31, the proximity of the bulge not only permits detailed measurement of stellar abundances and radial velocities, but also of stellar proper motions. The first such study undertaken (at the suggestion RMR) was that of Spaenhauer et al. (1992). The proper motions were measured from plates obtained at the 200-inch prime focus in 1950 and 1983; these data produced measurable proper motions on the order of 0.5 mas yr^{-1} .

The Spaenhauer et al. (1992) study was the source of an input catalog for a subsequent study of bulge radial velocity and low resolution abundances (Terndrup et al. 1995; Sadler et al. 1996). An early study of the abundances and kinematics of these stars, using published abundances from Rich (1988) and radial velocities from Rich (1990) was undertaken by Zhao et al. (1994). That study suffered from having a relatively small sample size, and the lack of a definitive bulge iron abundance scale; nonetheless the most metal rich subset of stars exhibited a vertex deviation of the velocity ellipsoid in the plot of radial versus transverse velocity. Modeling by Zhao et al. (1994) showed that such a vertex deviation, or rotation of the major axis of the velocity ellipsoid, is a feature expected from the long axis orbits that would support a bar structure. Such a bar had been claimed by Blitz & Spergel (1991) based on asymmetries in surface photometry of the bulge region, and by Binney et al. (1991) from the kinematics of molecular gas.

The possibility of a dominant stellar bar population was strengthened by the spectacular results from the *COBE* satellite (Dwek et al. 1994). All-sky maps of the Milky Way showed an asymmetry that was consistent with a bar, with major axis in the first quadrant. Many subsequent studies confirm the presence of a bar structure based on deprojecting the spatial distribution of the stellar population (Binney et al. 1997) and the Schwarzschild method has been used to build a self consistent rapidly rotating bar (Zhao 1996; Häfner et al. 2000).

Here we combine the proper motions of Spaenhauer et al. (1992), the abundances of Terndrup et al. (1995), and the radial velocities of Sadler et al. (1996) to explore the correlation of abundances and kinematics in the bulge stellar population. Surveys now in progress (Sumi et al. 2004) have achieved total numbers of order 5×10^6 stars. However, the sample of 315 stars on which we report here is at present the largest that has proper motions, radial velocities, and spectroscopically estimated abundances.

In exploring correlations of abundances and kinematics, our aim is to constrain models for the origin of the bulge and bar. When the composition of bulge stars (McWilliam & Rich 1994; Fulbright et al. 2007) is considered, it can be argued that the bulge formed early and rapidly (Matteucci et al. 1999; Ferreras et al. 2003). Kuijken & Rich (2002) isolated the old bulge population by proper motion (a similar study has been recently carried out by Kozłowski et al. 2006), and Zoccali et al. (2003) demonstrated a comparison with a 13 Gyr old main sequence turnoff population; these studies find little room for a detectable trace young population in the bulge. However, there are complicating issues in the chemical evolution. Mg is found to be elevated in bulge stars, while O is only mildly so (McWilliam & Rich 1994; Fulbright et al. 2007;

Lecureur et al. 2006) and the "explosive alphas" Ca, Si, and Ti are also less enhanced than Mg, tracking the thick disk trends with $[\text{Fe}/\text{H}]$. Finally, the bar poses a problem for early formation and enrichment, as the longevity of bars is an issue. If the metals in the bulge were built early and rapidly, how and when did the bar appear and why has it survived?

Correlating abundances and kinematics gives another viewpoint on chemical evolution. Even if the abundance distribution appears to fit the closed box model and the population is old, the correlation of abundances and kinematics may reveal distinct kinematic subgroups. Adding two proper motion vectors to the radial velocity increases the power of this analysis. There have been indications of abundance/kinematics correlations in the bulge. Rich (1990) found that the most metal rich stars have a smaller velocity dispersion. Spaenhauer et al. (1992) found a similar trend in their small sample. Zhao et al. (1994) found evidence for vertex deviation in the most metal rich stars. In a radial velocity study of a large number of bulge M giants, Sharples et al. (1990) found indications for a smaller velocity dispersion for a metal rich subgroup of stars. Minniti (1996) obtained spectroscopy in a bulge field at $(l,b)=(8,7)$ and found differing kinematics (more rotation support and a colder velocity dispersion) for stars with $[\text{Fe}/\text{H}] > -1$. In this paper, we explore abundance/kinematics correlations using both the radial velocity and proper motion data, and abundances from low resolution spectroscopy. We use the new iron abundance scale of Fulbright et al. (2006) to recalibrate the Sadler et al. (1996) low resolution abundances (those being based on the average of the Fe 5270 and 5335 features in the spectra). While the derived abundance for any individual star is uncertain to roughly $+0.3$ dex, the calibration ensures that the kinematic transitions we report here are tied to the best currently available iron abundance scale. The most metal rich stars in Sadler et al. (1996) have formal metallicities in excess of 1 dex; we do not take those values seriously, as they are transformed from outliers.

In this *Letter* we describe our kinematic analysis of the sample of 315 red giants.

3.2 ANALYSIS

In an axisymmetric potential, one of the axes of the velocity dispersion tensor of an equilibrium population must lie in the meridional plane. Any deviation from this situation indicates a non-axisymmetry, or a time variation. We will use the space velocities of our stars to measure the orientation of the axis of the velocity dispersion tensor in the radial-longitudinal velocity plane (known as the *vertex deviation* l_v) and determine whether it is consistent with zero. The angle l_v is defined as

$$\tan(2l_v) = \frac{2\sigma_{lr}^2}{|\sigma_r^2 - \sigma_l^2|} \quad (3.1)$$

where σ_{lr} , σ_r and σ_l are the covariance and standard deviation of the measured velocity components along the r (line of sight) and l (galactic longitude) directions. We measure the dispersions with an iterative clipping algorithm, by repeatedly rejecting stars that lie outside the ellipse with principal axes of 2.5 times the corresponding measured

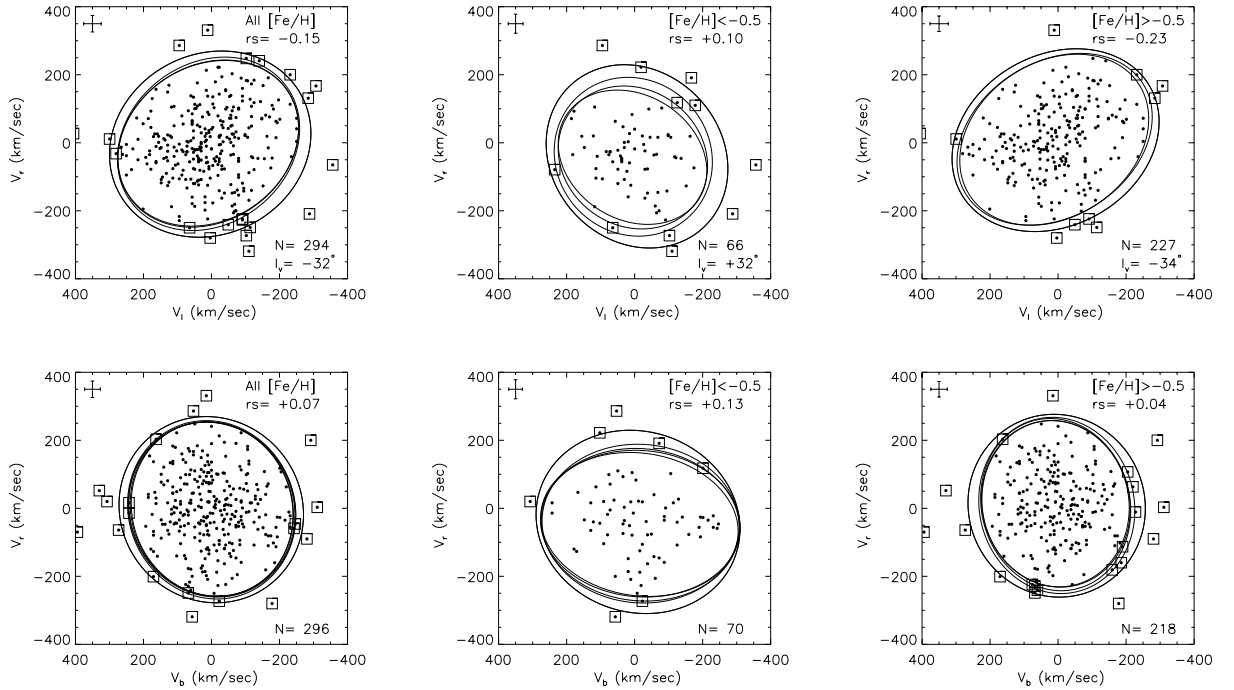


Figure 3.1: Velocity ellipsoids for metal rich and metal poor populations in Baade’s Window. An iterative clipping algorithm to reject stars outside the velocity ellipsoid at 2.5σ has been applied. *Top row, Left to right*, full sample, stars with $[\text{Fe}/\text{H}] < -0.5$, and stars with $[\text{Fe}/\text{H}] > -0.5$ respectively for radial velocity and transversal proper motion velocity ellipsoid. In each panel the vertex deviation l_v , the Spearman rank correlation coefficient r_s , and the number of stars N , is listed. *Bottom row*, same as before, but for radial velocity and latitudinal proper motion. None of the $V_r - V_b$ correlation are significant at the 90% level.

dispersion. Table 3.1 and Fig. 3.1 summarize the velocity ellipsoid parameters found, both for the full sample and for metal poor and metal rich subsets. For each subsample we have calculated the Spearman rank correlation coefficient r_s and its significance.

Proper motions have been transformed to velocities assuming a constant distance of 8 kpc; this should not present a problem, since if the stars are members of the bulge / bar we expect little correlation between metallicity and distance. Ramirez et al. (2000) found no evidence for vertical abundance gradient from 0 to 1000 pc. Rich & Origlia (2007) have derived abundances from echelle spectra of M giants in Baade’s Window (-4°) and a field at -1° and find no difference in either abundance or composition. Therefore, no metallicity gradient is expected. In addition, the adopted value of R_0 does not affect the Spearman rank-order correlation coefficient r_s , which also we use as a vertex deviation indicator.

The most significant vertex deviation is seen in Fig. 3.1 for the metal rich sample ($[\text{Fe}/\text{H}] > -0.5$), whereas metal poor stars show no significant deviation. This result is consistent with the results from Zhao et al. (1994), based on $\sim 20\%$ of the present sample, and proves the reliability of their results (Zhao et al. also saw a vertex deviation in the metal-poor sample, of opposite sign to the metal-rich set: with the addition of the

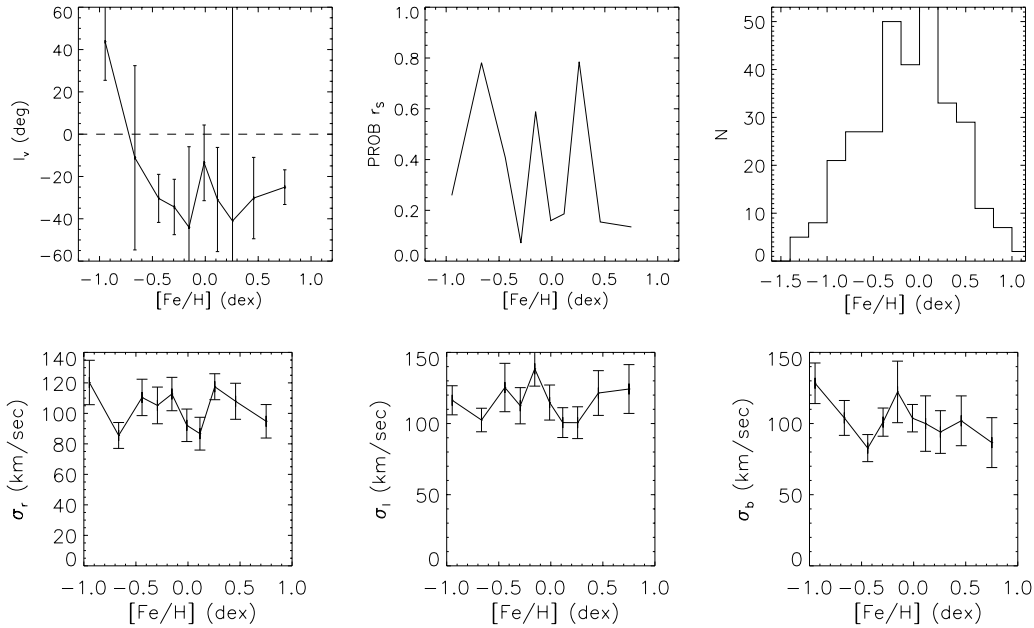


Figure 3.2: The kinematics as a function of metallicity. *Top row:* Left, Vertex angle l_v vs. $[\text{Fe}/\text{H}]$ using equal number of stars per metallicity bin; plotted bins are statistically independent. Center, the corresponding significance of the vertex deviation, using a non-parametric Spearman rank correlation. The combined significance for all stars with $[\text{Fe}/\text{H}] > -0.5$ is greater than 99%. Right, histogram showing the number of stars in 0.2 dex $[\text{Fe}/\text{H}]$ bins. *Bottom row,* velocity dispersions in r , l and b , for the same metallicity bins.

new stars in this study the significance of this deviation has dropped). This difference between metal rich and metal poor stars is a strong stellar-dynamical demonstration of the existence of a stellar bar in the galactic center (Binney et al. 1991; Zhao et al. 1994), and suggests that much of the disk takes part in it.

Fig. 3.2 shows the velocity dispersion components and vertex deviation as a function of the metallicity. Error bars have been estimated in every case using the Bootstrap Monte Carlo method. Interpreting the vertex deviation in terms of an orientation of the bar is complicated by the details of the stellar orbit distribution, and requires a full stellar-dynamical model

The Figure clearly shows a rather sharp transition near $[\text{Fe}/\text{H}] = -0.5$: more metal-poor stars show little or no deviation, whereas the more metal-rich stars' velocity ellipsoid is misaligned by about -30° , with a rank correlation between radial and longitudinal velocity components for these stars that is significant at the 99% level. A further indication of this change in kinematic properties is the dispersion in the (completely independent) vertical velocity component, σ_b , which shows a clear break at $[\text{Fe}/\text{H}] = -0.5$ with the more metal-poor stars' b velocity dispersion being higher.

We have also examined the correlations between the b velocity and the other components, but found no significant deviation of the velocity ellipsoids out of the plane.

The giant stars thus consist of a metal-rich population with a significant vertex de-

Table 3.1: Velocity ellipsoid parameters..

[Fe/H]	σ_r km/sec	σ_l km/sec	σ_b km/sec	l_v deg	r_S	N	N_{rej}	$Prob\ r_S$
All	107±4	116±4	106±5	-32±7	-0.15	315	21	0.0085
<-0.5	104±6	104±7	118±10	32±13	+0.10	77	11	0.3894
>-0.5	105±5	118±5	101±6	-34±7	-0.23	238	11	0.0002

viation of 30 degrees, and a metal-poor population that has no significant deviation, and hotter kinematics.

The general trend of the bulge to have this vertex deviation is also seen in three minor axis fields with proper motions from HST imaging with WFPC2 (Soto et al. 2010 in prep.). These fields were observed for radial velocities using the integral field spectrograph on VIMOS at VLT. The combination of radial velocities and l proper motions yields an observable vertex deviation in the fields (in samples not segregated by metallicity).

3.3 DISCUSSION

Our observations support the presence of a striking transition in the kinematics of the bulge, from an apparently isotropic oblate spheroid to a bar, at $[Fe/H] = -0.5$. We have used a non-parametric rank correlation statistic to determine that the significance of the vertex deviation for the metal-rich stars is $> 99\%$. There is a corresponding but shallower trend toward lower vertical velocity dispersion (σ_b) at higher abundance. It is difficult to imagine how a system with such a kinematic transition could be considered to have evolved in a one-zone chemical evolution scenario.

Do abundance trends of any other elements show a transition at $[Fe/H] = -0.5$? Examining the trends given in Fulbright et al. (2007) and Lecureur et al. (2007), we find no break in the trends of Mg, O, Ca, Si, Ti, Na, and $[Al/Fe]$ with $[Fe/H]$ that would correspond to -0.5 dex. Fulbright et al. (2007) consider the trend of the explosive alpha elements $\langle Ca + Si + Ti \rangle = \alpha_{exp}$ with $[Fe/H]$. They find that even to the lower limit of bulge $[Fe/H]$, at $[Fe/H] < -0.5$, the bulge trend of $[\alpha_{exp}/Fe]$ lies above the locus of halo and thick disk stars. Hence, the stars with $[Fe/H] < -0.5$ cannot be considered simply to belong to the halo or thick disk. Similarly, virtually all stars with $[Fe/H] > -0.5$ have strongly enhanced Mg, a strong indication that the chemistry reflects a history of rapid enrichment that extends through the boundary of this kinematic transition.

In order to form the bar via a stellar-dynamical instability, which then thickens into a bulge (Raha et al. 1991), the stars would already have to have been in place. The kinematics thus suggest a scenario in which all stars with $[Fe/H] > -0.5$ stars were formed in a disk *before* the bar instability occurred; the more metal-poor stars are then a population unrelated to the disk, bar and bulge, consistent with their hotter kinematics. But the continuity in bulge abundance trends across $[Fe/H] = -0.5$ argues against the existence of two entirely separate populations with different chemical evolution

histories. Evidently the situation is more complicated than a simple few-component model can describe. It is clearly important to explore the existence of these trends in larger samples and in additional fields in the bulge.

REFERENCES

- Beers, T., Sommer-Larsen, J. 1995, *ApJS*, 96, 175
- Binney, J., Gerhard, O.E., Stark, A.A., Bally, J., Uchida, K. 1991, *MNRAS*, 252, 210
- Binney, J., Gerhard, O., & Spergel, D. 1997, *MNRAS*, 288, 365
- Blitz, L. & Spergel, D.N. 1991, *ApJ*, 379, 631
- Burstein, D., Faber, S.M., Gaskell, C.M., Krumm, N. 1984, *ApJ*, 287, 586
- Cunha, K., Smith, V.V. 2006, preprint astro-ph/0607393
- Dwek, E., et al. 1994, *ApJ*, 445, 716
- Englmaier, P., and Gerhard, O. 1999, *MNRAS*, 304, 512
- Faber, S.M., Friel, E.D., Burstein, D., Gaskell, C.M. 1985, *ApJS*, 57, 711
- Feltzing, S., Bensby, T., & Lundström, I., 2003, *A&A*, 397, L1
- Ferreras, I., Wyse, R. F. G., & Silk, J. 2003, *MNRAS*, 345, 1381
- Fulbright, J. P., McWilliam, A., & Rich, R. M. 2006, *ApJ*, 636, 821
- Fulbright, J. P., McWilliam, A., & Rich, R. M. 2007, *ApJ*, 661, 1152
- Fuhrmann, K. 1998, *A&A*, 338, 161
- Gratton, R.G., Carretta, E., Matteucci, F., & Sneden, C. 2000, *A&A*, 358, 671
- Häfner, R., Evans, N. W., Dehnen, W., & Binney, J. 2000, *MNRAS*, 314, 433
- Kozłowski, S., Woźniak, P. R., Mao, S., Smith, M. C., Sumi, T., Vestrand, W. T., Wyrzykowski, Ł.
- Kuijken, K., & Rich, R. M. 2002, *AJ*, 124, 2054
- Lecureur, A. et al. (2006), astro-ph/0610346
- Majewski, S. 1992, *ApJS*, 78, 87
- Matteucci, F., Romano, D., & Molaro, P. 1999, *A&A*, 341, 458
- McWilliam, A., & Rich, R. M. 1994, *ApJS*, 91, 749
- Minniti, D. 1996, *ApJ*, 459, 175
- Raha, N., Sellwood, J. A., James, R. A., & Kahn, F. D. 1991, *Nature*, 352, 411
- Ramírez, S. V., Stephens, A. W., Frogel, J. A., & DePoy, D. L. 2000, *AJ*, 120, 833
- Rich, R.M. 1988, *AJ*, 95, 828
- Rich, R.M. 1990. *ApJ*, 362, 604
- Rich, R.M., Origlia, L. 2007 *ApJ Letter* submitted
- Sadler, E.M., Rich, R.M., Terndrup, D.M. 1996, *AJ*, 112, 171 (Paper II)
- Sharples, R., Walker, A., & Cropper, M. 1990, *MNRAS*, 246, 54
- Spaenhauer, A., Jones, B.F., Whitford, A.E. 1992, *AJ*, 103, 297

Sumi, T., et al. 2004, MNRAS, 348, 1439

Terndrup, D.M., Sadler, E.M., Rich, R.M. 1995, AJ, 110, 1174

Thomas, D., Maraston, C., Bender, R. 2003, MNRAS, 339, 897

Zhao, H., Spergel, D.N., Rich, R.M. 1994, AJ, 108, 2154

Zhao, H.S. 1996, MNRAS, 283, 149

Zoccali, M., et al. 2003, A&A, 399, 931

CHAPTER 4

A Schwarzschild model for three minor-axis fields

M. Soto, K. Kuijken
to be submitted

The study of the galactic bulge is interesting for a number of reasons. However, in spite of its proximity, many of its characteristics still remain veiled, unknown or undetermined due to the limitation of our observations and techniques. We are embarked on a project to determine the 3-dimensional kinematics in several low foreground extinction windows of the galactic bulge. This chapter presents a stellar-kinematic model which has been specially developed to reproduce the proper motion - photometric parallax observed distribution of 45000 stars in three fields across the galactic minor axis. A grid of 25 self-consistent Schwarzschild models has been run. We have focused on the determination of important bar parameters, such as bar inclination ϕ_{bar} and bar pattern speed Ω_b . We have found consistency between our best fit results and those for recent studies. Our models suggest that the most probable scenario to reproduce our data comes from a bar rotating at $40 \text{ km s}^{-1} \text{ kpc}^{-1}$ and a bar inclination of $30^\circ - 40^\circ$ with its near end in the first galactic quadrant.

4.1 INTRODUCTION

Our galactic bulge is a bar. Since this idea was first proposed by de Vaucouleurs (1964), evidence for it has grown considerably. Nevertheless, uncertainties still remain in the determination of the main structural parameters which define the stellar bulge/bar. A major difficulty is the high extinction towards the galactic bulge, which limits the optical work to a few “windows”. The new generation of instruments seems to be improving this situation; better, more powerful instruments are now able to sample a significant part of the stellar bulge and observe regions for which little information was previously obtained.

The question of whether the Milky Way is barred was revived by the work of Blitz & Spergel (1991) and Binney et al. (1991), who showed on the basis of near-IR maps and CO kinematics that the observed asymmetries could be explained by such a model. These results were spectacularly confirmed by the measurements from COBE/DIRBE (Dwek et al. 1995), showing that our galactic bulge is a boxy structure with its closer end in the first galactic quadrant. Further evidence has accumulated since then with the calculations of optical depths derived from gravitational microlensing (Zhao et al. 1995), asymmetries from star counts (Stanek et al. 1994, Babusiaux & Gilmore 2005) and stellar velocities for small samples in low extinction fields (Zhao, Spergel, & Rich 1994). Broadly speaking, a bar oriented at 20° to the line of sight with its nearest point in the first galactic quadrant and radius up to ~ 3 kpc is a good description of the data. However, a more recent determination undertaken with infrared star counts by the *Spitzer Space Telescope* (Benjamin et al. 2005) has revealed a different scale for the bar structure; infrared star counts favour a longer bar of ~ 4.4 kpc at an angle of $\sim 44^\circ$. Such differences in the determinations of bulge structural parameters have a direct impact on the dynamical conditions of the bar such as resonances or corotation radius. It has been suggested by N-body simulations that the size of bars is related to its evolutionary stage to some extent (Combes 2007); the bar can form initially from an instability in the disk, gas is driven inside the corotation radius by the bar torques, after which the gas reciprocates by torquing the bar. As a result the internal orbital structure of the bar changes, enhancing the frequency of chaotic orbits. The net result is that the bar grows gaining mass and slowing down until it destroys itself. The cycle can repeat when a new smaller bar can be formed again in a secular process.

In a similar way, stellar population studies also have played a role defining the bulge/bar. Stellar abundance studies over the years have confirmed that α -elements are enhanced in bulge giants, more precisely in Mg, Ti, Na and Al (McWilliam & Rich 1994, Rich & McWilliam 2000, Fullbright et al. 2007); similar trends have been also found with high-resolution spectra in other α -elements as O (Zoccali et al. 2006). The importance of these α -elements is related to the formation timescale of the galactic bulge. α -elements are produced during the explosion of SN Type II by short lived massive stars (timescales $< 10^7$ years), while SNe Type Ia explosion produce mainly iron. The latter are caused by progenitors that evolve on a timescale at least 1 order of magnitude longer ($> 10^8$ years; Tinsley 1979). Thus, the observed α -enhancements towards the galactic bulge also suggest a rapid formation scenario (< 1 Gyr; e.g. Ballero et al. 2007). Finally, this violent-rapid formation scenario is also in agreement with the

kinematics observed in bulge fields. Significant correlation between transversal proper motion and radial velocities has been found in BW's stars with a sudden change in the metallicity scale around -0.5 dex (see Chapter 3).

Several dynamical self-consistent models have been developed which try to reproduce the stellar properties in the Milky Way and other galaxies. The Schwarzschild method (Schwarzschild 1979, 1982) has been used in some of them. The Schwarzschild technique considers the bar basically as a collisionless stellar system, a realization of a distribution of orbits within the same potential¹, and involves adjusting the weights of collections of orbits in order to match the observations. The Schwarzschild's method was originally intended to reproduce the density distribution of triaxial galaxies, nevertheless its use was later on extended to other density distributions (e.g. Richstone 1980, 1984; Richstone & Tremaine 1984; Valluri et al. 2004; Schwarzschild 1982, 1993; Merrit & Fridman 1996; Zhao et al. 1996; Häfner et al 2000). Some of these first implementations of the Schwarzschild's method were designed to work on galaxies with spherical symmetry, which have four integrals of motion well defined (E, and the three components of L). Nevertheless, the applications of such models in real galaxies are limited. Subsequent results showed that even in axisymmetric galaxies, where two integrals of motion are known (E and L_z), a third integral of motion was important in order to reproduce realistic density distributions (Verolme et al. 2002). Particularly relevant in the development of Schwarzschild modeling for axisymmetric galaxies has been the work by the SAURON group (Bacon et al. 2001). They analyzed the kinematics of a sample of E and S0 galaxies, for which they implemented an extended Schwarzschild code which allowed them to study the phase-space distribution of the galaxies (Krajnović et al. 2005), and the central black hole when present (van de Bosch 2007). Their implementation of the Schwarzschild technique (e.g. Cappellari et al. 2006) was based on a parametrisation of the surface brightness distribution using a gaussian linear combination. In all the cases described the Schwarzschild method requires a complete orbit library, representative from the respective density distribution; in order to reach completeness such library must include the regular and irregular components of the phase-space. Bar/bulge models for the Milky Way, such as those by Zhao (1996b), Häfner (2000), and ours, combine both kinds of orbits, and in addition a triaxial potential rotating at a bar pattern speed Ω_b .

Previous dynamical models of the Galactic bulge were based on photometry and radial velocity data alone. In this paper we present an effort to construct a Schwarzschild model for the Milky Way which incorporates proper motion data as well. We expect such a model to be more robustly constrained by the data, as it is based on a higher-dimensional data set. For this work we use our new measurements of ~ 45000 stellar proper motions and photometry for three fields along the galactic minor axis.

The structure of this paper is as follows. In section 2, we explain the modeling technique based on the Schwarzschild method. Section 3 explains the different depro-

¹Since the two-body relaxation time is $t_{relax} \sim N t_{cross}/(8 \ln(N))$, where N is the number of stars and t_{cross} the crossing time, we can safely assume that our system is stable for a long time compared to the time for which our model is assumed to be collisionless. Therefore, the model of the galactic bar/bulge assumes that orbits are completely decoupled from each other and thus they can be considered as building blocks of the distribution of observables.

jection techniques applied to the COBE/DIRBE images in order to obtain a bulge/bar density distribution. Section 4 details the strategy used, the input information provided to the model and preliminary calculations to improve the overall robustness. Section 5 shows the results for a set of models and some variations to the fitting procedure. Section 6 summarizes our conclusions and describes possible further work.

4.2 MODELING TECHNIQUE

4.2.1 Formulation

In this section we explain the formulation and building of a steady-state model which fits a set of observables by means of the Schwarzschild technique.

Dynamical systems satisfy the collisionless Boltzmann equation, which means that they can be described by a distribution function that depends on six phase-space coordinates: three position and three velocity components. This is a direct consequence of the long 2-body relaxation time in such systems. The Boltzmann equation describes the motion of stars in a gravitational potential, Φ . At the same time we require that this potential be generated by the stars themselves, so we must also satisfy Poisson's equation in order to have a self-consistent solution. Furthermore, this distribution function can be written as a function of at most three *isolating integrals*, a result known as the strong Jeans theorem. Each set of values of these isolating integrals corresponds to a different orbit. The idea of using orbits (regular and irregular) as building blocks of real galaxies is used explicitly in the Schwarzschild technique (Schwarzschild 1979). Here we wish to model the bar of the Galaxy as a pattern-rotating, triaxial object. The problem is that these three integrals cannot be written down analytically: in fact some orbits are chaotic, and only obey one or two such integrals. With some notable exceptions, e.g. static Stäckel potentials (Binney & Tremaine 1994, p157), triaxial or pattern-rotating systems typically only have one analytic integral, E_J , the integral of Jacobi, which is

$$E_J = E - \frac{1}{2}\Omega_{bar}^2 R^2, \quad (4.1)$$

with Ω_{bar} the bar pattern speed, and R the radius in the plane of the bar rotation. A numerical approach to the problem is thus practically unavoidable.

In essence, the problem can be formulated as follows. Given a potential, we try to find a set of orbits which reproduce a given set of observables o_i , where $i = 1, \dots, n_{obs}$. For a broad class of observables this can be written as follows:

$$o_i = \sum_{j=1, N} \xi_{i,j} w_j, \quad (4.2)$$

where N is the number of orbits and $\xi_{i,j}$ is observable i due to orbit j and w_j is the weight of that particular orbit. Possible observables that can be reproduced in this way are three-dimensional or projected densities, luminosity-weighted mean velocities, etc.

We can rewrite eq.4.2 for a set of orbits as:

$$\sum_{i=1, n_{obs}} (o_i - \sum_{j=1, N} \xi_{i,j} w_j)^2 = 0. \quad (4.3)$$

Combined with the physical constraint that all orbit weights must be non-negative,

$$w_j \geq 0 \quad \forall j \quad (4.4)$$

this is the classical formulation of the Schwarzschild method, which can be viewed as the search for a feasible set in linear programming, a problem that usually has either a wide range of solutions, or none. By minimizing a cost function over the feasible solutions the method can be used to construct, for example, maximally rotating galaxies (e.g. Statler 1987).

For the present study we have measurements of individual stellar proper motions in a number of bulge fields, and our focus is on reproducing this observed distribution with a dynamical model. In particular our model tries to reproduce the full density distribution of the bulge/bar $\rho(x, y, z)$, and the distribution of two proper motions μ_l , μ_b , and a photometric parallax M_* , in our observed fields. The details of these data which are part of the input information of the model will be explained in detail in §4. The model presented in this paper fits four 3-D grids simultaneously. The first grid is the input density distribution obtained from a deprojection of the COBE DIRBE image, and the remaining three correspond to the distribution in proper motion and photometric parallax in each of our fields. Each grid consists of $32 \times 32 \times 32 = 32768$ cells which gives a reasonable definition of the bar structure. Consequently we can redefine eq.4.3 in a more realistic shape as:

$$\chi^2 = \sum_{f=1,4} \sum_{i=1,32768} (o_{f,i} - \sum_{j=1,N} \xi_{f,i,j} w_j)^2, \quad (4.5)$$

where f is here the number of the grid being fitted. This formulation of the problem as a least-squares minimization with the nonnegativity constraint on the weights is known as *quadratic programming*, and can be solved using a variation of the simplex algorithm developed for linear programming. It was introduced into galactic dynamics by Dejonghe (1989). In contrast to linear programming, this formulation of the problem will generally give a single optimal set of orbit weights.

4.3 DEPROJECTING THE BULGE DENSITY DISTRIBUTION FROM THE COBE MAP ONCE AGAIN

The near-IR images by the COBE-DIRBE experiment have already been the source of several deprojection models by different methods. Dwek et al. (1995) was the first to produce a 3-D density distribution from these images by using several analytical triaxial models to explore characteristics of the bar. More recently, studies as those performed by Bissantz & Gerhard (2002) using a more elaborated non-parametric maximum penalized algorithm, have found a bar with mass and size slightly different to

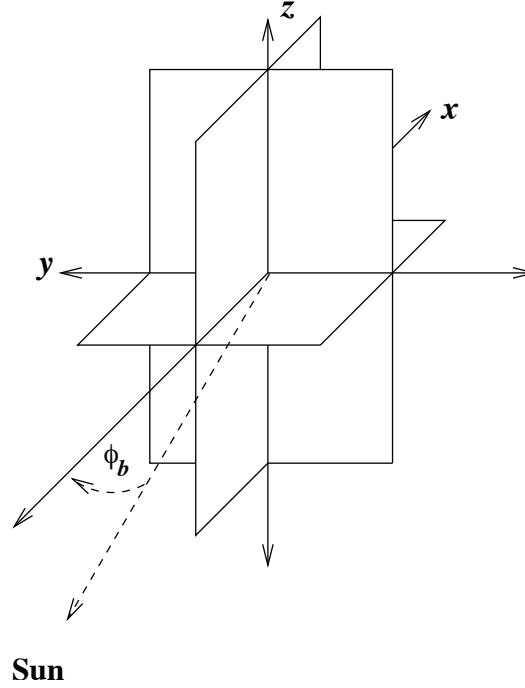


Figure 4.1: Eight fold symmetry assumed for our Schwarzschild model. Orbits have been calculated in the bar frame which is in an angle ϕ_b with the line connecting the sun with the galactic center.

those previously assumed. Those determinations have been more recently changed by Benjamin et al.'s (2005) work, which suggests an even larger bar according to their star counts from Spitzer data, as we have already mentioned in §1. Thus, the problem of the real dimensions of the bar is still an open discussion.

Our Schwarzschild model as explained before fits four 3-D grids simultaneously, where the first one (and the one which has the highest weight assigned) corresponds to the volume density distribution of the bulge. In order to acquire a representative density distribution for the galactic bulge we have performed our own deprojection from the COBE-DIRBE images.

4.3.1 Deprojection by analytical bars

Our deprojections by analytical bars consisted in each case in three components: a bar, a disk and a central cusp. Two disks have been tried, a double exponential, and a Miyamoto-Nagai (MN) disk (Miyamoto and Nagai 1975). The MN disk has the advantage that its potential can be calculated analytically. Thus, disk and cusp are given by the following form respectively,

$$\rho_d(R, z) = \left(\frac{e^{-|z|/z_0}}{z_0} + \alpha \frac{e^{-|z|/z_1}}{z_1} \right) R_d e^{-R/R_d} \quad (4.6)$$

$$\rho_c(x, y, z) = \eta r_c^{-1.85} \exp(-r_c) \quad (4.7)$$

Where $R_d = 2500$ pc, $z_0 = 210$ pc, $z_1 = 42$ pc and $\alpha = 0.27$ are the disk constants. In the case of the cusp, which corresponds to an oblate spheroidal nucleus with a steep power law and an exponential outer profile (Zhao 1996b), r_c corresponds to,

$$r_c = \left(\frac{q(R_0^2 + x^2 + y^2) + z^2}{c^2} \right) \quad (4.8)$$

Where q was set to 0.6. At the same time the disk can be written as

$$\rho_{MN}(R, z) = \left(\frac{\kappa^2 \beta}{4\pi} \right) \times \frac{[\lambda R^2 + (\lambda + 3\sqrt{z^2 + \kappa^2})(\lambda + \sqrt{z^2 + \kappa^2})^2]}{[R^2 + (\lambda + \sqrt{z^2 + \kappa^2})^2]^{5/2} (z^2 + \kappa^2)^{3/2}}. \quad (4.9)$$

Where a , b and κ are constants which control the shape of the disk. In the case of the bar we have chosen to try several analytical models to deproject the 3-D stellar density (Rattenbury et al. 2007). We have initially used :

$$\rho_{G1} = \rho_{b0} \exp(-r_{G1}/2) \quad (4.10)$$

$$\rho_{G2} = \rho_{b0} \exp(-r_{G2}/2). \quad (4.11)$$

Where r_{G1} and r_{G2} are

$$r_{G1}(x, y, z) = \left[\left(\frac{x}{a} \right)^2 + \left(\frac{y}{b} \right)^2 + \left(\frac{z}{c} \right)^2 \right]^{1/m} \quad (4.12)$$

$$r_{G2}(x, y, z) = \left[\left[\left(\frac{x}{a} \right)^2 + \left(\frac{y}{b} \right)^2 \right]^2 + \left(\frac{z}{c} \right)^4 \right]^{1/m} \quad (4.13)$$

The coordinate system has its origin in the center of the galaxy, with the xy plane the mid-plane of the galaxy and the z axis parallel to the direction of the galactic poles. The x direction defines the semi-major axis of the bar. In addition, our bar function is rotated in each deprojection in an angle ϕ_b to mimic the observed bar inclination. The constants a , b , c are the scale length of x , y and z respectively.

Our strategy consisted in the minimization of a χ^2 which compares the deprojection with the COBE DIRBE image. This minimization goes from 7 up to 10 free parameters depending of the combination of bar, cusp and disk. A powerful minimization algorithm was used in order to obtain a reliable set of values: MINUIT¹.

Table 4.1 summarizes the free parameters in each equation and figure 4.2 shows some of the different deprojections produced. Several bar types were probed during our preliminary models; in the final stage we constrained our analysis to one particular

¹available at <http://seal.web.cern.ch/seal/work-packages/mathlibs/minuit/home.html>

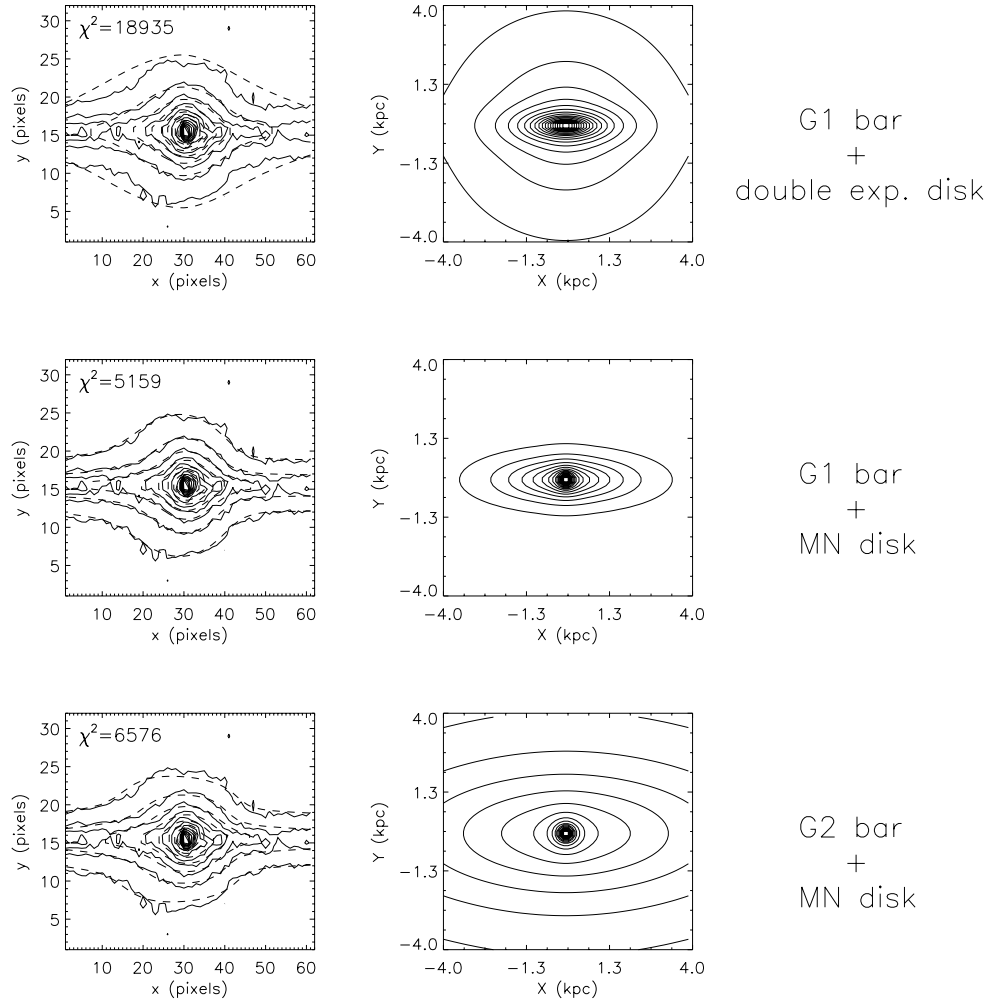


Figure 4.2: Some of the deprojection performed for the COBE-DIRBE images. *Top left*, contour image of the COBE-BIRBE image at $2.2\mu\text{m}$ (solid) superimposed over its respective deprojection (dashed lines) using a model with a central cusp, a double exponential disk and a G1 bar. The deprojection was performed assuming a $\phi_b = 20^\circ$. *Top right*, a view from the galactic north pole of the bar deprojected in the left panel. *Middle row*, same as top row, including a cusp, a Miyamoto-Nagai disk and a G1 bar deprojected at $\phi_b = 20^\circ$. *Bottom row*, Same order as upper rows, the model includes a Miyamoto-Nagai disk, a G2 bar, and a cusp. The parameters of the bars showed in the middle and bottom row can be seen in Table 4.2.

Table 4.1: Deprojection free parameters

Component	Free parameters
Bar-G1	ρ_{b0}, a, b, c, m
Bar-G2	ρ_{b0}, a, b, c, m
Disk-Double exponential	γ
Disk-MN	β, λ, κ
Cusp	c, η

model, due to its superior performance during the deprojection stage. These deprojections included several of the most commonly used density profiles for the galactic bar and disk (e.g. Rattenbury et al. 2007), where each equation has been slightly modified to include some free parameters (models G1 and G2 respectively). Clear differences have been found in the results of the deprojections according to the components chosen each time. Double exponential disk typically yield higher χ^2 , conversely, G1 and G2 bars have produced similar bars in size and volume density profile, with a slightly smaller χ^2 for the former, as table 4.2 and figure 4.2 shows. Also, the bars in our deprojections tend to have smaller axis ratio than some found before (e.g. Binney, Gerhard & Spergel 1997), nevertheless small bars have been also found recently by (Rattenbury et al. 2007) using OGLE-II red clump giants stars. Additionally, our bar compensates its relative smaller axis ratio by having smaller values of the exponent m in eq.4.12 and eq.4.13. These values make the bar density profile decay more slowly. Deprojections within the range of $\phi_{bar} \sim 20^\circ - 40^\circ$ have shown a reasonable consistency. Our bars show a ratio of semi-major and semi-minor bar axis scale lengths in the galactic plane a, b , and vertical bar scale length c which is $a : b : c = 10 : 3 : 3$. Thus, due to the consistency of the deprojections we have chosen one of our bars to generate a complete grid of models. This bar, which includes the oblate central cusp, the Miyamoto Nagai disk and the G1 bar will be referred as G1 model henceforth.

4.3.2 Potential formulation

Having fitted the density distribution of the bulge/bar, next we require a potential which is consistent with such density in order to integrate consistent orbits. We have done this by producing a multipolar expansion of the density (Englmaier & Gerhard 1999). Accordingly, we can write our 3-dimensional potentials as:

$$\Phi(r, \theta, \varphi) = -G\rho_0 \sum_{l,m} \Phi_{lm}(r) P_{lm}(\cos(\theta)) \cos(m\varphi) \quad (4.14)$$

We only include terms with even l and m to enforce reflection symmetry. Our potentials are derived from photometric models for the Galaxy and so involve an unknown mass-to-light ratio which can be adjusted through the parameter ρ_0 . We normalize it by forcing the circular speed of the Galaxy to match the observed 200 km s^{-1} at 8 kpc (Kui-

jen & Tremaine 1994), thus the mass of our bulge model corresponds to $\sim 2 \times 10^{10} M_{\odot}$ for a $\rho_0 = 366 M_{\odot}/I_{2.2\mu m}$.

Our decomposition of the potential in multipole components follows the procedure used by Englmaier & Gerhard (1999) for their 2-dimensional hydrodynamical model of the Milky Way. In order to obtain the multipole components of the potential, we start calculating the multipole components of the density distribution ρ_{lm} , these are

$$\rho_{lm}(\mathbf{r}) = \int_0^{\pi} d\theta \sin(\theta) P_{lm}(\cos(\theta)) \int_0^{2\pi} d\varphi \cos(m\varphi) g(\mathbf{r}) \quad (4.15)$$

Where g is the deprojected density distribution of the galactic bulge obtained before, which is related with the density by

$$\rho(r, \theta, \varphi) = \rho_0 g(r, \theta, \varphi), \quad (4.16)$$

Integrations in eq.4.15 were performed with the Romberg method for multipole components satisfying eight-fold symmetry as mentioned before (this was done typically until $l = 6$, which means 10 multipole terms). The $\rho_{lm}(r)$ tables were calculated for 8000 logarithmically equidistant radii between 1 pc and 12 kpc. Using those $\rho_{lm}(r)$ tables two integrals which will be used later were calculated,

$$I_{int}(r) = \int_0^r \rho_{lm}(s) s^{l+2} ds, \quad (4.17)$$

$$I_{ext}(r) = \int_r^{\infty} \rho_{lm}(s) s^{-(l-1)} ds \quad (4.18)$$

Armed with our auxiliary integrals we can then calculate the potential multipoles Φ_{lm} ,

$$\Phi_{lm}(r) = (2 - \delta_{m0}) \frac{(l-m)!}{(l+m)!} [r^{-(l+1)} I_{int}(r) + r^l I_{ext}(r)], \quad (4.19)$$

and their first derivatives

$$\Phi'_{lm}(r) = (2 - \delta_{m0}) \frac{(l-m)!}{(l+m)!} [-(l+1)r^{-(l+2)} I_{int}(r) + l r^{l-1} I_{ext}(r)]. \quad (4.20)$$

Where the partial derivatives of eq.4.14 are

$$\frac{d\Phi}{dr} = -G\rho_0 \sum_{l,m} \Phi'_{lm}(r) P_{lm}(\cos(\theta)) \cos(m\varphi), \quad (4.21)$$

$$\frac{d\Phi}{d\theta} = G\rho_0 \frac{R}{r} \sum_{l,m} \Phi_{lm}(r) P'_{lm}(\cos(\theta)) \cos(m\varphi), \quad (4.22)$$

$$\frac{d\Phi}{d\varphi} = G\rho_0 \sum_{l,m} m\Phi_{lm}(r) P_{lm}(\cos(\theta)) \sin(m\varphi), \quad (4.23)$$

and which can be used in turn to calculate the Cartesian accelerations through $\mathbf{a} = -\nabla\Phi$,

$$a_x = -\frac{d\Phi}{dr}(x/r) + \frac{d\Phi}{d\varphi}(y/R^2) - \frac{d\Phi}{d\theta}[xz/(r^2 R)], \quad (4.24)$$

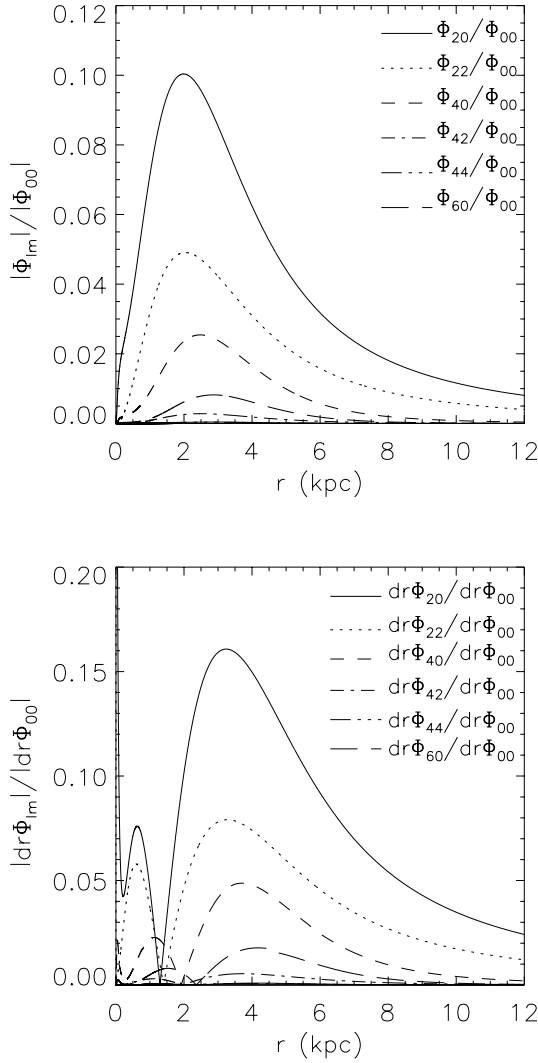


Figure 4.3: *Top*, relative contribution of multipole components Φ_{lm} in potential G1. 10 multipole components have been used to decompose the original potential. *Bottom*, relative contribution of derivatives of the multipole expansion $d\Phi_{lm}/dr$ of the potential, derivatives of multipole expansion are necessary to the calculation of forces in \hat{r} .

$$a_y = -\frac{d\Phi}{dr}(y/r) - \frac{d\Phi}{d\varphi}(x/R^2) - \frac{d\Phi}{d\theta}[yz/(r^2R)], \quad (4.25)$$

$$a_z = -\frac{d\Phi}{dr}(z/r) + \frac{d\Phi}{d\theta}(R/r^2). \quad (4.26)$$

Thus our forces in each case will be produced from a unique table containing the Φ_{lm} and Φ'_{lm} .

4.3.3 Orbit library

We have already mentioned that orbits can be considered as building blocks of the galaxy. Nevertheless, these building blocks can come in two flavors, regular and irregular. Regular orbits respect three isolating integrals of motion and therefore have “well

behaved" trajectories and are relatively simple to compute, whereas irregular orbits mostly respect only E_J as an integral, and therefore wander around in a 5-dimensional part of each constant- E_J slice of phase space, avoiding the regular orbits.

One way to include irregular orbits in the models is by using a special kind of orbits created to mimic the presence of these irregular components of the phase-space, composite orbits. Composite or "collective" orbits (Merrit & Fridman 1996; Zhao 1996b) are not orbits in the usual sense, but rather collections of many orbits with the same integral of motion. Therefore, in the case of triaxial models such as bars, a composite orbit will include all orbits with the same energy E_J , and will be independent of other integrals of motion. Hence, a model including regular and composite orbits will have a distribution function which is the sum of the distribution functions of regular (orbits with three integral of motion) and composite (one integral of motion) components explicitly. That is,

$$f = f_1 + f_3 = f(E_J) + f(\mathbf{I}).$$

Where E_J and \mathbf{I} represent the orbits with one and three integrals of motion respectively. Since the distribution function is time-independent, the same must apply for both components, composite and regular. Thus, we have that both components satisfy collisionless Boltzmann equation and are independent of time. Therefore, both can be considered as valid independent building blocks of the distribution function.

Nevertheless, there is a risk associated with including composite orbits in a library. Since composite orbits are entities which represent many orbits simultaneously, they can easily overpopulate our phase-space by selecting many types of orbits when assigning a particular weight to just one composite orbit. Due to the fact that composite orbits just depend on one integral of motion (E_J), a single composite orbit would fill completely a portion of the phase-space, including all regular orbits at that energy. To compensate this would require some regular orbits to have negative weights. While taking care to obtain a phase-space density positive everywhere. We have decided to avoid this complication by simply building orbit libraries that include a considerable number of orbits, regular and irregular. Our models contain between ~ 700 and ~ 4000 orbits depending on particular conditions of the bar modeled.

Orbit families

Families of regular orbits in a bar potential are well established. These orbit families are all related to resonances and can be even classified through them (Sellwood & Wilkinson 1993). Main regular orbit families are intrinsically related to resonances as corotation, inner Lindblad (ILR), outer Lindblad (OLR), or inner ultra harmonic resonances. Generally speaking, orbits in bar potentials tend to change orientation across every one of the resonances. The backbone of the bar structure is the $x1$ family of orbits, they commonly appear in simulations for 2-D bars, and even though they are less prominent in 3-dimensional bar simulations, where vertical instabilities arise (vertical resonances are found as often as horizontal), they still preserve a vital role in 3-dimensional bars. The $x1$ family of orbits is prograde and normally elongated along

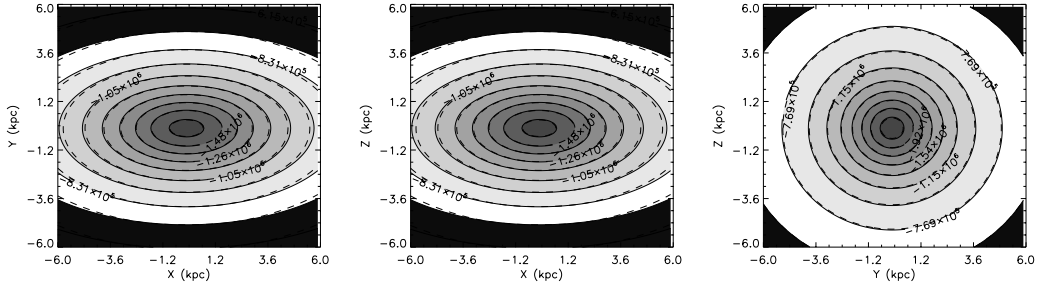


Figure 4.4: Performance of potential multipole expansion. In each plot contour solid lines correspond to an elongated analytical potential, dashed lines are from its respective multipole expansion including terms for $0 \leq l \leq 6$.

the bar at large radius and perpendicular at small radius. In addition, the $x1$ family of orbits has been associated by several authors with the boxy and peanut shapes observed in many galaxies (see Bureau et al. 2006, and references therein). More specifically, the $x1$ two main branches in the 2:1 vertical resonance form a “X” shape viewed side-on, that is transformed in a boxy bulge when projected in a different view angle. Since our bulge seems to have a boxy structure, as seen in the COBE-DIRBE images, a significant number of $x1$ orbits should be contained (and selected in the best solution) of our library. This has been found in previous models. Zhao (1996b) found a 40% of the latter orbits in the bars constructed by his model. Similarly, “banana” orbits should also play an important role in the bar structure, long-period banana orbits often appear around Lagrange points $L_{4,5}$ (see fig.4.5). Conversely, since the $x2$ and the $x3$ families of orbits are perpendicular to the bar, they have typically been considered of little importance in 3-D bars. The $x4$ retrograde family of orbits should also be present in our libraries and solutions as it has been observed in previous models. The $x4$ family seems very robust and little affected by resonances, existing from close to the center till the disk. A more detailed account on bar orbits can be found in Skokos et al. (2002) and Patsis et al. (2002). We will discuss the orbit families involved in our solutions and the implications for the models later in this chapter.

Orbit integration scheme

The initial conditions of our orbit library are similar to those in previous models (Schwarzschild 1979; Pfenniger 1984; Zhao 1996b). Orbits are launched perpendicularly to the y - z plane along the bar in both directions. In addition, a dynamical timestep has been calculated in each orbit considering the initial tangential force. The initial timestep has been set to $dt = 0.005 T$, where $T = (\mathbf{F}_r/r)^{1/2}$, the rotational period calculated from the initial force. Then, the orbit integration has been set to complete the equivalent of 10.000 rotational periods using an adaptive stepsize control algorithm with a required accuracy of $\sim 10^{-7}$ pc. Typically the latter precision yields changes in the integral of motion lower than $\sim 0.01 E_J\%$ at the end of the integration. The final orbits have been interpolated with a fourth order polynomial to regular timesteps to complete 2×10^6 steps per orbit.

At each integration step, we have recorded the density grid cell. Furthermore, when the projected position falls within $1.2'$ of one of our HST fields we record proper motions, radial velocities, and line of sight distances. Even though radial velocities have been recorded, these have been used to compare to existing data in the same field, rather than obtaining additional constraints to our models. In order to focus our attention in the bulge structure we have discarded orbits going beyond 5 kpc from the galactic center. Similarly, orbits with high energies, and therefore not sufficiently bound were not used.

Once the grid densities have been computed for all orbits in a library, our task is to find suitable weights $w_j \geq 0$ that reproduce the observations as accurately as possible (eq. 4.5). In order to ensure that the density of the model matches the potential as well as possible, we give the density grid a weight that is equal to the sum of the three kinematic grids. To further increase the modelling we impose eight-fold spatial symmetry on the cell densities of each orbit; this is justified by the symmetry of our bar model.

4.4 SCHWARZSCHILD MODELS

Since our goal is the determination of relevant bar parameters, specifically ϕ_{bar} , the angle between the sun line-of-sight to the galactic center and the major semi-axis of the bar, and Ω_b , the bar pattern speed of the bar, we have devised a strategy which consists in running a grid of libraries within the range in which we would expect our two parameters ϕ_{bar} and Ω_b to fall. Our grid spans $\phi_{bar} = 0^\circ$ until 40° in steps of 10°

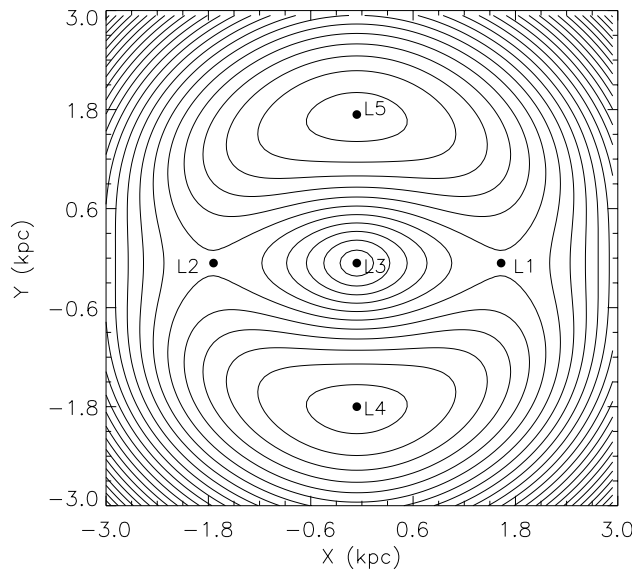


Figure 4.5: Effective potential for model G1 in a bar along the x axis rotating at $\Omega = 80 \text{ km s}^{-1} \text{ kpc}^{-1}$, showing the four usual Lagrangian points in the corotation region.

Table 4.2: Deprojected and chosen parameters for models

Parameter	G1	G2
a (pc)	947 ± 65	1490 ± 50
b (pc)	309 ± 20	580 ± 10
c (pc)	317 ± 20	400 ± 10
m	1.47 ± 0.05	4.0
ρ_{b0} (M_{\odot}/pc^3)	0.013 ± 0.001	0.0063 ± 0.00002
β ($M_{\odot} \times 10^8$)	7.5 ± 0.6	3.9 ± 0.01
λ (pc)	11185 ± 592	6500
κ (pc)	206 ± 3	260
η (M_{\odot}/pc^3)	0.009 ± 0.001	0.0063 ± 0.00002
χ^2	5159	6576

and $\Omega_b = 0$ up to $80 \text{ km s}^{-1} \text{ kpc}^{-1}$ in steps of $20 \text{ km s}^{-1} \text{ kpc}^{-1}$. The grid consisting of 25 complete libraries has been run for our best deprojection (§ 4.3.1), which includes a G1 bar plus a cusp and a Miyamoto-Nagai disk.

For different Ω_b , the libraries contain different numbers of orbits. Slow bars tend to contain many chaotic orbits, whereas the resonances of fast bars kick many orbits out of the grid. In order to provide a fair comparison between the different bar parameters we randomly subsample each library, limiting the number of orbits we fit to 1000. We have checked that different random subsamples lead to consistent results.

4.4.1 Proper motions and Photometric parallax

In addition to the proper motions, each kinematic grid includes a record of the distances of each star along the line of sight. This record has been obtained by using a photometric parallax for a subsample of turn-off and main sequence stars in each field. The slope of the CMD has been removed in each plot by means of the quantity M^* which corresponds to a crude distance modulus. The latter quantity is

$$M^* = m_{814} - \zeta \times (m_{814} - m_{555})$$

Where ζ for *Sagittarius-I* and *Baade's Window* fields is 2, and for *NEAR NGC 6558* field, which uses the F606W filter instead of F555W, is 3. This relative distance indicator M^* is corroborated by the smooth gradient of rotation observed for our three central fields in KR02 and K04, and is also consistent with radial velocity surveys which have revealed the rotation pattern for bulge population (see Minniti & Zoccali 2008, and references therein). Nevertheless, such rotation in practice might be blurred by the selection of stars, a pure bulge population is difficult to achieve since its population rapidly decreases at the same time disk and halo increase as one moves off axis. Our samples in the three minor axis fields clearly show the rotation of bulge dominated populations.

In order to compare the orbit grids with the kinematic data we need to understand the observational errors, and convolve the models with them. Both the proper motions, and the line of sight distances, have errors. For proper motions, we have assumed a typical error of 0.8 mas/yr, this value is consistent with the observed proper motion errors in our three minor-axis fields. For the distance modulus M_* on the other hand, we have calculated the observed error by field as it is illustrated in figure 4.6. For each field we have compared the distribution of stars along the line of sight with the distribution derived from the bar model chosen. As expected, the distribution from the model is always well defined with a sharper peak. Thus, we have used two free parameters in a Levenberg-Marquardt least-squares minimization to find the best fit parameters which convolve the model distribution. Model G1 yields a $\sigma_{M_*} \sim 0.3$ (mag) for Baade's Window and Sagittarius, and ~ 0.6 (mag) for Near NGC 6558.

This smoothing has been performed using a Gaussian kernel in the proper motion-photometric parallax grids for the $7^3 - 1 = 342$ adjacent pixels.

4.5 RESULTS OF THE SCHWARSCHILD TECHNIQUE

Figure 4.7 shows the χ^2 contour plot of the 25 libraries run for the G1 model. Several facts can be pointed out immediately from this plot. Firstly, a clear minimum can be observed for this model at $\phi_{bar} = 0^\circ$ and $\Omega_b = 60 \text{ km s}^{-1} \text{ kpc}^{-1}$, this minimum seems to be part of a zone with lower χ^2 , which roughly spans from $\Omega_b = 40$ to $60 \text{ km s}^{-1} \text{ kpc}^{-1}$. A secondary minimum in this zone can be observed for the models at $\phi_{bar} = 40^\circ$ and $\Omega_b = 40$ to $60 \text{ km s}^{-1} \text{ kpc}^{-1}$, which produces a χ^2 almost identical. Secondly, models with slow bars seem to be ruled out by the plot; bars as fast as $\Omega_b = 80 \text{ km s}^{-1} \text{ kpc}^{-1}$ can similarly be excluded.

We interpret the results (which are based only in proper motions) as a valley of solutions that runs from $\sigma_{bar} = 0^\circ, \Omega_b = 60$ to $\sigma_{bar} = 40^\circ, \Omega_b = 50$. Next we investigate whether the radial velocities can provide extra constraints that can be used to break the apparent degeneracy of models. Radial velocities allow us to measure vertex deviation and velocity dispersions σ_r and $\sigma_{r,l}$. Vertex deviation simply corresponds to the angle between the major axis of the velocity ellipsoid and the line of sight (Zhao, Spergel, & Rich 1994). In an axisymmetric potential the velocity ellipsoid must be aligned with the axis, thus the vertex angle l_v is 0° or 90° depending of the axis of the alignment. Any deviation of this situation necessarily implies triaxiality of the potential and in turn of the density distribution which generates it. Hence, vertex deviation is an indicator of triaxiality which has been repeatedly detected for stars of the galactic bulge. As shown in Zhao et al. (1994) and §3, a significant vertex deviation appears for samples of K and M giants in Baade's Window. More recently, we analyzed ~ 2000 radial velocities for stars in our three minor axis fields which correspond to the spectroscopic counterpart of the proper motions already obtained in KR02 and K04 (§2). A significant vertex deviation in these three fields has been found, with vertex angles of -41° , -40° and -17° for Baade's Window, Sagittarius-I, and Near NGC 6558 respectively. We would expect our best fit model to reproduce those signatures of triaxiality.

Figure 4.8 shows the predicted velocity ellipsoids and vertex angle(l_v) for the 5

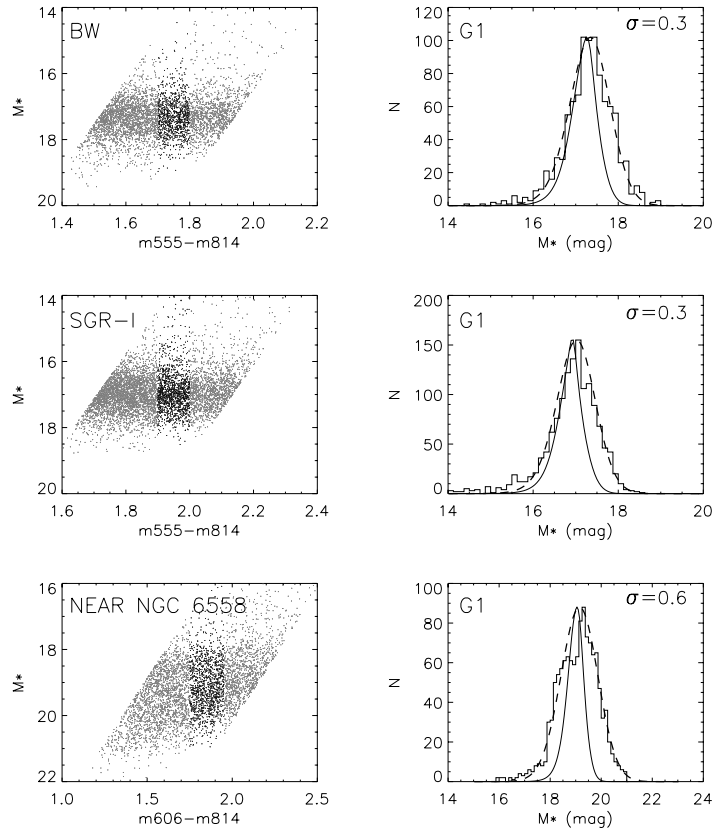


Figure 4.6: Calculation of the σ_{M^*} in our three fields. We have compared the distribution of stars along the line of sight with the prediction made for each model. *Top row left*, the selection of stars in Baade’s Window with photometric parallax determined, where a subsample (in black) has been used to build the histogram along the line of sight in order to reach completeness. (*Top right*), histogram for which we have found the best fit parameters (dashed) to match the real stellar distributions (histogram) with the initial prediction of G1 model (solid line). *Middle and bottom row*, same as top row but for fields Sagittarius-I and Near NGC 6558 respectively.

models with the lowest χ^2 of the G1 grid. In addition, table 4.3 shows the χ^2 and dispersions in r for the 25 models. Similar velocity ellipsoids to those in figure 4.8 have been obtained in chapter 2, for a subsample of turn-off and main sequence bulge stars, in our three minor axis fields (Figure 2.13). These “real data” velocity ellipsoids from chapter 2 can be directly compared with those obtained from the models. In general, we found that a bar inclination is needed in order to have a vertex deviation; velocity ellipsoids in models at $\phi_{bar} = 0^\circ$ point in the opposite direction of the real data velocity ellipsoids, that fact immediately allows us to rule out the best χ^2 model. Similarly, though more weakly, models at $(\phi_{bar}, \Omega_b) = (10^\circ, 60)$ and $(\phi_{bar}, \Omega_b) = (40^\circ, 60)$ can be discarded due to their strong disagreement in at least one of the vertex angle calculated in each field. In order to quantify those differences, which we have just described, we compared the dispersions σ_r and σ_{r_l} predicted for the grid of models with those found

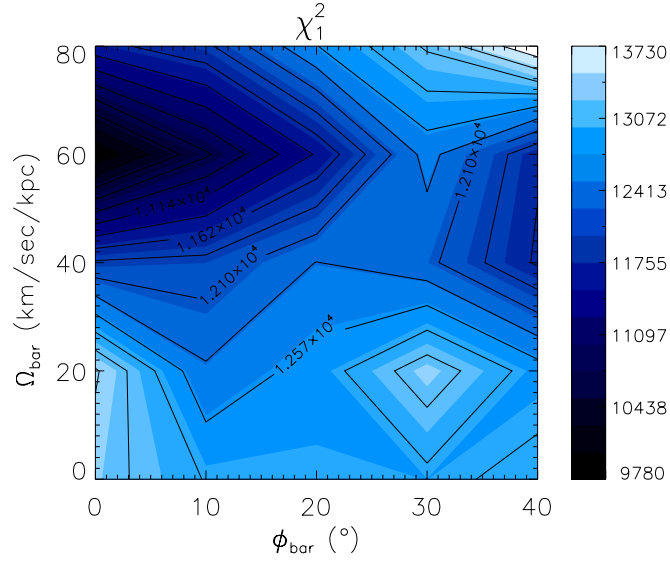


Figure 4.7: Contour plot for the grid of models using the G1 bar. Dark zones correspond to the models with small χ_1^2 .

in the chapter 2. Figure 4.9 shows the $\chi^2(\sigma_r)$ and $\chi^2(\sigma_{rl})$, we observe that $\chi^2(\sigma_r)$ in general favours bars with high inclination and rapid rotations, whereas σ_{rl} on the other hand roughly reproduces the minimums observed in figure 4.7 plus a new minimum at $(\phi_{bar}, \Omega_b) = (20^\circ, 40)$. When combined with equal weights they show a remarkable agreement with figure 4.7, the same two clear minimums at $(\phi_{bar}, \Omega_b) = (0^\circ, 60)$ and $(\phi_{bar}, \Omega_b) = (40^\circ, 40)$ appear; however the main minimum in this $\sigma_r + \sigma_{rl}$ grid has shifted to the model at $(\phi_{bar}, \Omega_b) = (40^\circ, 40)$ as we would expect accordingly to the velocity ellipsoids.

Thus, the best candidates for the G1 bar according to our grid seems to be the model at $(\phi_{bar}, \Omega_b) = (40^\circ, 40)$. Interestingly, this bar inclination has been pointed out previously under different techniques as the correct inclination of the bar, as we have already mentioned. The list of orbits minimized in this section do not have any preselection criterion. Nevertheless it might be interesting to explore if restricting our list of orbits in order to favour regular orbits, as previous work have done, significantly changes the results.

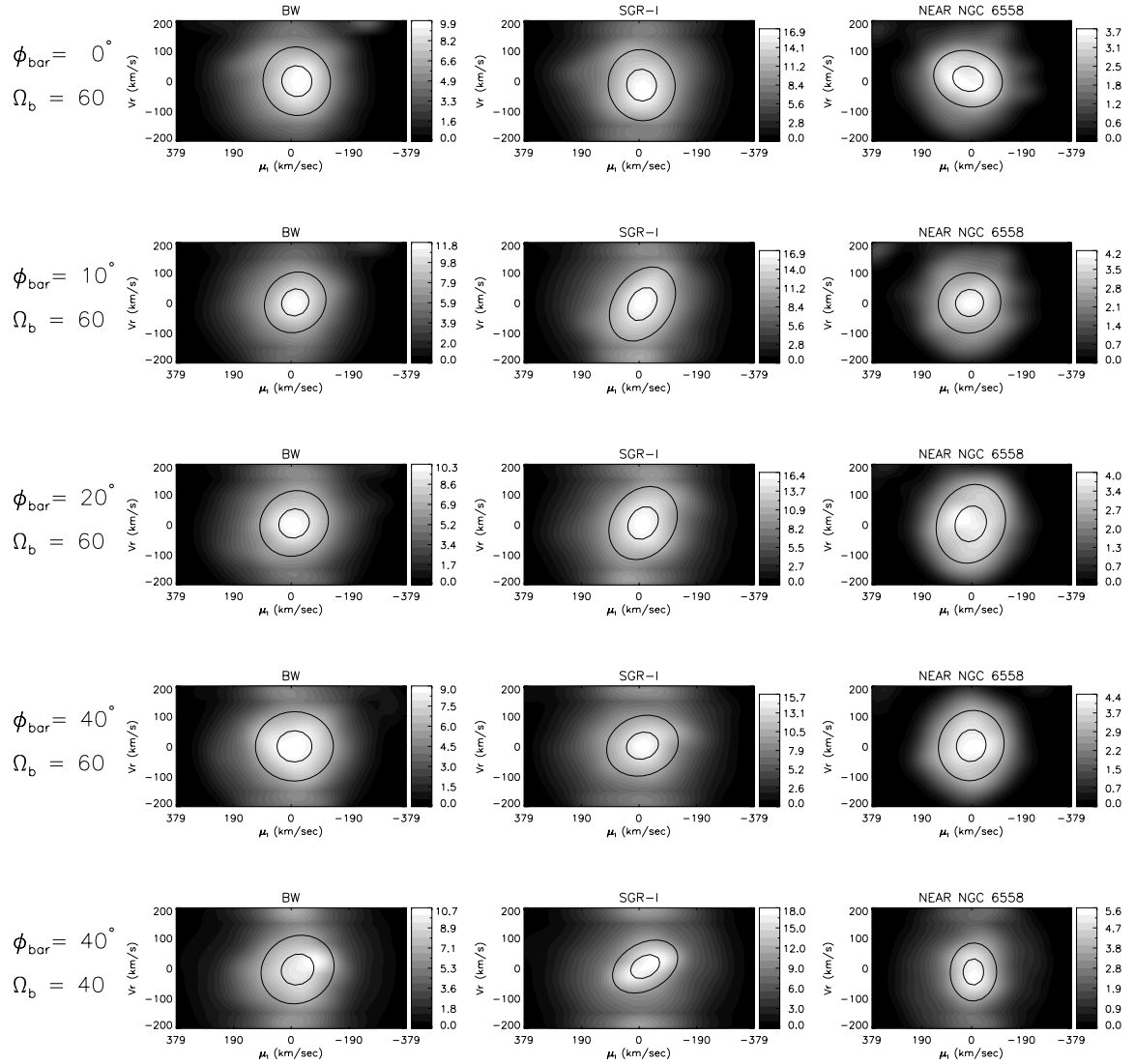


Figure 4.8: Transversal proper motion μ_l vs. radial velocity V_r for the three minor axis fields obtained from the 5 lowest χ^2 models in G1 grid. A two-dimensional Gaussian fit has been performed in each plot.

Table 4.3: Vertex angle and velocity dispersions in r for G1 models grid

ϕ_{bar} (deg)	Ω_b	χ^2_1	Baade's Window			Sagittarius-I			Near NGC 6558		
			l_v (deg)	σ_r	$\sigma_{r,l}$	l_v (deg)	σ_r	$\sigma_{r,l}$	l_v (deg)	σ_r	$\sigma_{r,l}$
0	0	13159	-0.5	85.4	-26.1	-88.9	93.7	-142.3	-86.7	104.1	-365.8
10	0	12796	-35.1	63.1	-4397.9	-82.3	64.1	-449.4	-78.8	66.7	-263.9
20	0	12774	-49.9	74.7	-4538.8	-93.5	44.4	-182.2	-84.9	76.1	-393.6
30	0	12741	-50.9	76.7	-4760.4	-39.3	74.1	-6640.9	-69.6	79.4	-2239.9
40	0	12895	-55.9	83.9	-3536.8	76.9	50.8	-85.5	-75.6	64.0	-947.0
0	20	13319	-179.6	82.7	34.0	-173.9	78.5	-95.1	-17.5	49.7	-1706.1
10	20	12371	-24.8	54.7	-3883.2	-6.0	78.7	-81.4	-31.6	56.8	-4489.7
20	20	12675	-16.6	50.4	-2188.2	-12.5	54.0	-1654.7	-7.1	61.7	-447.4
30	20	13203	-28.4	56.9	-5033.2	-42.6	78.5	-6657.9	-15.3	44.3	-1207.9
40	20	12691	-53.1	106.6	-7416.8	-61.8	106.8	-5872.5	-46.3	73.2	-5100.5
0	40	11897	-0.4	94.1	16.1	-179.0	80.7	28.3	-172.9	80.0	-225.3
10	40	11951	-13.5	49.6	-1586.7	-23.6	49.0	-3970.5	-45.5	88.4	-7670.8
20	40	12340	-19.9	47.8	-2908.9	-30.8	68.9	-3967.5	-13.5	55.2	-1008.3
30	40	12158	-42.8	76.8	-6223.2	-43.2	78.7	-6231.6	-36.1	55.9	-4110.0
40	40	11583	-62.8	99.6	-4171.6	-59.6	87.1	-4394.6	-11.0	56.2	-494.3
0	60	9780	56.2	65.1	-5509.3	-156.1	99.8	-3576.6	81.5	80.9	37.1
10	60	10630	-51.9	81.7	-5006.0	-37.4	71.1	-6606.3	-84.8	91.5	-368.9
20	60	11407	-58.5	93.9	-4771.6	-40.6	77.3	-6466.4	-52.7	102.3	-7498.1
30	60	12426	-69.1	109.8	-3905.0	-46.8	83.8	-6290.5	-69.0	110.4	-3965.1
40	60	11648	-86.8	96.0	-198.3	-71.6	101.7	-2896.8	-71.7	100.5	-2197.5
0	80	11531	-90.8	74.1	-39.9	-47.5	89.4	-7194.8	82.9	55.4	59.4
10	80	11803	-99.5	64.6	-860.3	-60.0	98.2	-5286.4	77.3	47.2	-152.2
20	80	12563	-61.9	106.6	-4804.8	-50.7	98.1	-7872.6	-122.3	36.7	-1957.9
30	80	13082	-62.1	110.7	-6144.8	-55.4	103.3	-7321.9	-34.3	39.9	-2252.3
40	80	13730	-60.3	115.8	-7442.1	-60.4	100.9	-5609.2	-47.6	52.9	-2321.9

Note: Bar pattern speed Ω_b in $km\ s^{-1}\ kpc^{-1}$, velocity dispersions σ_r in $(km\ s^{-1})$, and $\sigma_{r,l}$ in $(km^2\ s^{-2})$

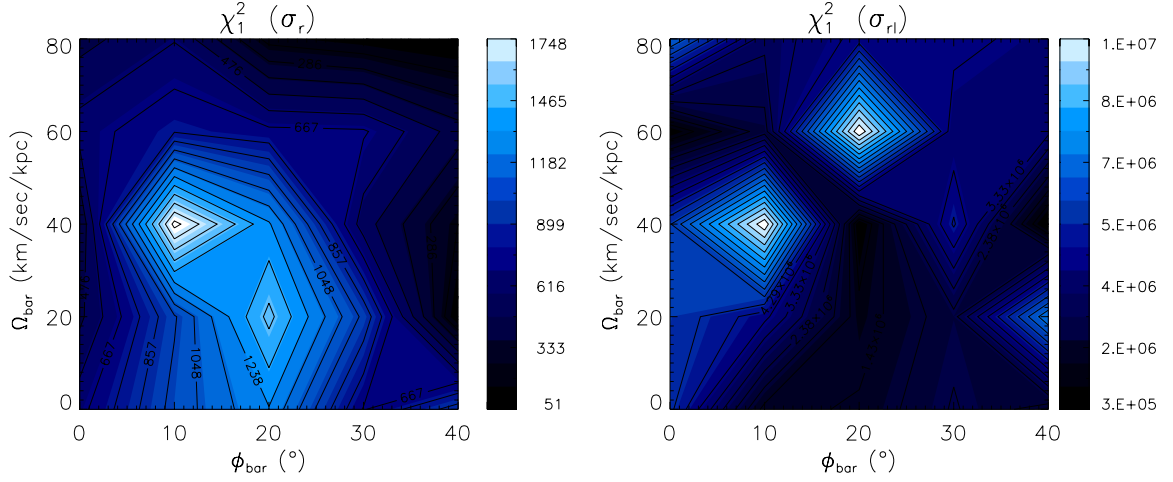


Figure 4.9: χ^2 contour plots of G1 models which compare the σ_r and $\sigma_{r,l}$ predictions from the models and those obtained in chapter 2, from a subsample of turn-off and main sequence bulge stars.

Orbit classification

A considerable fraction of each library must correspond to irregular or stochastic orbits. In our libraries this fraction increases as the bar becomes slower and under the influence of the central mass concentration (CMC). An orbit might be considered as ‘regular’ when its trajectory does not yield a significant change in its mass density distribution over a period of time longer than the one we expect our model to be stationary. This concept has been the base of the classification by Liapunov exponents, in this technique (e.g. Scheck 1980) the distance between pairs of close orbits is measured through the integration, in stochastic orbits the latter distance is expected to diverge exponentially.

In order to provide a similar classification we have devised a much simpler approach which is useful for orbits launched not in pairs. Our goal is not to overload our minimization matrix with stochastic orbits, which in general fill a significant number of cells in comparison with regular orbits. On the other hand the former orbits might be redundant since many of them tend to fill a similar fraction of the phase space which gives them a characteristic appearance. We performed a simple identification of those orbits by comparing the relative number of cells occupied in each of the grids sampled. In our tests this very simple approach has proven to be effective to separate the regular orbits from the irregulars that fill a considerable portion of the phase-space. Consequently, we have recalculated the NNLS best fit controlling the relative ratio of regular and irregular orbits. Figure 4.10 shows the contour plot for the grid of G1 models, 70% of the input orbit list were selected in this second minimization to be our so-called “regular” in order to favour a selection where the latter type prevails. The new minimization grid calculated including our orbit classification delivers χ^2 values consistent with the grid of non-classified orbits.

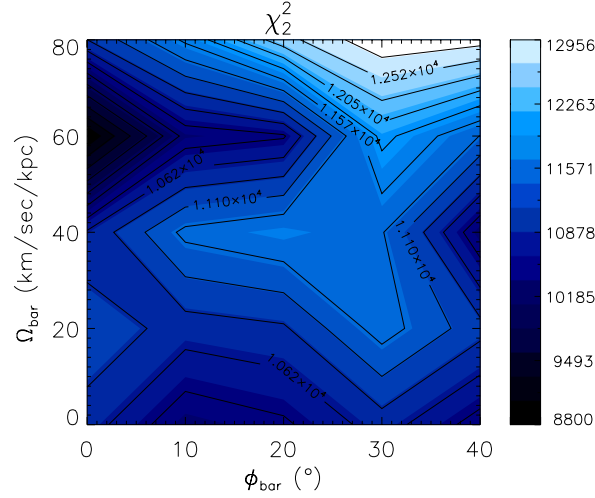


Figure 4.10: Contour plot for the grid of models using the G1 bar. A simple classification has been performed to control the relative ratio of regular and irregular orbits. In each library 70% of the orbits selected as input of the NNLS are regular.

As in the previous minimization grid we also calculated and compared the prediction of the models in σ_r and σ_{rl} with the values obtained in the chapter 2. The results are summarized in table 4.4 and figure 4.11. $\chi^2(\sigma_r)$ shows a similar behaviour than in the non-selected orbit library minimization grid. Conversely $\chi^2(\sigma_{rl})$ shows a slightly different distribution, where it has not preserved one of the three minimum observed at $(\phi_{bar}, \Omega_b) = (40^\circ, 40)$; in addition has favoured slower bars with small inclinations $(\phi_{bar}, \Omega_b) = (10^\circ - 20^\circ, 20)$. As a result of this small differences the combined best fit model (with equal weights) for the $\chi^2(\sigma_r + \sigma_{rl})$ is in this case at $(\phi_{bar}, \Omega_b) = (30^\circ, 40)$.

The values determined by the best fit model in the G1 grid are not a surprise. We have already indicated how the last determinations based on star counts in M and K giants using Spitzer counts by Benjamin et al.(2005) have found its best fit for a long bar at $\phi_{bar} = 44^\circ$. It is remarkable how our best model in spite of the differences in the bar dimensions agrees.

Figures 4.12, 4.13 and 4.14 show the best fit model at $(\phi_{bar}, \Omega_b) = (40^\circ, 40)$ on which we will focus in our subsequent analysis. In our models the percentage of stochastic orbits strongly depended on the bar pattern speed as expected; libraries for rapid bars at $80 \text{ km s}^{-1} \text{ kpc}^{-1}$ have $\sim 80\%$ of regular orbits whereas slow bars at $0 - 20 \text{ km s}^{-1} \text{ kpc}^{-1}$ only have $\sim 15\%$. This overabundance of stochastic orbits (which over long integration times have in many cases a similar appearance) has produced noticeable effects in the best fit in each model. In the case of our best model at $(\phi_{bar}, \Omega_b) = (40^\circ, 40)$ even though the fit is dominated in number of orbits by regulars (75% of the orbits with weights > 0 are regular), the stochastic component accounts by $\sim 80\%$ of the mass. Thus, the elongated bar shape is provided mainly by the smooth stochastic component rather than $x1$ regular family of orbits, as we could have expected according to previous models. The main role that regular orbits seem to play is to give a more realistic shape to the

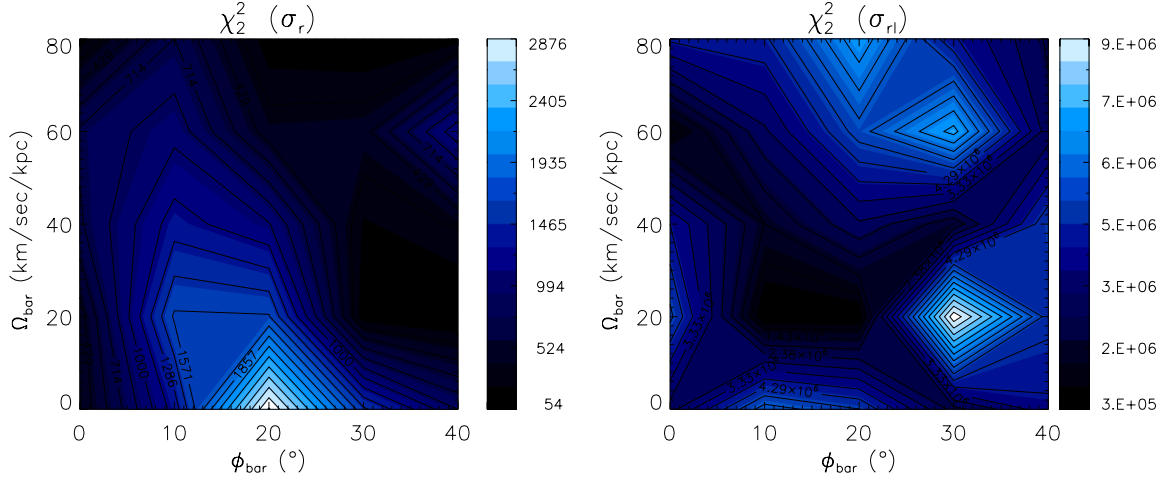


Figure 4.11: Same as figure 4.9 but using our orbit classification to force 70% of the orbits to be regular.

best fit, accounting for the details in the fit. Figure 4.15 shows the cumulative fraction of irregular and regular orbits as a function of the Jacobi energy E_J for the model at $(\phi_{bar}, \Omega_b) = (40^\circ, 40)$. Jacobi energy E_J measures roughly the radial extent of an orbit. Even though regular orbits seem to dominate at small radius, we know that our simple procedure to classify orbits should be ineffective to recognize stochastic orbits close to the center, therefore we would expect those regular orbits to be overestimated there. For larger radii both regular and irregular fractions steadily increase not showing a particular radius in which regular or stochastic orbits clearly prevail over the other type.

Comparatively, the bar pattern speed favoured by our best χ^2 is slower than those in previous bar models. Binney et al. (1991) determined a bar rotation of $81 km s^{-1} kpc^{-1}$, while Zhao (1996b) and Häfner used slower bars at $60 km s^{-1} kpc^{-1}$, thus our model predicts a bar at least $20 km s^{-1} kpc^{-1}$ slower. Evidence of a slower rotation than $60 km s^{-1} kpc^{-1}$ has already been suggested in previous models, Zhao's model encountered problems to fit observations at large radius, his model predicted too much rotation at large radii which could be solved by a slower bar, just as our grid of models predicts.

Our best fit results put forward two possibilities, the first is related to the bar model initially assumed; our deprojected bar is small and comparatively concentrates most of its mass within the 2.5 kpc radius. Hence, one can expect in advance that a considerable fraction of the orbits in the library are stochastic when the bar is sufficiently slow; this limits in turn the number of regular orbits. The latter problem is coupled with the fact that the central regions of the COBE DIRBE images are heavily obscured and hardly can be considered to satisfy a linear extinction relation, which might account for the overestimation of the mass in the unresolved central cusp of the bulge. In addition, our model has not explicitly avoided retrograde orbits, and mathematical incertainties based on our many free parameters used during the deprojection can also

be a source of risk. Nevertheless, if one assumes the feasibility of the bar input model, and considering the remarkable agreement with previous work respect to bar parameters, we might want to assume that these results suggest an actual particular formation scenario for the bulge/bar. If the bar has grown secularly from the thin disk, after a few dynamical rotation periods a considerable population would bend its trajectories to fill the phase-space in orbit families which spent a significant period of time away of the plane. Regular orbits far from resonances can survive adiabatic changes in the potential, the retrograde orbits on the other hand are a result of the scattering in resonances and potential fluctuations. This process can be enhanced by the central mass concentration and the gas inflow (Hasan et al. 1993) which has been pointed out has a crucial factor in the self-destruction of bars. Gas inflow is driven inside the corotation radius by the bar torques and reciprocally torques the bar (Combes 2007). This angular momentum loss makes the bar grow larger and slower until it finally destroys itself. Since that a considerable fraction of the orbits found in the bar are stochastic seems to indicate that the bar is in an advance evolutionary stage. On the other hand, the fact that stochastic orbits dominate the mass of the bar suggests a violent formation scenario where many regular orbits have not survived due to rapid changes in the phase-space.

4.6 SUMMARY AND FUTURE WORK

We have presented in this paper the results of a set of Schwarzschild models which attempt to reproduce the density, proper motion and photometric parallax distribution for the galactic bulge. Our data comprises ~ 45000 stars with proper motions lying in three low foreground extinction windows along the galactic minor axis and an input density distribution of the bar/bulge which comes from a deprojection of the dust-extinction corrected COBE-DIRBE images. The target has been fitted for a grid of 25 models which includes models with 5 different bar inclinations and 5 bar pattern speeds.

The results show two minima and exclude rapid bars or bars without rotation. In order to choose between one of the two minima at $(\Omega_b, \phi_{bar}) = (60 km s^{-1} kpc^{-1}, 0^\circ)$ and $(\Omega_b, \phi_{bar}) = (40 km s^{-1} kpc^{-1}, 40^\circ)$ we have tested the predictions of the models for the radial components of the dispersion tensor, comparing them with ~ 2000 radial velocities in the same fields. The results of this second set of constraints shows that a bar inclination is needed in order to obtain a vertex deviation. Thus, we have chosen $(\Omega_b, \phi_{bar}) = (40 km s^{-1} kpc^{-1}, 40^\circ)$ as the best fit in our grid of models. As an additional exercise we have explored the influence of limiting the percentage of stochastic orbit in our minimizations. We performed in each case a second minimization which forced each library to have 70% of regular orbits. This results have been consistent with those in the first minimization grid (which did not use any kind of orbit selection whatsoever). The results of this second minimization presents the same two minima, however when combined with radial velocities this second minimization grid shifts the second minimum at $(\Omega_b, \phi_{bar}) = (40 km s^{-1} kpc^{-1}, 30^\circ)$. It is remarkable that our models show a best fit which seems to agree with the last determinations of bar parameters. Ac-

According to our results the galactic bar presents a high inclination $30^\circ - 40^\circ$ in the first galactic quadrant and a moderate pattern speed of $40 \text{ km s}^{-1} \text{ kpc}^{-1}$. Additional analysis to our best model show that this bar is highly dominated by stochastic orbits, even when 75% of the orbits selected for the best fit correspond to regular orbits, they just provide $\sim 20\%$ of the total mass of the bar. Hence, the main structure of this model is given by elongated stochastic orbits which smoothly fill the phase-space, while more detailed features are reproduced by the regular component of the bar. We believe that these results suggest a bar formation scenario in which the bar has been formed from the disk and is in an advanced evolutionary stage, it has been slowed down and made more massive through angular momentum exchange and gas accretion. At the same time the central mass concentration play an important role in disrupting the orbits close to the center and increasing the frequency of stochastic orbits.

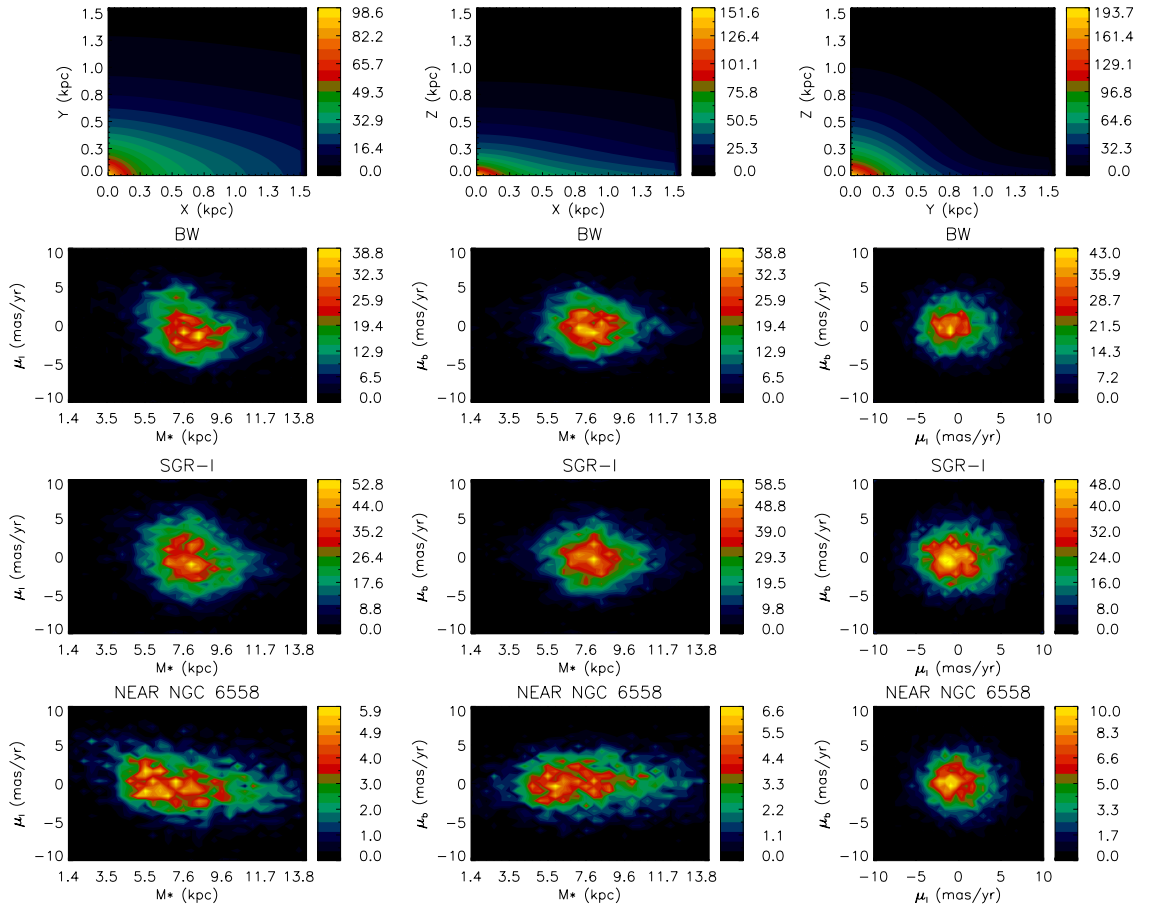


Figure 4.12: Contour filled plot with the target fitted in all the libraries. This target has been scaled to fit the models in each case.

Table 4.4: Vertex angle and velocity dispersions in r for G1 models grid using a rough orbit classification

ϕ_{bar} (deg)	Ω_b	χ_2^2	Baade's Window			Sagittarius-I			Near NGC 6558		
			l_b (deg)	σ_r	σ_{rl}	l_b (deg)	σ_r	σ_{rl}	l_b (deg)	σ_r	σ_{rl}
0	0	10739	40.5	87.3	-6450.7	-89.3	95.9	-100.4	-85.9	82.3	-205.5
10	0	10192	-32.4	68.6	-7034.9	81.4	48.0	13.5	-45.0	66.5	-4355.8
20	0	10336	69.6	27.5	-186.8	80.8	29.1	26.8	-105.2	32.7	-894.4
30	0	10738	-69.3	71.0	-1706.5	67.5	42.2	-989.6	-74.9	89.0	-2005.3
40	0	10269	-72.0	62.1	-544.0	-79.4	76.5	-818.1	-71.3	75.0	-1883.8
0	20	11042	-5.8	94.5	-97.4	-5.7	76.8	-148.9	-17.3	49.0	-1811.2
10	20	10739	-22.9	50.5	-3199.6	-18.8	47.8	-2778.5	-7.4	64.1	-119.5
20	20	10821	-19.1	49.5	-3128.8	-17.7	50.8	-2691.1	-16.5	44.3	-1618.9
30	20	11450	-43.4	97.2	-9090.3	-57.5	102.1	-5593.0	-43.8	70.3	-4961.2
40	20	10946	-54.3	104.6	-7853.5	-61.3	110.0	-6372.3	-77.7	70.8	-389.5
0	40	10655	-177.5	79.6	-11.7	-17.6	68.3	-1886.4	-90.0	77.8	-0.1
10	40	11402	-13.1	51.0	-1523.4	-28.9	66.3	-3643.1	-10.0	53.8	-878.7
20	40	11559	-9.9	61.5	-1294.3	-31.1	64.5	-4287.7	-30.8	51.1	-3123.1
30	40	11356	-55.2	92.8	-5905.4	-57.9	94.1	-5482.2	-10.3	53.1	-402.0
40	40	10181	-47.4	84.3	-6517.5	-53.2	89.1	-5930.5	-34.9	56.4	-4422.3
0	60	8800	-37.2	68.7	-5823.9	-68.8	97.6	-2736.1	-85.6	97.2	-438.6
10	60	10230	-33.8	58.7	-4595.1	-35.9	72.2	-7179.5	74.8	67.9	-1365.4
20	60	10350	-66.2	100.3	-3719.5	-35.3	73.4	-5770.2	-26.9	61.3	-5445.9
30	60	11892	-64.7	107.8	-4347.5	-51.0	93.1	-6514.2	-56.4	97.3	-6077.0
40	60	11327	-111.0	57.9	-3822.1	-64.5	95.0	-3130.2	-65.3	105.1	-4571.7
0	80	10854	89.8	91.3	11.9	-75.9	102.0	-1792.1	86.6	54.9	97.1
10	80	11621	-101.3	59.1	-1134.2	-52.2	94.4	-6868.5	75.9	44.7	-204.2
20	80	12434	-58.8	109.8	-7068.9	-50.7	102.4	-8572.3	76.5	37.4	-326.8
30	80	12956	-61.9	116.9	-6927.3	-57.9	103.1	-6575.2	-35.5	41.1	-2350.1
40	80	12856	-67.3	106.8	-3327.5	-53.4	98.9	-6435.6	-30.0	37.0	-2289.3

Note: Bar pattern speed Ω_b in $km\ s^{-1}\ kpc^{-1}$, velocity dispersions σ_r in $(km\ s^{-1})$, and σ_{rl} in $(km^2\ s^{-2})$

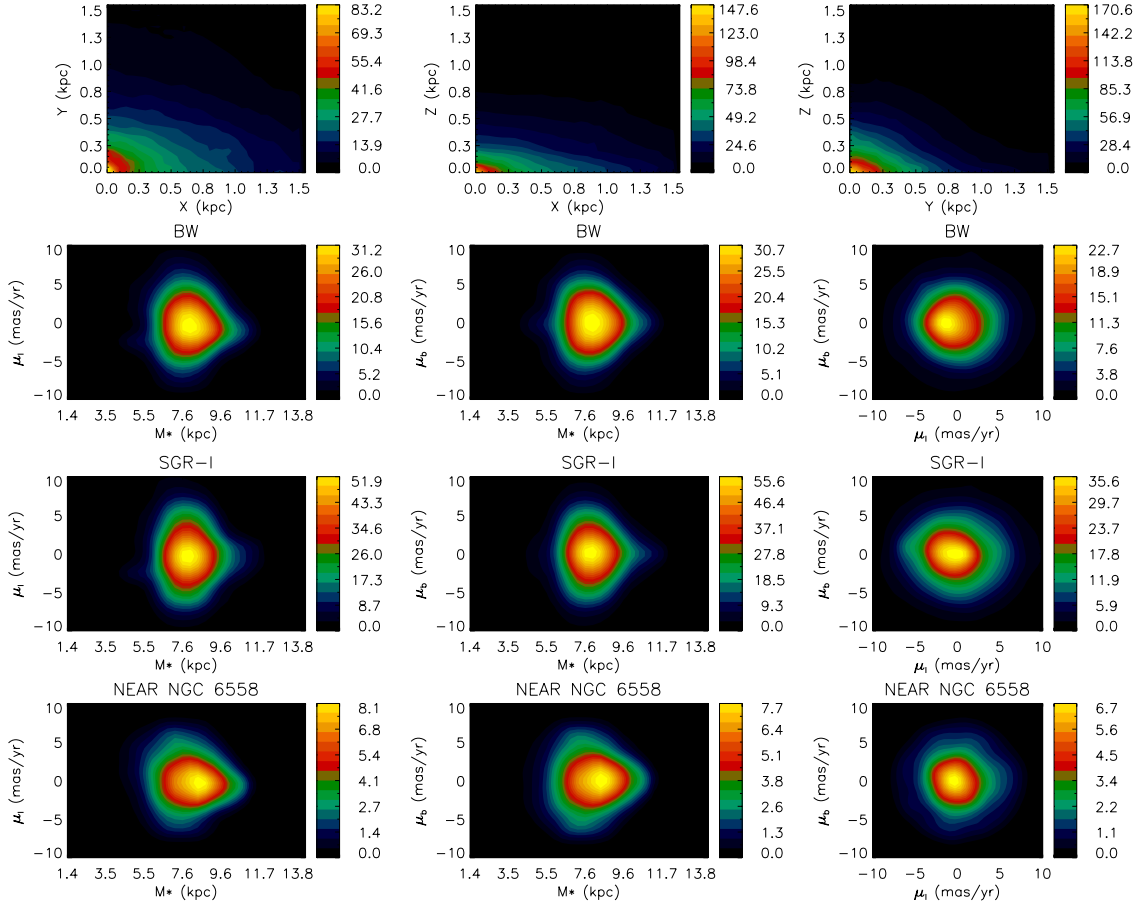


Figure 4.13: Best fit of one of the models in G1 grid at $\phi_{\text{bar}} = 40^\circ$ and $\Omega_b = 40 \text{ km s}^{-1} \text{ kpc}^{-1}$.

4.6.1 Future improvements in the model

In spite of our efforts and the number of constraints developed in our models at the present stage, we can recognize a number of future improvements which will be highly desirable. We can summarize those as follows:

- *Our input density distribution of the bar:* Our deprojection of the COBE DIRBE image has been using a simple analytical form; it does not account for asymmetries or the presence of spiral arms. Eight fold symmetry is just an ideal case.
- *Orbit classification:* Our orbits do not have an efficient classification scheme at all radii. An improved version of our code should take into account a suitable classification procedure which might include Liapunov exponents or similar.
- *Smoothing constraints:* Additional smoothing constraints might be given to the model. That will ensure smooth transitions between the families chosen in the NNLS for the best fit.
- *Orbit initial conditions:* Our library includes roughly ~ 4500 orbit initial conditions. A higher number of initial conditions could eventually improve the com-

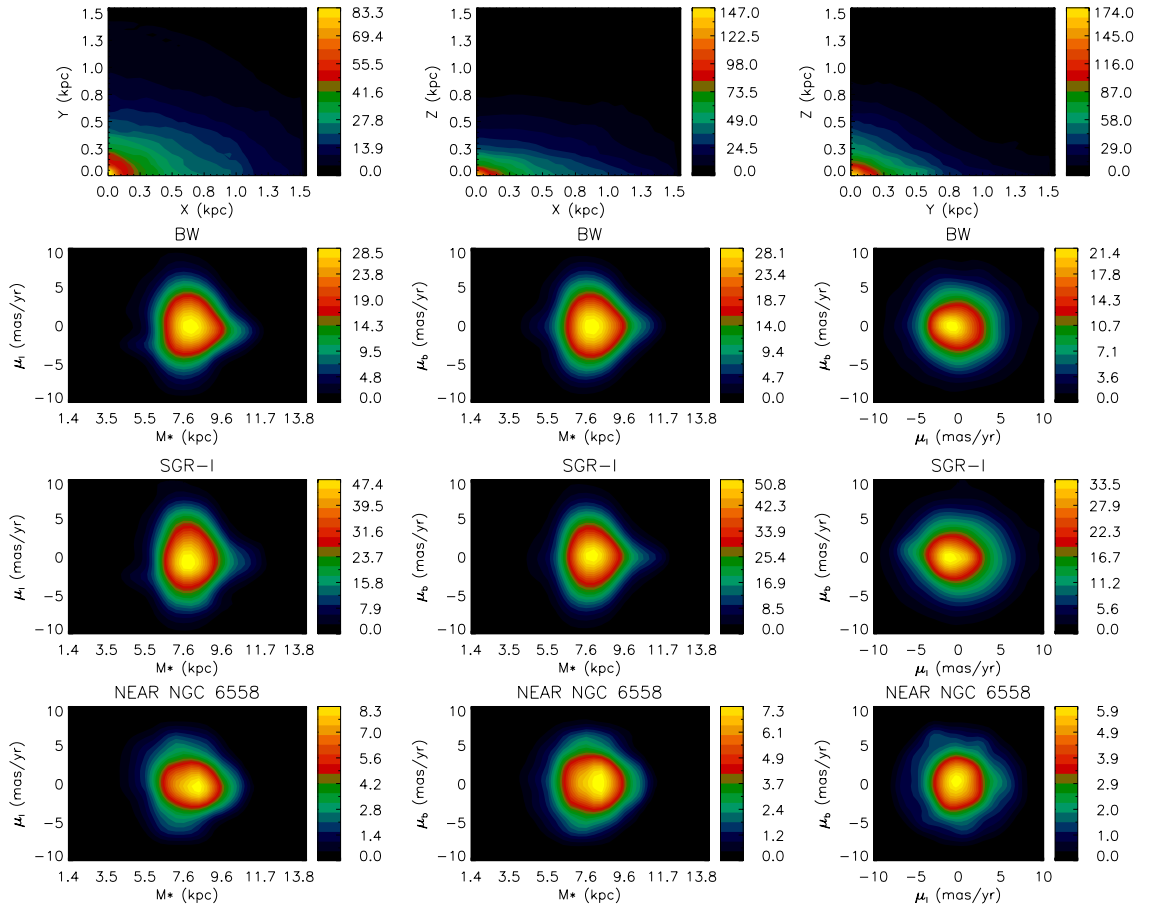


Figure 4.14: Same as figure 4.13, but using our orbit classification to force a 70% of the orbits to be regular.

pleteness of the library. A smaller number of rotations per star could be used in order to increase the number of orbits maintaining the time spent per run.

- *Radial velocities:* We have measured a considerable number of radial velocities in our proper motion fields. That information should be included in the constraints of the model. Even though numbers of radial velocities are much smaller (~ 2000) than the proper motion sample (~ 45000) they are statistically significant and therefore can be used with a suitable smoothing technique.
- *Additional fields on both sides of the bar:* We already have ~ 1000 radial velocities and ~ 10000 proper motions for three fields at positive longitudes. This information will significantly improve the quality of our constraints since it samples the near end of the bar.
- *N-body stability tests:* In order to guarantee that our best models are stable a N-body simulation is necessary. The latter will check, in addition to the overall stability over a significant dynamical time, the influence of the central mass concentration in the evolution of the system.

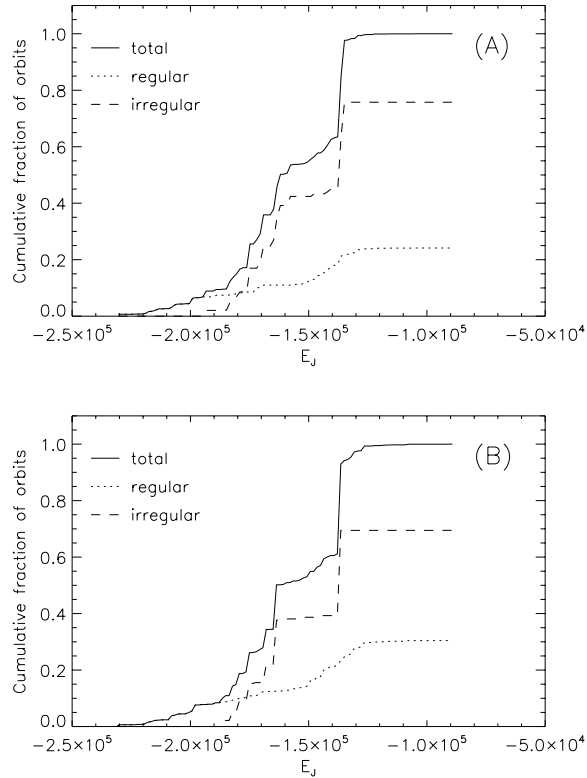


Figure 4.15: Cumulative fraction of orbits as a function of E_J for model at $\phi_{bar} = 40^\circ$ and $\Omega_b = 40 \text{ km s}^{-1} \text{ kpc}^{-1}$. (A), for first minimization, which does not include an orbit classification. (B), second minimization, in which we have forced each library to have 70% of regular orbits.

- *Zoom:* Our results have constrained the bar parameters to a relatively small range. Since we have discarded a considerable fraction of the $\phi_{bar} - \Omega_b$ plane as the most probable values for the galactic bar, we can zoom in the most probable range and to produce a finer grid of models in order to have a more precise determination of the actual bar parameters.

REFERENCES

- Arendt et al. 1994, ApJ, 425, L85
 Anderson, J., & King, I.R. 1999, PASP, 111, 1095
 Anderson, J., & King, I.R. 2000, PASP, 112, 1360
 Athanassoula, E. 2005, MNRAS, 358, 1477
 Bacon R., Copin Y., Monnet G., Miller B. W., Allington-Smith J. R., Bureau M., Carollo C. M., Davies R. L., Emsellem E., Kuntschner H., Peletier R. F., Verolme E. K., de Zeeuw P. T. 2001, MNRAS, 326, 23
 Ballero, S.K., Matteucci, F., Origlia, L., & Rich, R.M. 2007, A&A, 467, 123B

- Babusiaux C. & Gilmore G., 2005, MNRAS, 358, 1309
- Benjamin, R.A., et al. 2005, ApJ, 630, L149
- Binney J., Gerhard, O.E., Stark, A.A., Bally, J., Uchida, K.I. 1991, MNRAS, 252, 210
- Binney J., Tremaine, S. 1994, *Galactic Dynamics*, Princeton University Press
- Binney J., Gerhard O.E., Spergel D. 1997, MNRAS, 288, 365
- Bissantz N., Gerhard O. 2002, MNRAS, 330, 591
- Blitz, L., Spergel, D.N. 1991, 379, 631
- Bureau, M., Aronica, G., Athanassoula, E., Dettmar, R.-J., Bosma, A., Freeman, K. C. 2006, MNRAS, 370, 753B
- Cappellari, M., Bacon, R., Bureau, M., Damen, M. C., Davies, R. L., de Zeeuw, P. T., Emsellem, E., Falcón-Barroso, J., Krajnović, D., Kuntschner, H., McDermid, R. M., Peletier, R. F., Sarzi, M., van den Bosch, R. C. E., van de Ven, G. 2006, MNRAS, 366, 1126
- Combes, F. 2007, IAUS, 235, 19C
- Cudworth, K.M. 1986, AJ, 92, 348
- de Vaucouleurs, G., 1964, in Kerr F., Rodgers A., eds, Proc. IAU Symp. 20, The Galaxy and the Magellanic Clouds. Australian Academy of Sciences, Canberra, p. 195
- Dejonghe, H. 1989, 343, 113
- Dwek, E., et al. 1995, ApJ 445, 716
- Englmaier, P., and Gerhard, O. 1999, MNRAS, 304, 512
- Fullbright J. P., McWilliam A., Rich R.M. 2007, ApJ, 661, 1152F
- Hasan, H., Pfenniger, D., Norman, C. 1993, ApJ, 409, 91
- Häfner R., Evans N.W., Dehnen W., Binney J., 2000, MNRAS, 314, 433
- Holtzman, J.A., Watson, A.M., Baum, W.A., Gillmair, C.J., Groth, E.J, Light, R.M., Lynds, R., & O'Neill, E.J., Jr. 1998, AJ, 115, 1946
- Krajnović D., Cappellari M., Emsellem E., McDermid R. M., de Zeeuw P. T. 2005, MNRAS, 357, 1113
- Kuijken, K., Tremaine, S. 1994, ApJ, 421, 178
- Kuijken, K., Merrifield, M.R., ApJ, 443, L13
- Kuijken, K., & Rich, R.M. 2002, AJ, 124, 2054
- Kuijken, K. 2004, ASP, 317, 310K
- Merrit D., & Fridman T. 1996, ApJ, 460, 136
- McWilliam, A., Rich, R.M. 1994, ApJS, 91, 749
- Minniti D. 1993, IAUS, 153, 315M
- Minniti D. 1996, ApJ, 459, 175
- Minniti, D., & Zoccali, M. 2008, IAUS245, 323M
- Miyamoto M., & Nagai R. 1975, Publ. Astron. Soc. Japan, 27, 533
- Patsis, P. A., Skokos, Ch., Athanassoula, E. 2002, MNRAS, 337, 578
- Pfenniger D. 1984, A&A, 141, 171

- Rattenbury N.J., Mao S., Takahiro S., Smith M.C. 2007, MNRAS, 378, 1064
- Rich, R.M. 1988, AJ, 95, 828
- Rich, R.M. 1990, ApJ, 362, 604
- Rich, R.M., McWilliam, A. 2000, SPIE, 4005, 150
- Rich, R.M., Reitzel, D.B., Howard, C.D., Zhao, H. 2007, ApJ, 658, L29
- Richstone, D.O. 1980, ApJ, 238, 103
- Richstone, D.O. 1982, ApJ, 252, 496
- Richstone, D.O., & Tremaine, S. 1984, ApJ, 286, 27
- Rieke, G.H., & Lebofsky, M.J. 1985, ApJ, 288, 618
- Sadler, E.M., Rich, R.M., Terndrup, D.M. 1996, AJ, 112, 171
- Sellwood, J.A., Wilkinson, A. 1993, Dynamics of barred galaxies, Rep. Prog. Phys., 56, 173
- Spaenhauer, A., Jones, B.F., Withford, E. 1992, AJ, 103, 297
- Schwarzschild, M. 1979, ApJ, 232, 236
- Schwarzschild, M. 1982, ApJ, 263, 599
- Schwarzschild, M. 1993, ApJ, 409, 563
- Scheck, F., Mechanic, Berlin Heidelberg, Springer-Verlag, 1990
- Patsis, P. A., Skokos, Ch., Athanassoula, E. 2002, MNRAS, 333, 847
- Soto, M., Rich, R.M., Kuijken, K. 2007, ApJ, 665, L31
- Stanek K.Z., Mateo M., Udalski A., Szymánsky M., Kaluzny J., Kubiak M., 1994, ApJ, 429, L71
- Statler, T.S. 1987, ApJ, 321, 113S
- Terndrup, D.M., Rich, R.M., Sadler, E.M., 1995, AJ, 110, 1774
- Tinsley, B.M., 1979, ApJ, 229, 1046
- Tonry, J., & Davis, M. 1979, AJ, 84, 10
- Valluri, M., Merritt, D., Emsellem, E. 2004, ApJ, 602, 66
- van den Bosch, R.C.E. 2008, PhD Thesis
- Verolme E. K., Cappellari M., Copin Y., van der Marel R. P., Bacon R., Bureau M., Davies R. L., Miller B. M., de Zeeuw P. T. 2002, MNRAS, 335, 517
- Weiland, J.L., et al. 1994, ApJ, 425, L81
- Zeballos, H., Soto, M., Kuijken, K, Rich, R.M. 2008, (in preparation)
- Zhao, H.S., Spergel, D.N., Rich, R.M. 1994, AJ, 108, 2154
- Zhao, H.S., Spergel, D.N., Rich, R.M. 1995, ApJ, 440, L13
- Zhao, H.S., Rich, R.M., & Spergel, D.N. 1996a, MNRAS, 282, 175
- Zhao, H.S. 1996b, MNRAS, 283, 149
- Zoccali et al. 2006, A&A, 457L, 1Z

4.A BUILDING THE COBE / DIRBE IMAGE

The COBE-DIRBE data has been obtained from the COBE public database^a. This data comes sorted in a quadrilateralized spherical cube projection which contains all the sky. The information in the cube can be retrieved by means of several packages in different programming languages as FORTRAN 77 or IDL. Since we intend to obtain properties of the inner kpc of the galactic bulge we have limited the image used in the deprojection of the galactic bulge/bar to the central 62×32 pixels of the DIRBE image at a resolution of $0.32^\circ/\text{pixel}$. The images are available in 10 infrared bands, where we have centered our analysis in wavelengths 1.25, 2.2, 3.5 and $4.9 \mu\text{m}$. These wavelength are of particular interest, due to the fact that unreddened Galactic light (from bulge and disk) at that wavelength range exhibits colors similar to those of late K and M giants (Arendt et al. 1994), which should be the dominant population in our bulge observations. Armed with the COBE-DIRBE image we have repeated the analysis by Arendt et al. (1994) and Weiland et al. (1994) to clean the images of interstellar extinction.

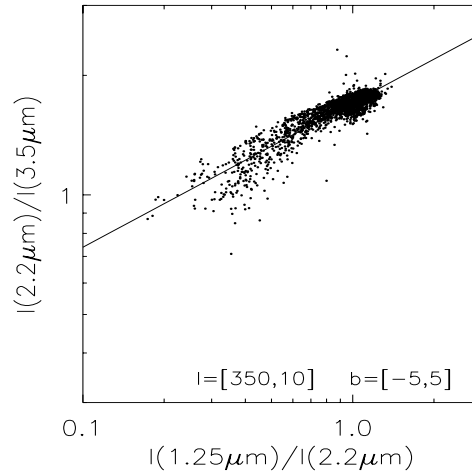


Figure 4.16: Near-IR color-color diagrams in the central region $l = [-10^\circ, 10^\circ]$ and $b = [-5^\circ, 5^\circ]$ of the COBE-DIRBE image

Figure 4.16 shows the extinction law for the COBE images in four filters and the inner $|l| \leq 10^\circ$ and $|b| \leq 5^\circ$. In order to compute the extinction-corrected intensity maps we have assumed both that the slope in figure 4.16 is unique and that all the sources have the same intrinsic colors, where the variations observed are related with foreground extinction. That is,

$$\frac{-2.5 \log(I_{2.2}/I_{3.5})}{-2.5 \log(I_{1.25}/I_{2.2})} \simeq \frac{E_{K-L}}{E_{J-K}} \simeq 0.38.$$

Where the DIRBE bands at 1.25, 2.2, 3.5, and $4.9 \mu\text{m}$ correspond to the standard J, K, L, and M photometric bands respectively. The slope found of ~ 0.38 agrees fairly

^aavailable at http://www.gsfc.nasa.gov/astro/cobe/cobe_home.html

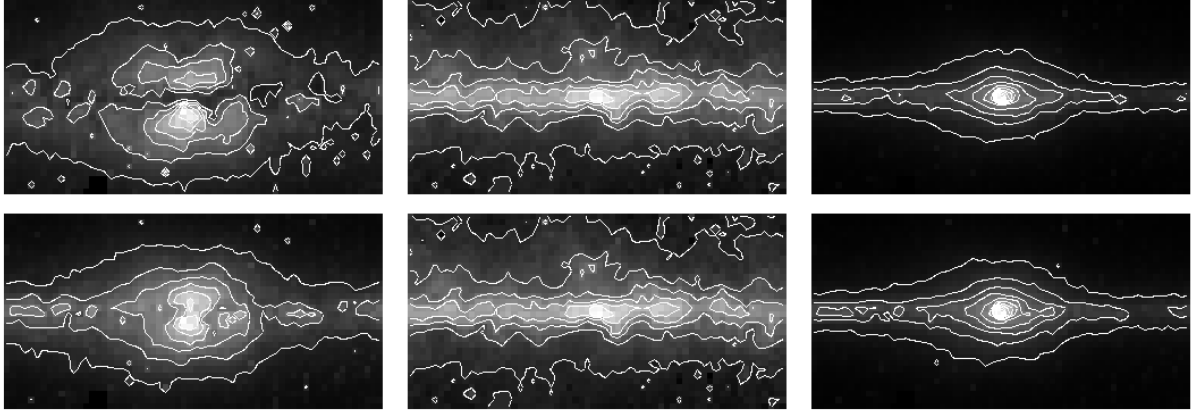


Figure 4.17: COBE-DIRBE NIR images for $|l| < 10^\circ$, and $|b| < 5^\circ$. *Top left*, original image in $1.25\mu m$. *Top middle*, optical depth $\tau_{1.25}$ map. which will be used to correct the original COBE-DIRBE image. *Top right*, Extinction-corrected galactic map in $1.25\mu m$. *Bottom*, Same as top row but for $2.2\mu m$ maps.

well with other extinction laws, such as those by Rieke & Lebofsky (1985) and consequently allows us to use other identities derived by those extinction laws. Thus we can calculate the optical depth as follows,

$$\tau_K = -2.5 \log \left(\frac{I_{1.25}}{I_{2.2}} \right) \times \left(\frac{0.38}{0.483 \ 1.086} \right)$$

Which combined with $I(\lambda) = I_0(\lambda) \exp(-\tau_\lambda)$ has been used to yield the extinction corrected maps at $1.25\mu m$ and $2.2\mu m$ as can be seen in figure 4.17. Figure 4.17 clearly shows the increasing effect of the extinction towards shorter wavelengths. The subsequent analysis of the COBE-DIRBE extinction corrected images has generally included just the $2.2\mu m$ once that consistency was shown between both bands and for simplicity's sake.

4.B DEPROJECTION BY MULTIPOLAR EXPANSION

Our first attempt to deproject the COBE map considered the use of a multipole expansion in exponential shells in order to obtain a reliable 3-dimensional density distribution. That is, our density can be fitted by

$$\rho(r, \theta, \phi) = \sum_n \rho_{lm}, \quad (4.27)$$

$$= \sum_n \sum_{l,m} C_{lmn} Y_{lm}(\theta, \phi) \exp \left(\frac{(r - r_n)^2}{2\sigma^2} \right). \quad (4.28)$$

P_{lm} are the associated Legendre functions; in addition the problem implicitly requires that $|r_n - r_{n-1}| < \sigma$ to reach smoothness in the solution. However, the available constraints in our case depend on the COBE image projected at 8 kpc in the square cone

towards the galactic center direction. Thus, each pixel is

$$\rho_{ij} = \sum_k C_k \rho_{kij} \quad (4.29)$$

Where we have expressed all the multipolar components at different radius with the single index k , and i and j are the pixel positions in the COBE image. In our case several number of multipolar shells were tried, ranging from 3 up to 10 radius for each lm combination. Similarly, multipole components were limited until the octupole term, choosing l and m to satisfy eight fold symmetry (l even and m even > 0). Hence, our multipolar shells correspond to 20-62 components (images from multipoles integrated 20 kpc along the line of sight) including a double exponential disk (Binney, Gerhard, & Spergel 1997) and a cuspy component (similar to Zhao's model) for the galactic center.

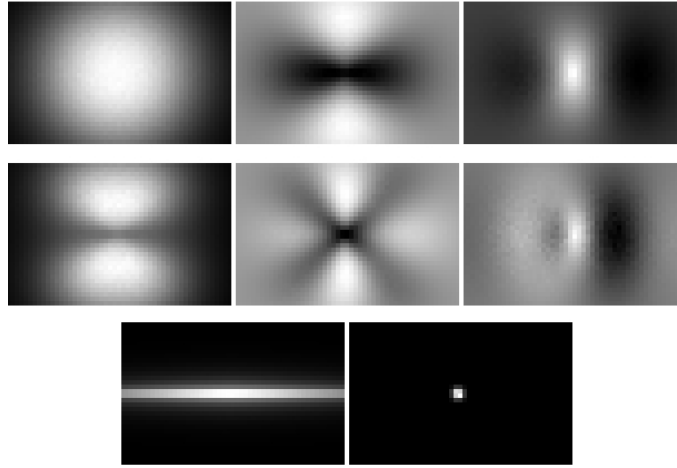


Figure 4.18: *Top and middle row*, multipole components for one of our shell radius, the multipole components have been integrated over the same cone covered by the COBE DIRBE image and considering the center of the galaxy (shells) at 8 kpc. *Bottom row*, double exponential disk and cuspy components projected at 8 kpc as well.

This problem, as equation 1 shows, requires that all $C_k > 0$, and therefore falls in the Non-Negative Least Square (NNLS) realm. NNLS problems are solvable for a number of standard programs currently available, such as E04NAF from the NAG library. However, even though no additional constraints are needed to solve the system, the best fit does not need to be a bar, not even a distribution increasing mass to the center. Thus, additional constraints are needed. Our first approach to obtain a realistic solution was to include a set of additional constraints projected from a 3-dimensional grid. Using a 3-dimensional density grid of $32 \times 32 \times 32$ for a detailed fit of the bulge structure, we require

$$\rho_{ij} = \sum_k C_k \rho_{kij} \geq 0. \quad (4.30)$$

The latter condition dramatically increases the number of constraints to 32768 making the NNLS process unsolvable. Nevertheless, taking advantage of the eight-fold symmetry assumed and placing the conditions in pixels as in a 3-D chess board or

some clever distribution, the constraints can be lowered to a solvable level. Despite the improvement achieved in the solutions adding the last constraints solutions produced still did not resemble a bulge-like structure. Results in adding to the fit a known 3-d density distribution showed that a significant amount of this false analytical target was required to obtain a reasonable solution from the deprojection making the process too biased to be considered reliable.

A second approach, simpler in its formulation implies including a set of constraints for the 3-dimensional density distribution which makes the density increase to the center, thus in addition to eq.4.30 we require for each pixel in the positions i,j

$$\frac{d}{dr}\rho_{ij} = \sum_k C_k \rho_{kij} \frac{(r_n - r)}{\sigma} \leq 0. \quad (4.31)$$

Unfortunately solutions including eq.4.31 in spite of their improved accuracy in the 2-D fits with respect to previous deprojections (fig.4.2), did not produce bars as we expected. This results argue against possible solutions lacking of additional information to the COBE DIRBE image. Consequently we developed deprojections by analytical bar distributions as explained in §4.3.1.

CHAPTER 5

Stellar proper motions in three off-axis galactic bulge fields

M.Soto, H.Zeballos, K.Kuijken, R. M. Rich, T. Astraatmadja
A&A (to be submitted)

This is the third in a series of papers which attempt to unveil the kinematic structure of the galactic bulge. We report here ~ 11000 new proper motions for three low foreground extinction off-axis fields, part of a sample which already includes 1000 radial velocities in the same three fields, and ~ 45000 proper motion and ~ 2000 radial velocities for three minor axis fields. Our project thus samples a considerable extent of the galactic bar.

Proper motions are derived from a combination of WFPC2 and ACS observations and reach accuracies better than 0.9 mas yr^{-1} .

The proper motion distributions in these fields are similar to those observed on the minor axis fields. Furthermore, we observe a rotation of main sequence stars below the turn-off across the galactic bulge, as it has been observed in minor axis fields. This gives us a clear indication of the extent of the galactic bulge in the first galactic quadrant.

5.1 INTRODUCTION

The mechanisms which have come to form the galactic bulge as we know it today are still uncertain. It is not clear whether the evolution of the bulge was driven by mergers, as the hierarchical galaxy formation scenarios suggest, or secularly from disk instabilities. To make progress, we need a clear observational picture of the bulge's current structure. But this is difficult because of the fierce extinction towards the galactic center, which has classically been the main obstacle to the acquisition of such a picture. Nevertheless, there has been much progress in the understanding of the galactic bulge over the past years.

In addition to the high foreground extinction by dust towards the galactic bulge, which is not constant even on small scales, bulge and disk are projected on top of each other on the sky. Disentangling them is not straightforward: even in the color-magnitude diagram (CMD) the populations overlap (Holtzman et al 1998). Moreover, blue stragglers extend brighter than the turn-off and overlap with the main sequence region hosting young population. This overlapping complicates the separation of populations based on photometry alone. Therefore, additional measurements are required in order to study the different components of the bulge.

Abundance studies as those by Rich (1988) or McWilliam & Rich (1994) have shown that the galactic bulge has a wide range of metallicities, which nevertheless differs from disk and halo populations, showing a comparatively metal-rich population. Consistently α elements have been found to be overabundant with respect to halo and disk (Zoccali et al. 2006; Fullbright 2007), suggesting a rapid formation scenario. α -elements are related to the formation timescale of the galactic bulge since they are preferably produced during the explosion of SN Type II (due to short lived massive stars), while iron production is favoured by SNe Type Ia explosion. SN Type Ia typically have a timescale 1 order of magnitude longer. Evidently most bulge stars were formed before the inter-stellar medium (ISM) could be enriched by SN Type Ia explosions, hence the short inferred formation timescale (< 1 Gyr) (e.g. Ballero et al. 2007). At the same time, number counts along the CMD between populous clusters at several latitudes have been used to estimate the foreground disk contamination (Feltzing & Gilmore 2000). Foreground disk population mimics the young bulge population, specially near the turn-off, affecting the age determinations in the bulge. These results for two bulge fields, which effectively identified the contamination by foreground populations, have placed the age of the bulge population as old as ~ 10 Gyr.

In spite its proximity, and due to the inconveniences described before, the galactic bulge has classically suffered of a lack of proper motions studies. Only in recent years, this situation has considerably improved. Spaenhauer et al. (1992) were the first to obtain reliable proper motions from a galactic bulge sample using photometric plates taken more than three decades apart. This study was the subject of a subsequent analysis by Zhao et al. (1994) which included radial velocities for a small subsample of stars (64). Zhao et al. (1994) found the presence of a significant vertex deviation in the small proper-motion combined sample.

Microlensing surveys of the Milky Way bulge have also contributed to create proper motions catalogs. The OGLE-II experiment has produced $\sim 5 \times 10^6$ proper mo-

tions (Sumi et al. 2004) for 49 bulge fields, covering a range of $-11^\circ < l < 11^\circ$ and $-6^\circ < b < 3^\circ$, and reaching accuracies of $0.8 - 3.5 \text{ mas yr}^{-1}$. The latter results have been the basis of a study of proper motion trends in the Red Clump of the bulge region (Rattenbury 2007a; 2007b). The Rattenbury et al. (2007a) selection, however, seems to have suffered from a significant disk contamination as pointed out by other authors (Vieira et al. 2007). Plaut's Window ($l, b = 0^\circ, -8^\circ$) has also recently provided proper motions (Vieira et al. 2007), which have been obtained with plate observations spanning 21 years of epoch difference. Bulge stars in these fields have been selected by cross-referencing with the 2MASS catalog in order to obtain a clean sample of bulge giants.

Space-based observations have also played a role in bulge proper motion observations, because of the combination of sharper images and much reduced blending. Anderson & King (2000, 2002) developed a precise technique to derive proper motions from HST images, which they applied to globular clusters as Tucanae 47 (Anderson & King 2003). Kuijken & Rich (2002) (the first paper on this project; henceforth KR02) were the first to use HST observations to obtain reliable bulge proper motions. Two low foreground extinction fields at that time, Baade's Window ($l, b = 1.1^\circ, -3.8^\circ$) and Sagittarius I ($l, b = 1.3^\circ, -2.7^\circ$) were used to successfully obtain 15,862 and 20,234 proper motions respectively. The latter results showed the feasibility of space-based proper motions using time baselines considerably smaller than those previously used. The samples in both fields could be separated in bulge and disk components based on the mean proper motions. The bulge component clearly resembled an old population, as those observed in globular clusters, and showed a significant rotation with no covariance in l, b . For both fields the results of new further proper motion studies based on HST images have appeared since then (Kozłowski et al. 2006). The latter study obtained proper motions for 35 small fields in the vicinity of Baade's Window. Their calculations, which involved the combination of ACS HRC images and archival observations with WFPC2, yielded 15,863 stellar proper motions. These proper motions, which showed consistency with the velocity dispersions found by KR02, found in addition a significant negative covariance term in the transverse velocity $C_{lb} = \sigma_{lb}/(\sigma_l\sigma_b) \simeq -0.10$, which might imply a tilt in the velocity ellipsoid with respect to the galactic plane.

New results for the *Sagittarius I* field (Clarkson et al. 2008) yielded > 180000 proper motion with epochs just 2 years apart. From their initial numbers they finally selected 15,323 bulge stars using a similar procedure as the one applied by KR02. The covariance found by Kozłowski et al. (2006) was also found. In addition Clarkson et al. (2008) produced velocity ellipsoids in (l, b) as a function of distance bins. These velocity ellipsoids demonstrated a slight dependence on the distance of the objects analyzed. Finally, and similarly to the finding of KR02, the median stellar sequence for this bulge sample was best represented by an 11 Gyr old isochrone.

We report here on the next step in our own project: to measure proper motions and radial velocities in several low foreground extinction windows of the galactic bulge. This chapter presents proper motions for three new fields at positive longitudes in the near end of the galactic bar. Suitable first epoch WFPC2 images were taken from the HST archive, and complemented with new ACS/WFC exposures. The resulting time

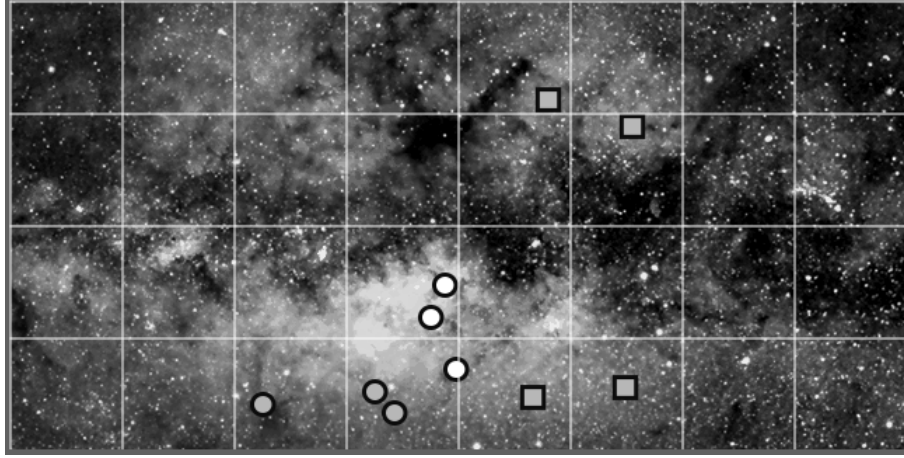


Figure 5.1: Fields in the Galactic Bulge observed for this project, superimposed on an optical map, from longitude $+20^\circ$ to -20° , and latitude -10° to $+10^\circ$. White circles are the fields on the galactic minor axis, for which proper motions have been published in KR02 and K04. Grey circles are the fields for which we here present new proper motions. Grey squares are the fields in the far end of the bar with incomplete observations.

baselines are 8-9 years.

This paper is organized as follows: In section 2 we describe our observations. A detailed account of the procedures involved in the measurements of the proper motion can be found in §3. Section 4 presents the analysis performed on our sample of proper motions, the criteria used to separate a “pure bulge” population, and the implications of the results. In addition, we compare our results with those of similar surveys in the galactic bulge. Finally, we have summarized our conclusions in §5.

5.2 OBSERVATIONS

Our observations target three fields at positive galactic longitudes; Field 4-7 $[(l, b) = (3.58^\circ, -7.17^\circ)]$, Field 3-8 $[(l, b) = (2.91^\circ, -7.96^\circ)]$, and Field 10-8 $[(l, b) = (9.86^\circ, -7.61^\circ)]$. These fields are the farthest from the galactic minor axis with accurate proper motions.

Table 5.1: Summary of observations

Field	Epoch	Exp.(s)	Instrument	Type	α, δ ($J2000$)
Field 4-7	1995 July 14	1200($\times 2$), 1300($\times 2$)	WFPC2	Undithered	18 22 16, -29 19 22
	2004 July 11	50($\times 2$), 347($\times 4$)	ACS WFC	Dithered	
Field 3-8	1996 May 1	500, 2900($\times 3$)	WFPC2	Undithered	18 24 09, -30 16 12
	2004 July 12	50($\times 2$), 348($\times 4$)	ACS WFC	Dithered	
Field 10-8	1995 Nov 30	1200($\times 4$)	WFPC2	Undithered	18 36 35, -23 57 01
	2004 July 14	50($\times 2$), 347($\times 4$)	ACS WFC	Dithered	

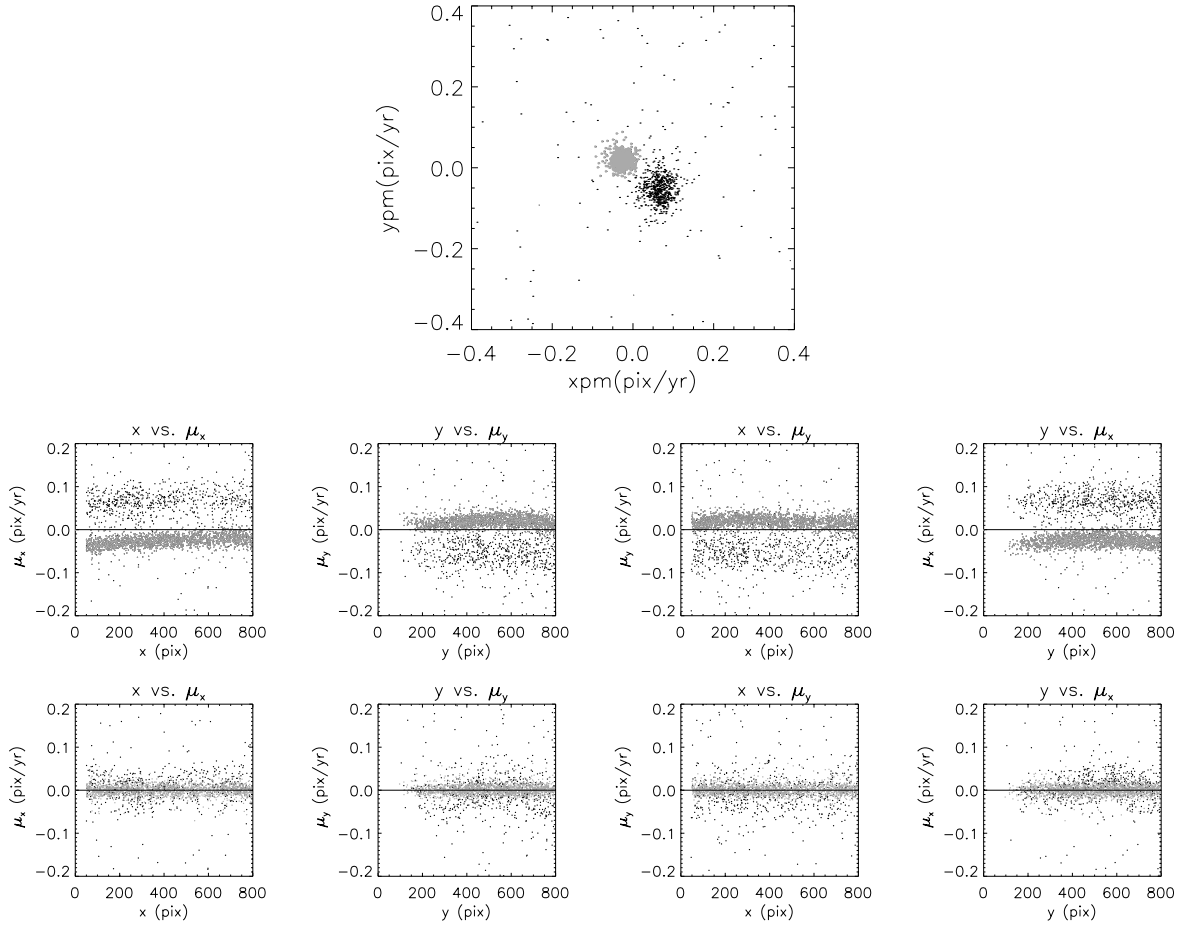


Figure 5.2: Proper motions before and after the correction in WF4 for Field 10-8. Cluster stars have all a single velocity, which therefore biases the relative zeropoint when calculating the proper motion of bulge stars. The latter stars must thus be excluded from the reference frame used to calculate bulge proper motions. *Top row*, proper motions in $pixels\ yr^{-1}$ before the correction for WF4 chip in Field 10-8, where black dots are bulge stars, and grey dots are those classified as cluster stars. *Second row*, proper motions in pixels μ_x and μ_y as a function of the $x - y$ coordinates before the correction. *Third row*, same as second row, but after applying the correction.

First epoch observations were obtained from the Hubble Space Telescope (HST) data archive, which is now almost a decade and a half old. This wealth of images has provided us in addition with the three low foreground extinction fields close to the galactic minor axis, already presented in KR02 and K04. Two aspects of the 1st epoch data are not ideal: (i) the exposures are all long, so that we cannot measure positions for the bright stars; (ii) the exposures are not dithered, which limits our ability to build a point-spread function (PSF) model. In order to attenuate the effect of the undersampling of the PSF we chose the F814W filter, which has the widest and therefore least undersampled PSF.

As it was already mentioned, the observations for our three fields have combined

WFPC2 and ACS WFC for first and second epoch respectively. The ACS WFC second epoch observations acquired during 2004 took place between 2004 July 12 and 14. Two short exposures with 50 s of integration time and 4 of ~ 350 s were taken of each field; second epoch observations were dithered in order to maximize accuracy and ensure that errors in the proper motion were not dominated by the second set of exposures. Table 5.1 summarizes our observation in both epochs for our three fields.

It has been proven that for a wide range of realistic PSF profiles the 1σ uncertainty in the centroid of a stellar images of full width at half maximum $FWHM$ and signal to noise ratio S/N is given by $\simeq 0.7 \times FWHM/(S/N)$ (KR02). In the case of our proper motions, where first epoch observations were performed in WFPC2 ($FWHM \simeq 0.12''$ in F814W), a star detected at 20σ can be centered with a precision of $4.2 mas$. Therefore, a time baseline of 8 yr (in our fields we have 8-9 yrs of baseline), yields an accuracy of $0.6 mas yr^{-1}$, which corresponds to $23 km s^{-1}$ at the distance of the bulge of about 8 kpc. On the other hand, our second epoch observations, which have been dithered, and have a higher resolution, and even though they provide a higher accuracy than those of the first epoch, can not improve our proper motion precision beyond the limits of the first epoch observations, which in addition are undithered. Thus, the spatial variations of the PSF within the ACS WF image (Anderson & King 2006) have not been considered in our analysis. These PSF spatial variations in ACS if ignored, can produce 10% of error in core photometry, which is reduced when a larger aperture is taken. In the case of astrometric measurements the effects are at the 0.01 pixel level ($\simeq 0.001''$ for ACS) which is negligible considering the error introduced by the first epoch. New measurements including only ACS measurements will include this effect in our astrometric measurements in the future.

5.3 PROPER MOTION MEASUREMENTS

Anderson & King (2000) have described a procedure for accurate astrometric measurements using HST WFPC2, and subsequently updated these for ACS WFC (Anderson & King 2006). Originally, these techniques have been designed to work with both epochs dithered, where a common PSF model is used for all the dithered exposures. This PSF must be consistent with all the exposures and is used to obtain the centroids of each star. Thus, for our undithered first epoch observations we have performed some variations to the original (Anderson & King 2003) recipe. In order to improve the centroid determination our method determines a PSF by each exposure starting from an analytical model. This model consists of a Gaussian PSF multiplied by a polynomial, where the number of the components for the polynomial accounts for the wings of the PSF and other secondary features. In each exposure the PSF model starts from this model being fitted to the 100 brightest unsaturated stars in the image, the process then iterates using a higher order polynomial with an robust outlier criterion which refines the selection until it converges. Details of the technique can be found in KR02, and will not be repeated here.

Once the PSF has been calculated for each exposure we can determine the proper motions. These are obtained starting from a master image which has been generated by

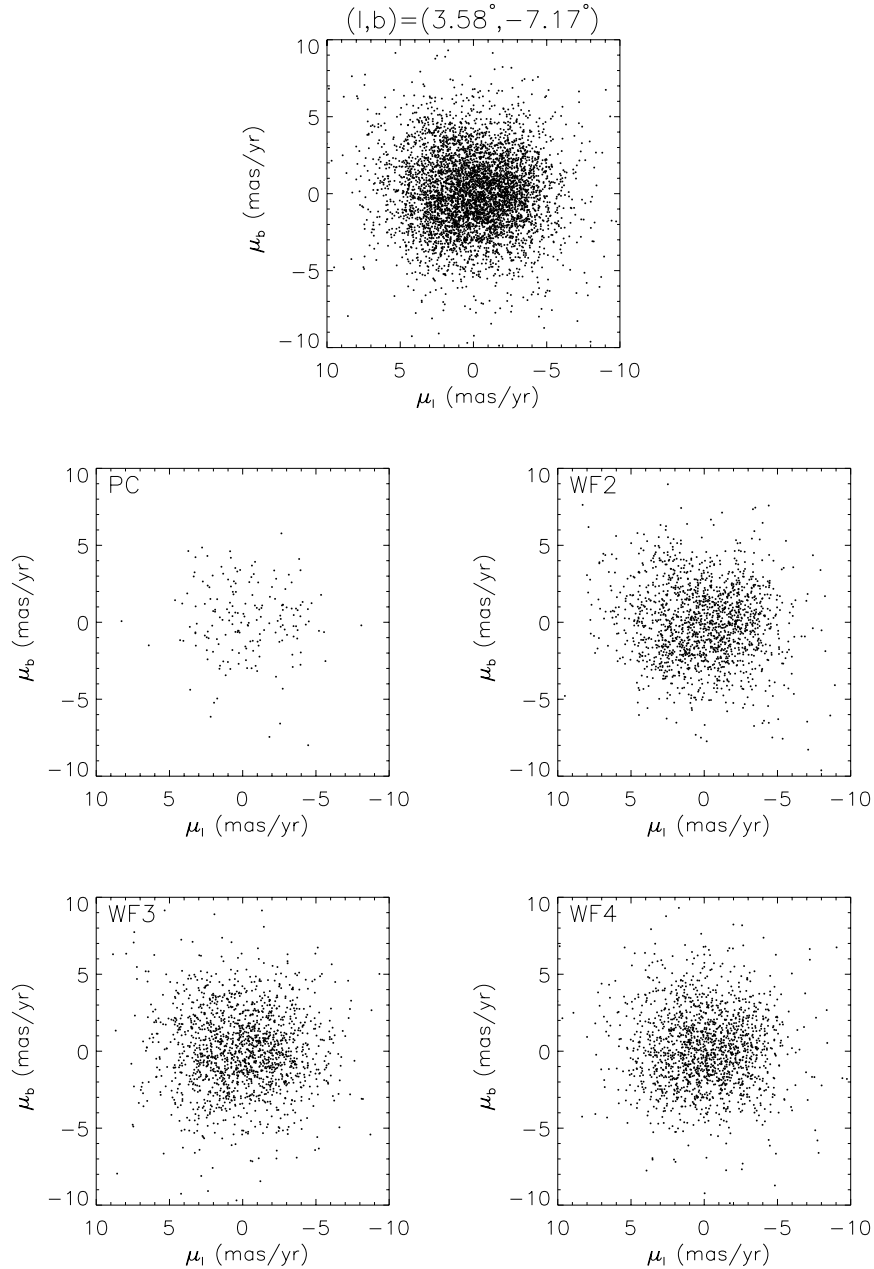


Figure 5.3: *Top row*, proper motion distribution for WFPC2 in Field 4-7. *Second and third row*, proper motion distribution on individual CCD frames of WFPC2.

combining all the first epoch exposures in F814W filter. Then the master image is used in DAOFIND to detect stars with fluxes over 15σ , which produce a master list of stars. The master list is used to detect the same stars in all the exposures; for each exposure the master coordinates are used as initial guess to the star position. In the case of proper motion with WFPC2 in all the epochs a simple linear transformation is sufficient to transform the master coordinates to each exposure (e.g. KR02). For our second epoch ACS WFC images, we have used a third order polynomial transformation to account

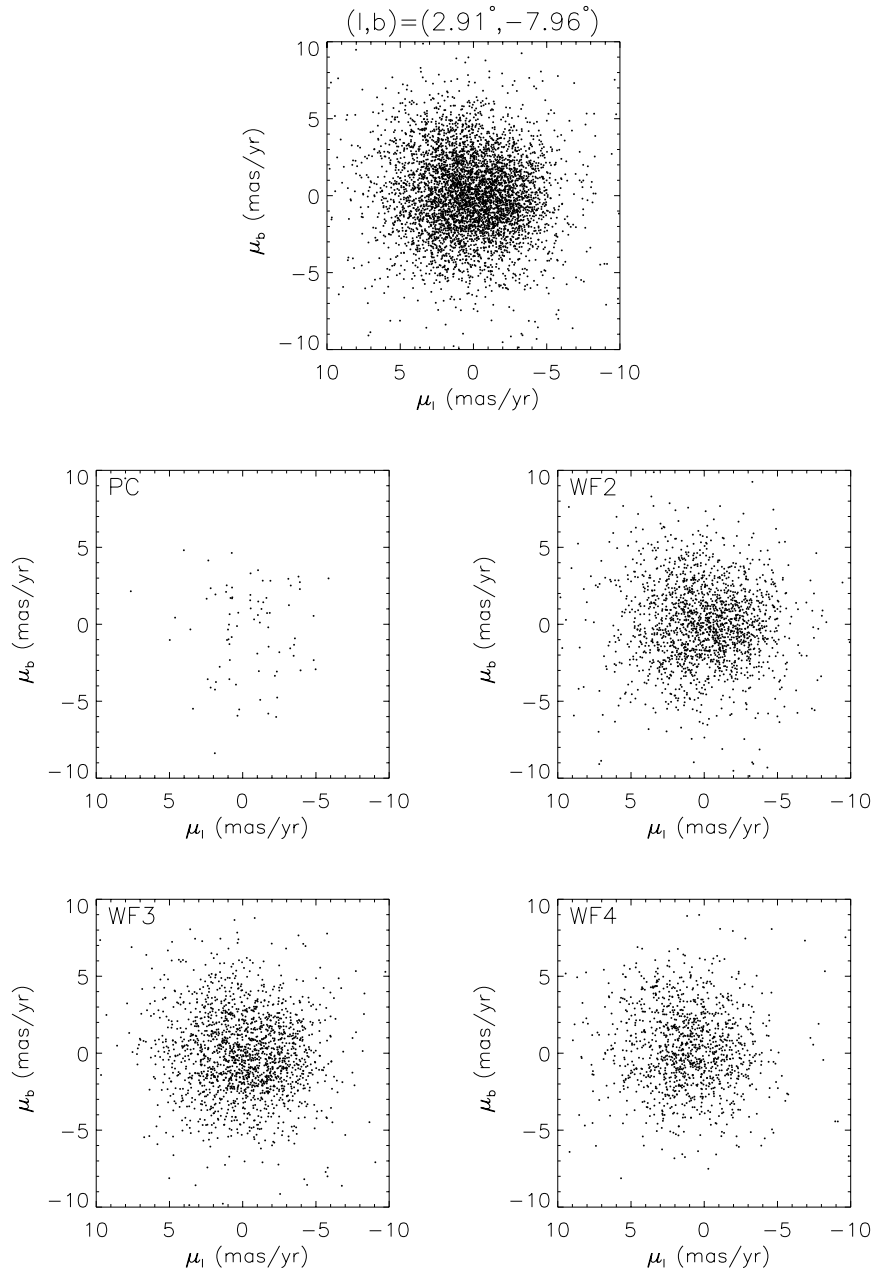


Figure 5.4: Same as Fig. 5.3, but for the Field 3-8

for the geometric distortions found in ACS. For each star a PSF fit is then computed, to give a best fitting position in each exposure.

With the positions calculated for each exposure we can then extract the proper motions. The proper motions must be separated from the rest of the effects included within these positions. These include a general transformation that maps the positions of each exposure to those of the reference frame, the proper motions, the average position residual as a function of pixel phase for each image which is subtracted from each measurement, and average residual position as a function of the “34th row” effect

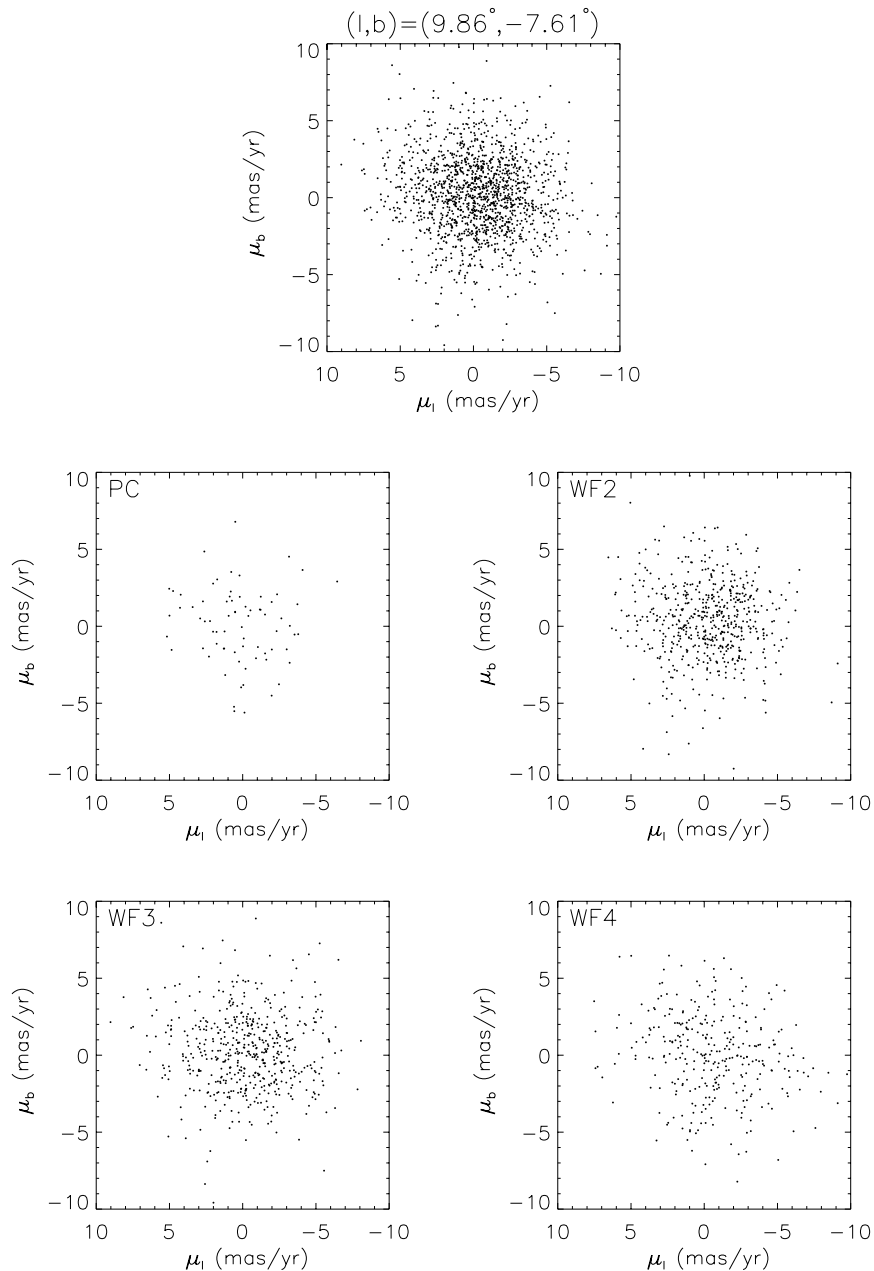


Figure 5.5: Same as Fig. 5.3, but for the Field 10-8

(Anderson & King 1999). This process is iterative, it produces a proper motion solution in each loop for each star. The solution is obtained from a weighted linear least-square fit with rejection of outliers, where the weights are estimated from the flux detected.

We must stress that these are *relative* proper motions, they assume that the average movement of all the stars in the field is zero. Absolute proper motions would require a selection of extragalactic sources as a reference in the same field. The zero-mean assumption works well for bulge fields, but breaks down when many stars have the same peculiar velocity. Such is the case of the Field 10-8, where many of the bright stars

Table 5.2: Proper Motion Dispersions

Field	Chip	N	σ_l ($mas\ yr^{-1}$)	σ_b ($mas\ yr^{-1}$)	σ_{lb} ($mas^2\ yr^{-2}$)	r_{lb}
Field 4-7	PC	180	3.00±0.29	2.85±0.29	0.81±1.08	0.08±0.16
	WF2	1617	3.00±0.08	2.66±0.08	0.53±0.44	0.04±0.04
	WF3	1641	3.21±0.10	2.90±0.11	0.99±0.28	0.11±0.05
	WF4	1678	3.00±0.06	2.80±0.07	0.52±0.46	0.03±0.03
	All	5116	3.07±0.04	2.79±0.04	0.72±0.10	0.06±0.03
Field 3-8	PC	83	3.33±0.45	3.53±0.32	0.39±1.25	0.01±0.18
	WF2	1802	3.13±0.09	2.98±0.08	0.76±0.38	0.06±0.04
	WF3	1806	3.17±0.11	2.99±0.07	0.71±0.33	0.05±0.04
	WF4	1231	3.08±0.09	2.87±0.08	-0.11±0.57	-0.01±0.03
	All	4922	3.18±0.03	2.97±0.04	0.69±0.12	0.05±0.02
Field 10-8	PC	75	2.54±0.20	3.43±0.63	0.89±0.97	0.09±0.14
	WF2	570	2.87±0.14	2.79±0.16	-0.58±0.62	-0.04±0.07
	WF3	531	3.24±0.16	2.71±0.14	1.01±0.33	0.12±0.06
	WF4	328	3.57±0.20	3.15±0.19	1.30±0.30	0.15±0.08
	All	1504	3.16±0.12	2.88±0.11	0.82±0.28	0.07±0.04

Note: r_{lb} is the Pearson correlation coefficient.

in the master list correspond to the globular cluster NGC 6656 (M22). To make matters worse the mean proper motion is different for the four chips of WFPC2 since the cluster star fraction depends on position. In order to remove this effect we have discarded the cluster stars in each image from the master list. We have done this selection by means of the proper motions calculated including all the stars in the field, the cluster stars can thus be easily identified (and removed) taking advantage of its small dispersion. Once identified, the proper motions have been re-calculated including only non-cluster stars, in which is reasonable use the assumption of average movement zero. This procedure is illustrated in figure 5.2 for one of the chips, WF4. In a similar way, we repeated the latter procedure for cluster stars in order to exclude bulge contamination, as it is shown in §5.4.1.

5.4 ANALYSIS

Our proper motion results can be observed in figures 5.3, 5.4, and 5.5; proper motion dispersions and numbers per field are shown in table 5.2. Color-magnitude diagrams for the three fields which include the proper motion information also appear in figures 5.6, 5.7, and 5.8. The first indication of the correct performance of our method appears in Table 5.2, which does not show any evidence of a significant variation or inconsistency of the kinematics between the WF and PC chips, as it would be expected in a reliable proper motion determination. Similarly, we find that the distributions of the

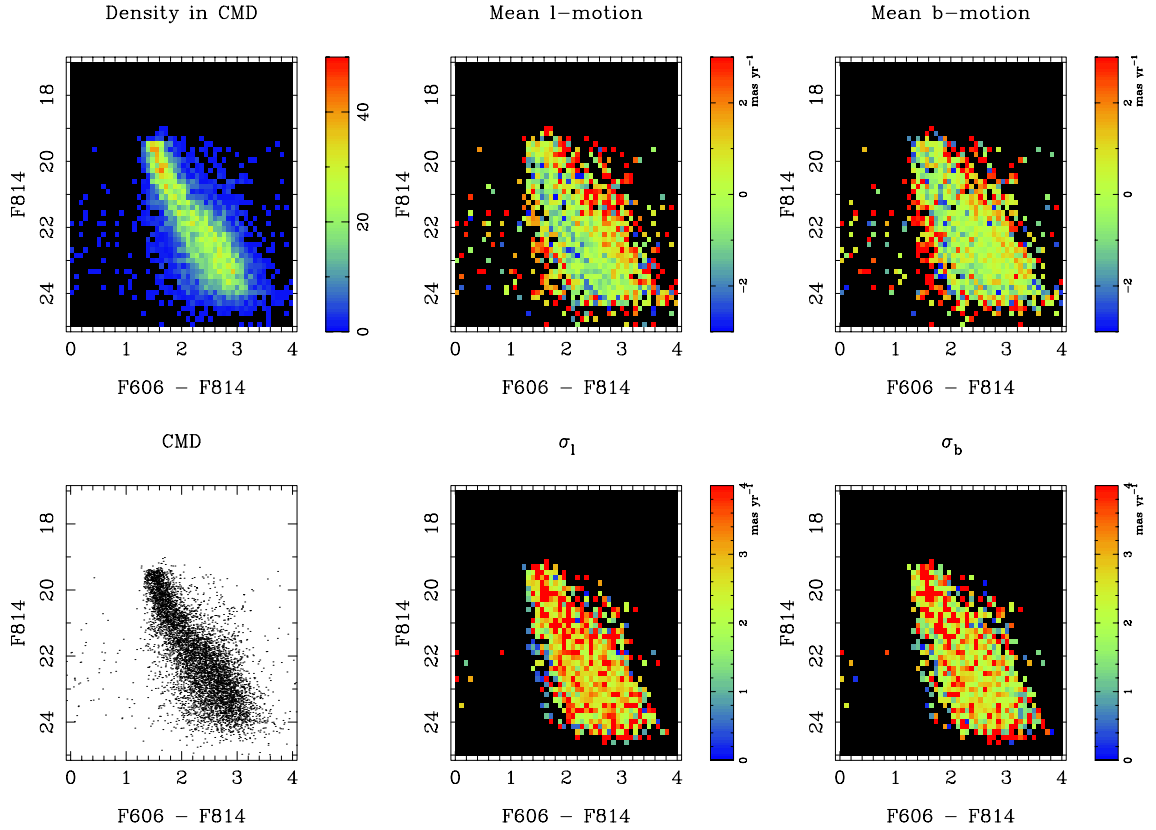


Figure 5.6: Binned CMDs of Field 4-7 field $(l, b) = (3.58^\circ, -7.17^\circ)$ with $n_{\text{fit}} > 5$. The parameter n_{fit} corresponds to the minimum number of exposures fitted by the proper motion solution of each star. Some plots have been color-coded using the proper motions and derived dispersions. *Top row, left to right:* Stellar density; mean longitudinal proper motion; mean latitudinal proper motions. *Bottom, left to right:* Unbinned CMD; longitudinal dispersion in proper motions; latitudinal dispersion in proper motions.

proper motion do not differ dramatically from one field to the other, this agreement in the proper-motion distribution seems to extend even to the fields presented in KR02 and Kuijken (2004; henceforth K04) close to the galactic minor axis. Our three fields at positive longitudes seem to have a spherical distribution with no significant correlation between l and b proper-motions, at the same time σ_l and σ_b are slightly bigger than the dispersions found in minor axis fields in KR02 and K04. At first inspection we can infer two reasons to this increase in the dispersions; due to an intrinsic increase accordingly to the location of the fields, and also due to the higher contamination by foreground disk populations, and therefore a decrease of the total number of bulge stars detected. We will try to discern below which of these effects prevail using the assistance of the CMD information.

The binned CMDs for the three fields show some distinctive features. All the fields are affected by saturation of the bright stars in the first epoch data, which has limited our proper motions to main sequence (MS) stars below the turn-off. Fields in KR02, on the other hand, counted with many shorter exposures which allowed them to reach the turn-off and red-giant branch (RGB). A second clear feature present in the three

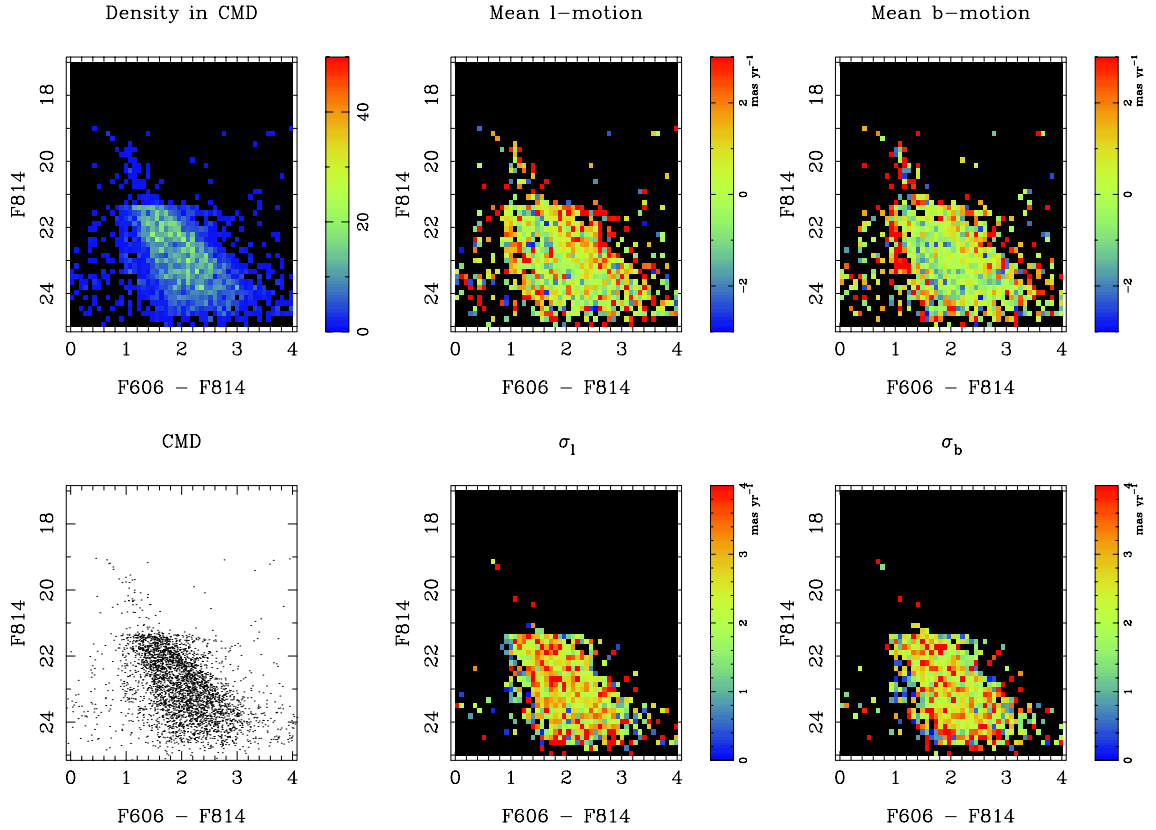


Figure 5.7: Binned CMDs of Field 3-8 field $(l, b) = (2.91^\circ, -7.96^\circ)$ with $n_{\text{fit}} > 6$

fields, and in spite the difference in numbers, is a gradient perpendicular to the main sequence in the mean μ_l . This gradient, which for a given color shows a drift toward negative μ_l , has been already observed in the central fields in KR02; in our fields however has a noisier appearance which we believe is due to the reduced statistics. The gradient can be explained as a signature of the rotation through the galaxy, as figure 5.9 shows for one of the fields, where high positive μ_l should correspond mainly to foreground population rotating in front of the bulge. Interestingly, a similar but noisier feature appears in the mean μ_b panels, this might be caused rather by a combination of projection effect of the bulge orbits and contamination by the disk which we would be able to discern only when we apply our Schwarzschild model to these fields. As it has been mentioned in previous studies, normally the rotation of the galactic bulge is difficult to observe because of the strong contamination by disk and halo and the rapid decrease in numbers of the bulge population as one moves off axis.

Proper motion dispersions deliver a different piece of information. Field 3-8 shows a rather noisy distribution of dispersion over the main sequence. Field 4-7 and Field 10-8 dispersions on the other hand, show that the fainter main sequence stars have comparatively a smaller dispersion than bright main sequence stars. This can be interpreted as the distance effect that we would expect for fainter stars lying farther away and that therefore show smaller proper motion (it is also a nice demonstration that noise does not dominate our results).

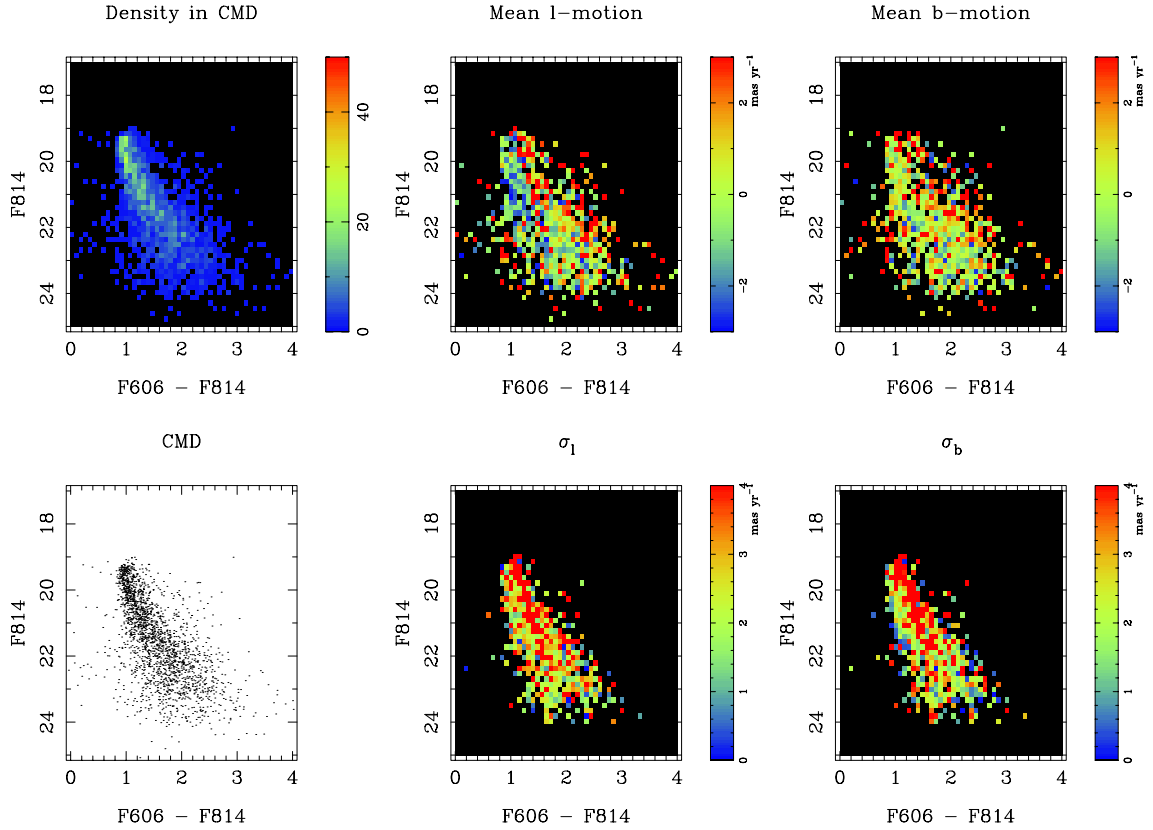


Figure 5.8: Binned CMDs of Field 10-8 field (l, b) = $(9.86^\circ, -7.61^\circ)$ with $n_{\text{fit}} > 5$

Consistently with the analysis of KR02 and K04 we followed a similar procedure to dissect the stellar populations in our fields. We have chosen a crude distance modulus as an indicator of the distances toward the galactic bulge, the quantity M^* , which can be defined as:

$$M^* = m_{814W} - 3 \times (m_{814W} - m_{606W}) \quad (5.1)$$

has been used to remove the slope of the main sequence stars in the CMD for our proper motion sample. The factor 3 multiplying the color, is 2 in KR02, due to the difference in filters with the minor axis fields Sagittarius-I, and Baade's Window (both used F814W and F555W filters).

Figure 5.10 illustrates our distance modulus M^* and its respective photometric distance D^* as a function of the color for Field 4-7. In order to obtain completeness from the initial main sequence subsample, which is based on the selection performed in K04 for field near NGC 6558, we have re-selected a narrower band in the photometric distance D^* . An analysis to the angle ϕ_{lb} (the equivalent to the vertex angle, but in the l - b velocity plane) in distance bins shows a mild increase of this angle as a function of distance D^* . The angle ϕ_{lb} has been calculated using an iterative clipping algorithm which rejects stars beyond 3σ of the distribution, in order to avoid contamination. In addition, we calculated the Spearman correlation coefficient r_S in each case to have another independent measurement of the correlation between μ_l and μ_b . Errors in ϕ_{lb}

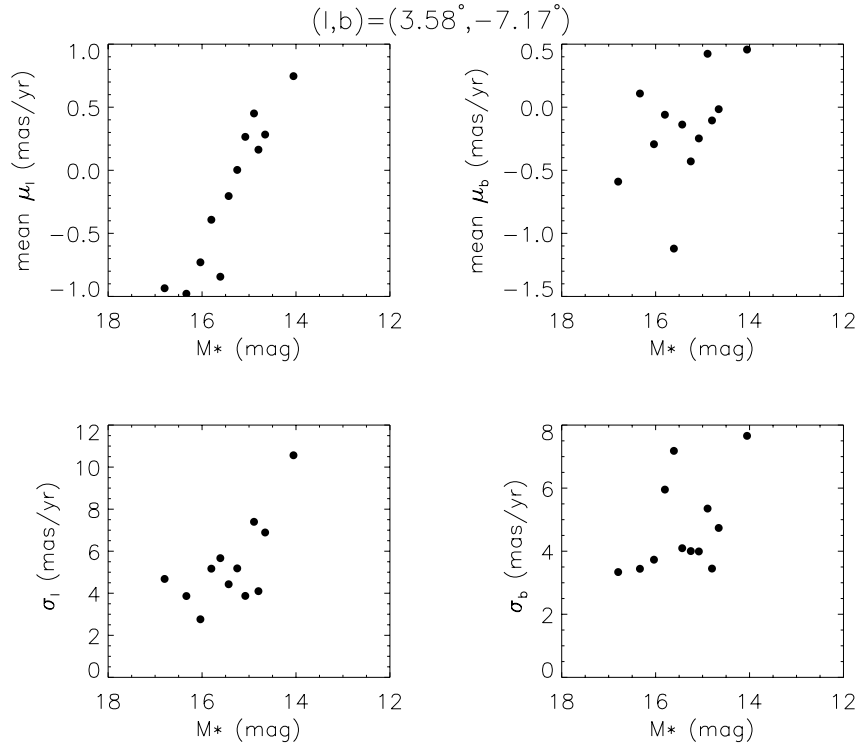


Figure 5.9: Mean proper motions and dispersions as a function of the photometric parallax M_* , for the subsample of main sequence stars in Field 4-7. Each point corresponds to 180 stars.

come from Bootstrap Montecarlo realizations, where figure 5.11 shows the respective velocity ellipsoids for Field 4-7. Error bars in ϕ_{lb} and significance of r_S do not indicate a reliable significant correlation between l and b for these bins, a result that has been repeated for Field 3-8 and Field 10-8. Similarly, Clarkson et al. (2008) also looked for significant changes in the orientation of the velocity ellipsoid generated by proper motions, their improved sample of ACS proper motions in Sagittarius-I showed no such transition.

5.4.1 NGC 6656 results

We have already mentioned how our field with the highest latitude Field 10-8, has been separated in a cluster and bulge component during the proper motion procedure using a pure kinematic selection. Table 5.3 and figure 5.12 show the numbers and dispersions for the cluster stars lying in the field. In a globular cluster such as NGC 6656, the velocity dispersion observed must be very small in order to maintain a dynamically stable structure. This kind of behaviour can be clearly observed in the figure 5.13, where no particular gradient or variation is revealed in the respective binned CMD. The radial velocity dispersion for cluster stars in this field in chapter 2 is $\sim 17 \text{ km s}^{-1}$, which is very close to the intrinsic error of the radial velocity measurements. Similarly, we would expect that most of the proper motion dispersion observed in this system is

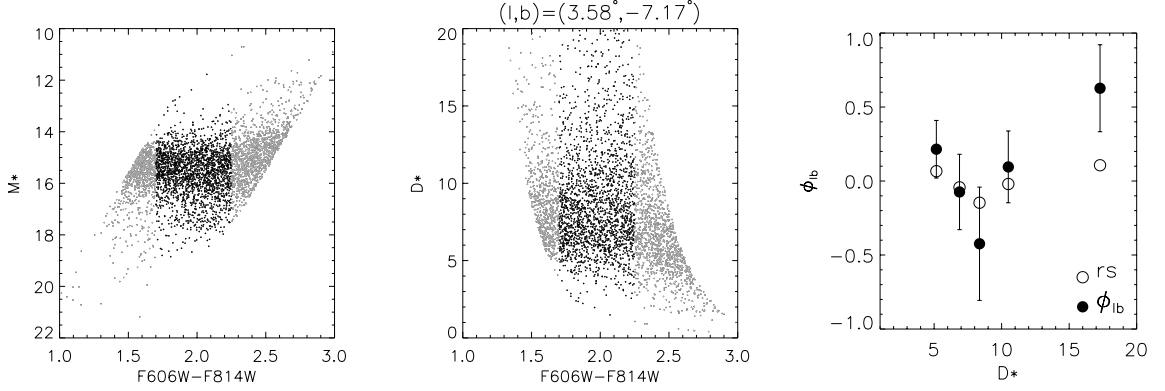


Figure 5.10: *Left*, Photometric parallax M^* as a function of the color in Field 4-7. *Middle*, Distance D^* in kpc as a function of the color. *Right*, Angle ϕ_{lb} as a function of binned D^* , equal numbers of stars have been selected per bin; in addition the Spearman correlation coefficient r_S has been calculated in each bin to have an independent correlation measurement between l and b .

due to systematic errors in the procedure. Consequently, we can test the accuracy of our proper motions by measuring this observed cluster dispersion.

Table 5.3 indicates a dispersion in l and b of $\sim 1.1 \text{ mas}$ at the WF chips, which at the distance of 3.2 kpc (Samus et al. 1995) from the Sun corresponds to $\sim 17 \text{ km/sec}$. Not surprisingly, the PC dispersions are about twice as small, which we relate with a direct effect of pixel size in the measurements. These dispersions are a confirmation of the quality of our measurements, and perfectly satisfies the precision achieved by our radial velocities in the same field (see chapter 2 for details) of 30 km/sec . Furthermore, when performing a two-dimensional Gaussian fit over the proper motion data the dispersion drops in the l and b directions to $\sim 0.9 \text{ mas}$, which corresponds to $\sim 14 \text{ km/sec}$. All this confirms the reliability of our proper motion technique.

Table 5.3: Proper motion dispersions in NGC 6656

NGC 6656					
Field	N	σ_l (mas yr^{-1})	σ_b (mas yr^{-1})	σ_{lb} ($\text{mas}^2 \text{ yr}^{-2}$)	r_{lb}
PC	207	0.55 ± 0.02	0.57 ± 0.06	0.04 ± 0.12	0.01 ± 0.06
WF2	721	1.02 ± 0.04	0.99 ± 0.03	0.19 ± 0.16	0.04 ± 0.05
WF3	1141	1.17 ± 0.03	1.14 ± 0.03	0.25 ± 0.17	0.05 ± 0.04
WF4	857	1.16 ± 0.05	1.21 ± 0.04	-0.27 ± 0.19	-0.05 ± 0.05
All	2899	1.10 ± 0.02	1.10 ± 0.02	0.12 ± 0.16	0.01 ± 0.02

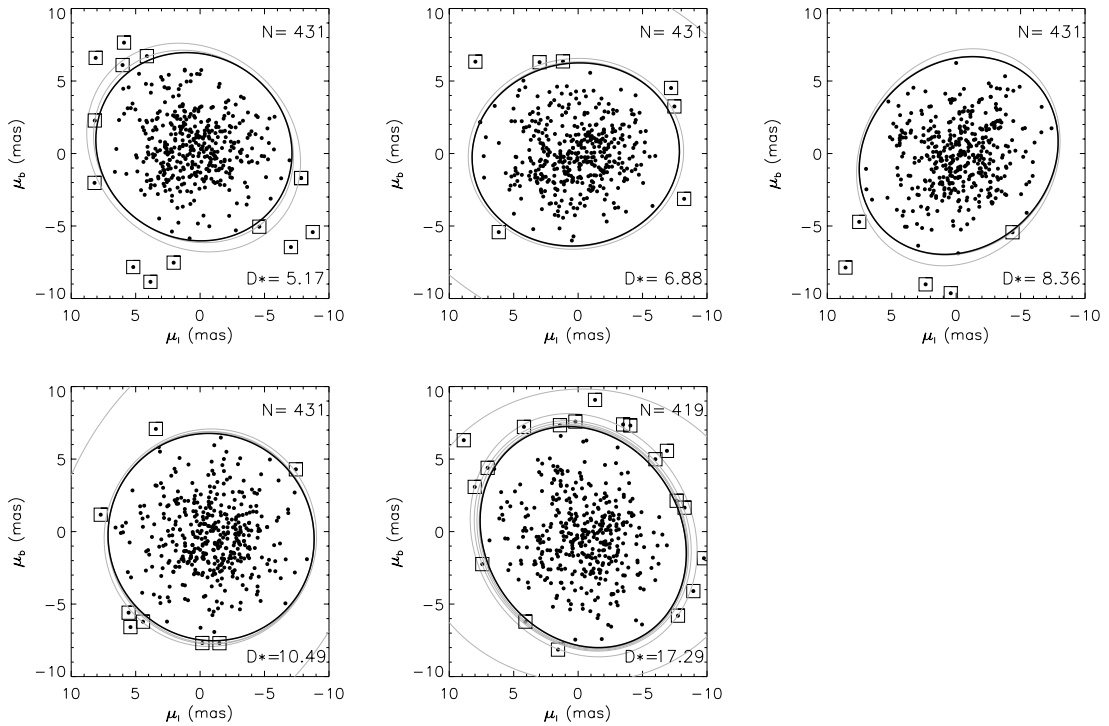


Figure 5.11: Velocity ellipsoids used to calculate the angle ϕ_{lb} in Field 4-7. An iterative clipping algorithm has been used to exclude stars beyond 3σ . Rejected stars during the process are enclosed by squares.

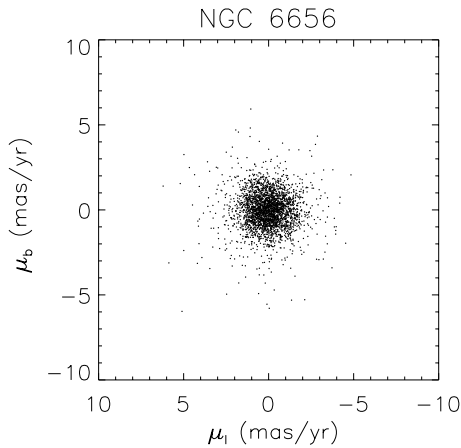


Figure 5.12: Proper motion distribution for stars belonging to the globular cluster NGC 6656 observed in Field 10-8. These stars have been kinematically separated of the bulge population during the proper motion procedure.

5.4.2 A bulge sample kinematically selected

Extracting a pure bulge population from the total sample including disk stars is difficult. The uncertain binary fraction in the bulge and overlapping of populations in

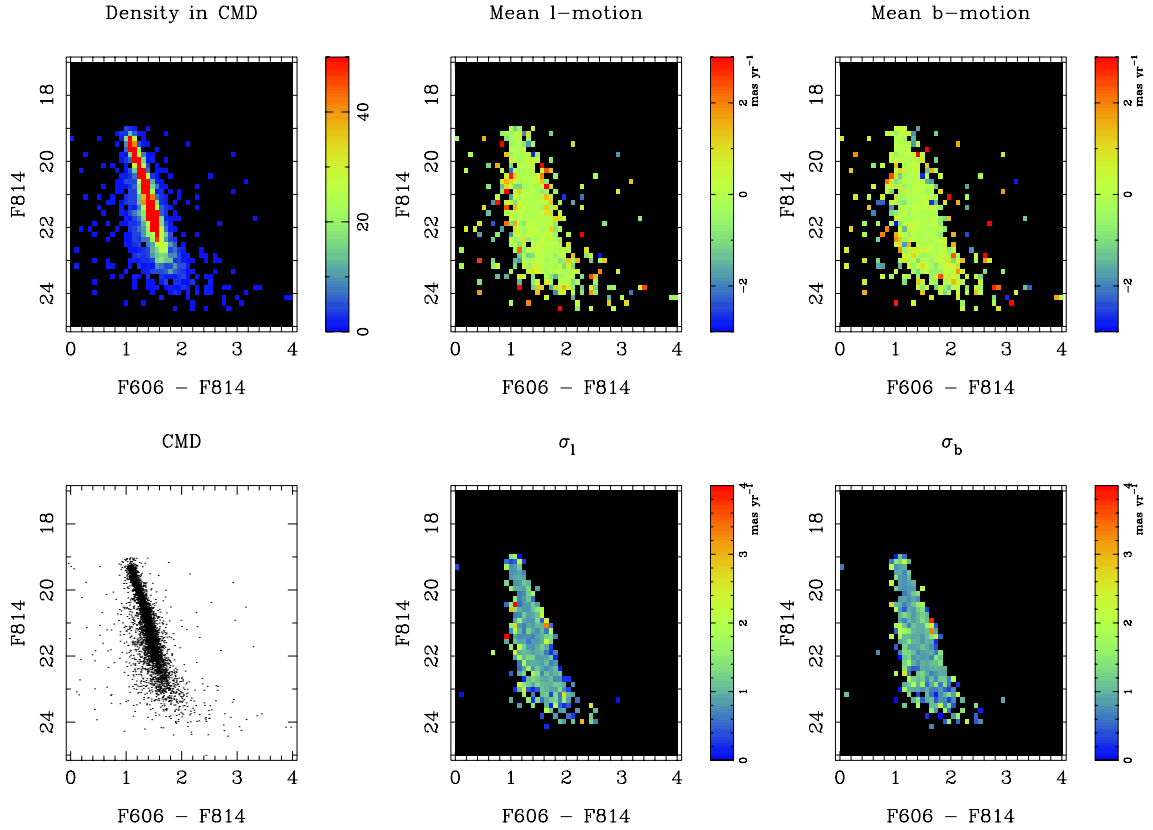


Figure 5.13: Binned CMDs for NGC 6656 stars in Field 10-8 $(l, b) = (2.91^\circ, -7.96^\circ)$. The stars have been selected kinematically using the small kinematic dispersion of the cluster proper motions.

the CMD are some of the reasons (KR02). In order to overcome such difficulties, and also considering the strong evidence of a rotation gradient through the bulge, which resembles the kinematics of minor-axis fields, we turn to the kinematics as our selection criterion. KR02, and more recently Clarkson et al. (2008), have successfully used simple cutoffs in μ_l and μ_b to select bulge star for minor-axis fields; a pure bulge pop-

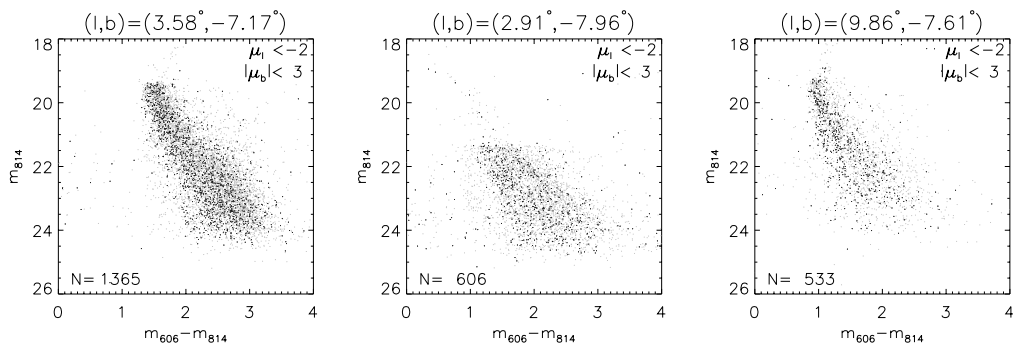


Figure 5.14: CMDs for subsample of kinematically selected stars in each field in our survey. Grey faded points correspond to non-selected stars .

ulation can be obtained by selecting stars with negative μ_l and moderate $|\mu_b|$. This cut, probably excludes some bulge stars on the near side, biasing the subsample to far-side objects. On the other hand, a considerable disk contamination from the far side is unlikely due to the line of sight of our fields.

Figure 5.14 shows the result of the selection in our fields; where the absence of features in the CMD, as the RGB, and the diminished statistics for our three off-axis fields have made difficult to consider them univocally as an old population, as it happens in the minor axis fields. We are not able to check if the cuts are effective in removing the main sequence, and late type foreground populations, without the aid of additional information as proper motions. However, considering the resemblance of the proper motion results in the off-axis fields with those of the fields along the galactic minor axis, we believe the same selection criterion for a pure bulge population should be effective in the off-axis fields, where the absence of other populations in the CMDs is mainly a technical difficulty rather than an intrinsic lack of features. This might be solved in the future with shallower additional observations reaching the turn-off and RGB regions. At the same time blue stragglers can not be detected due to the same saturation problem.

Hence, we distinguish the two populations that coexist in each CMD. Interestingly, the fact that this kinematic separation between the two populations (bulge and disk) still occurs at the longitude of our fields gives us a clue about the real extent of the bar. In the future, models as the one that we developed using the Schwarzschild technique (see chapter 4) will include the kinematic information here exposed to disentangle the actual bulge structure, and produce an improvement in the bar/bulge parameters generated by our model only with the initial three minor axis-fields.

5.5 CONCLUSIONS

We have presented in this chapter ~ 11000 new proper motions for 3 off-axis fields of the galactic bulge. The results for these three fields show a remarkable agreement with the results in KR02 and K04, and thus speak of a bulge where the kinematics observed in the center, along the galactic minor axis fields, is repeated to some extent to higher longitudes. We have checked that the rotation of the bulge, in spite of the reduced number of proper motions by comparison with minor axis fields, is still visible in our three fields, which reach $l \sim 10^\circ$. At the same time, we have explored the possible changes of the velocity (proper motion) ellipsoid in the fields as a function of the distance; similarly to the results of Clarkson et al (2008), we have not found a significant change in the tilt of the velocity ellipsoid.

All this suggests that the dynamics of the stars even at the location of our fields is dominated by bulge orbits. The latter argument in turn suggests, if we consider the anisotropies produced by the bar in the minor axis fields (see chapter 2) that what we observe should be part of the galactic bar. The importance of the extent of the bar can be related with the evolutionary stage of the bulge (e.g. Combes 2007; Athanassoula 2005) and thus the potential of this information for galactic models is invaluable. Our Schwarzschild model will include all the new data we have presented in the near fu-

ture. This will provide our model of new insights in the actual bulge structure, until now poorly constrained.

Finally, we have proven the technical feasibility of proper motions measurements with a mixture of cameras with different geometry for first and second epoch. Field 10-8 with its cluster NGC 6656 has provided us with a direct assessment of the accuracy of our proper motion procedure, which with a dispersion of 0.9 mas or $\sim 14 \text{ km/sec}$ corresponds to an excellent proof of the precision achieved by our procedure.

REFERENCES

- Anderson, J., & King, I.R. 1999, *PASP*, 111, 1095
Anderson, J., & King, I.R. 2000, *PASP*, 112, 1360
Anderson, J., & King, I.R. 2002, *ASPC*, 273, 167K
Anderson, J., & King, I.R. 2003, *AJ*, 126, 772
Anderson, J., & King, I.R. 2006, ACS Instrument Science Report 2006-01 (Batimore: STScI)
Athanasoula, E. 2005, *MNRAS*, 358, 1477
Ballero, S.K., Matteucci, F., Origlia, L., & Rich, R.M. 2007, *A&A*, 467, 123B
Benjamin, R.A., et al. 2005, *ApJ*, 630, L149
Binney, J., Gerhard, O.E., Stark, A.A., Bally, J., Uchida, K.I. 1991, *MNRAS*, 252, 210
Combes, F. 2007, *IAUS*, 235, 19C
Clarkson, W. et al. 2008, *ApJ*, 684, 1110
Cudworth, K.M. 1986, *AJ*, 92, 348
Dwek, E., et al. 1995, *ApJ* 445, 716
Englmaier, P., and Gerhard, O. 1999, *MNRAS*, 304, 512
Feltzing, S., & Gilmore, G. 2000, *A&A*, 355, 949
Fullbright, J.P., McWilliam, A., & Rich, R.M. 2007, *ApJ*, 661, 1152
Holtzman, J.A., Watson, A.M., Baum, W.A., Gillmair, C.J., Groth, E.J, Light, R.M., Lynds, R., & O'Neill, E.J., Jr. 1998, *AJ*, 115, 1946
Kozłowski, S., Woźniak, P.R., Mao, S., Smith, M.C., Sumi, T., Vestrand, W.T., and Wyrzykowski, Ł. 2006, *MNRAS*, 370, 435
Kuijken, K., Merrifield, M.R., *ApJ*, 443, L13
Kuijken, K., & Rich, R.M. 2002, *AJ*, 124, 2054
Kuijken, K. 2004, *ASP*, 317, 310K
Minniti, D. 1993, *IAUS*, 153, 315M
Minniti, D. 1996, *ApJ*, 459, 175
Rattenbury, N.J., Mao, S., Debattista, V.P., Sumi, T., Gerhard, O., & de Lorenzi, F. 2007, *MNRAS*, 378, 1165
Rattenbury, N.J., Mao, S., Sumi, T., Smith, M.C. 2007, *MNRAS*, 378, 1064

- Rich, R.M. 1988, *AJ*, 95, 828
- Rich, R.M. 1990, *ApJ*, 362, 604
- Rich, R.M., Reitzel, D.B., Howard, C.D., Zhao, H. 2007, *ApJ*, 658, L29
- McWilliam, A., Rich, R.M. 1994, *ApJS*, 91, 749
- Samus, N., Kravtsov, V., Pavlov, M., Alcaïno, G., and Liller, W. 1995, *A&A SS*, 109, 487
- Sadler, E.M., Rich, R.M., Terndrup, D.M. 1996, *AJ*, 112, 171
- Sumi, T., et al. 2004, *MNRAS*, 348, 1439
- Spaenhauer, A., Jones, B.F., Withford, E. 1992, *AJ*, 103, 297
- Schwarzschild, M. 1979, *ApJ*, 232, 236
- Schwarzschild, M. 1982, *ApJ*, 263, 599
- Soto, M., Rich, R.M., Kuijken, K. 2007, *ApJ*, 665, L31
- Terndrup, D.M., Rich, R.M., Sadler, E.M., 1995, *AJ*, 110, 1774
- Tonry, J., & Davis, M. 1979, *AJ*, 84, 10
- Vieira, K., et al., 2007, *AJ*, 134, 1432
- Zeballos, H., Soto, M., Kuijken, K, Rich, R.M. 2008, (in preparation)
- Zhao, H.S., Spergel, D.N., Rich, R.M. 1994, *AJ*, 108, 2154
- Zhao, H.S., Rich, R.M., & Spergel, D.N. 1996, *MNRAS*, 282, 175
- Zhao, H.S. 1996, *MNRAS*, 283, 149
- Zoccali, M., et al. 2006, *A&A*, 457, L1

Outlook

Nowadays, several projects attempt to unveil, in spite of its many difficulties, the stellar structure of the Milky Way. In this variety of studies, our own project plays a unique role; each important survey makes use of different tools in order to study the galactic structure, as we explain below for some of them.

Gaia is a mission of ESA which will attempt to complete a stereoscopic census of the Galaxy during the next decade. *Gaia* will deliver a vast and invaluable amount of data of the galactic surroundings of our Sun. The information collected will comprise spectroscopic and imaging observations up to $V \simeq 20 \text{ mag}$, which will produce accurate photometry, proper motions, radial velocities and distances. While the billion of stars with available information will provide an accurate map of the spatial and dynamic structure of the disk and halo, the bulge will have comparatively little information to be analyzed.

VVV Vista is another survey mapping the Galactic Structure. The methodology of Variables in the Via Lactea (VVV) consists on the systematic IR observation of central regions of the galactic bulge and an adjacent region of the mid-plane; this in order to study mainly variable stars. A catalogue of $\sim 10^6$ variable stars is expected, which will be complemented with data from HST, and SPITZER, and other surveys as MACHO, and OGLE. One of the main goals of this survey is the mapping of the 3-D bulge and disk structure derived from distance estimations using RR Lyrae, which are tracers of old populations. Furthermore, the study of variables will allow the study of possible remnants recently accreted by the Galaxy, which should show variables with unusual periods.

BRAVA, the Bulge Radial Velocity Assay (Rich et al, ApJ, 658, L29) is probably the most similar to our own project. *BRAVA* attempts to constrain the phase-space distribution function of the galactic bulge by means of a large-scale radial velocity survey of M giants stars. The radial velocity results of *BRAVA* are compared with Zhao's bulge model (Zhao 1996, MNRAS, 283, 149), which allows to study the main orbit families supporting the bar/bulge structure.

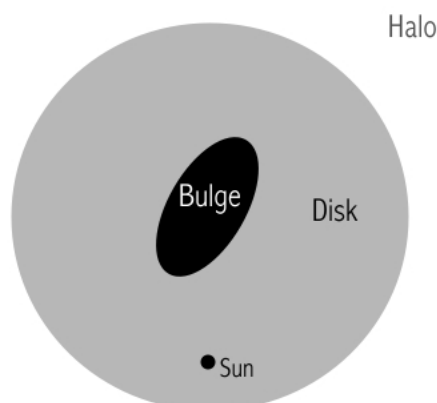
Our own project thus differs from previous surveys, targeting a more general stellar population; stars identified as bulge population through their proper motions in the color-magnitude diagram. Our project, on the other hand, focuses only in the bulge, while *GAIA* and *VVV* have the whole galactic structure as scope. Similar to *BRAVA*'s approach, we attempt to constrain the phase-space, but our choice provides a higher dimensionality since we combine radial velocities and proper motions. In addition, our Schwarzschild's model, taking advantage of today's computational power, is run for a

grid of models with a range of bar parameters. Thus, not only the main orbit families in the bulge are studied, but also main structural parameters of the galactic bulge, as the bar pattern speed, and bar inclination. This project, is still on-going, new fields in the far side of the bar/bulge will considerably increase the number of proper motions and radial velocities measured. Similarly, the overall robustness of our Scharschild's model will be improved with the new data, providing a realistic picture of the galactic bulge in the context of dynamics.

Nederlandse samenvatting

DIT proefschrift gaat over de kinematica van de galactische “bulge”, ofwel over de bewegingen van de sterren in het centrum van onze Melkweg. Het centrum van de Melkweg is een actief onderzoeksgebied en vele studies hebben reeds bijgedragen aan een zo nauwkeurig mogelijke beschrijving van deze belangrijke component van de Melkweg. De eerste beschrijvingen van de Melkweg waren voornamelijk filosofisch van aard, voornamelijk omdat goede astronomische waarnemingen niet voor handen waren. Ook waren religieuze concepten van het universum vaak een onderdeel van de beschrijvingen. De modellen van Thomas Wright (1711–1786) en Immanuel Kant (1724–1804) uit de achttiende eeuw zijn hier goede voorbeelden van. William Herschel (1738–1822) begon met het toetsen van melkwegmodellen aan de hand van echte metingen. Herschel baseerde het eerste empirische model van de Melkweg op tellingen van sterren en maakte gebruik van een aantal hypothesen die tot aan de twintigste eeuw niet weerlegd konden worden. Aan het begin van de twintigste eeuw waren er verschillende modelbeschrijvingen van de Melkweg in omloop, waaronder die van Harlow Shapley and Jacobus Kapteyn. Deze controversiële modellen, die qua afmeting wel tienmaal verschilden, hielden de sterrenkundige gemeenschap lange tijd in hun greep. De modellen waren namelijk moeilijk te testen met name door de gebrekkige waarnemingen, de onduidelijkheid over de zogenaamde “spiraalnevels” (deze bleken uiteindelijk niet tot onze Melkweg te behoren, maar waren op zichzelf ver weggelegen melkwegstelsels), en doordat de absorptie van sterlicht door stof (in de sterrenkunde aangeduid met “extinctie”) werd onderschat.

Vanaf 1927 begon zich echter een consistent beeld van de Melkweg te vormen, met name dankzij de ontdekkingen van Hubble, Oort en Lindblad. Zij zagen in dat zowel de Melkweg als de vele spiraalnevels op zichzelf staande sterrenstelsels waren, zoals reeds door Shapley was voorspeld. Opeenvolgende ontdekkingen zoals de sterclassificaties van Walter Baade, die verschillende evolutionaire fasen van sterren ontdekte, en de ontdekking van de 21-cm spectraallijn van waterstof, maakten het mogelijk om onze kennis van de Melkweg enorm uit te breiden. Ons huidige beeld van de Melkweg ziet er als volgt uit (zie afbeelding 7.1). In het centrum bevindt zich de populatie van bulge-sterren. Er is relatief minder gas en er worden minder nieuwe sterren gevormd vergeleken met de rest van de Melkweg. De bulge is omgeven door een spiraalvormige schijf van gas, stof en sterren. Het gas in de spiraalarmen voedt nieuwe sterformingsgebieden. De bulge en de schijf zijn omgeven door een langzaam roterende “halo”, waar zich de oudste sterren van de hele Melkweg bevinden. Deze sterren worden gekenmerkt door een gebrek aan zware elementen (metalen). Desalniettemin is



Figuur 7.1: Schematisch overzicht van de verschillende onderdelen van de Melkweg.

onze huidige beschrijving van de Melkweg nog lang niet compleet. Vooral de hevige extinctie in de richting van het centrum van de Melkweg maakt het moeilijk om de precieze structuur te zien. Er zijn aanwijzingen dat de bulge door een balkvormige structuur is omgeven (Engels: “bar”), maar de precieze details zoals de afmeting en de massa ervan zijn niet bekend. De extinctie kan met behulp van twee methoden omzeild worden. Ten eerste kunnen waarnemingen worden gedaan in het infrarood, waar de invloed van de extinctie veel kleiner is. Ten tweede kan men gebruik maken van speciale gezichtslijnen door de Melkweg waar de extinctie relatief klein is (Engels: “low extinction windows”). Het project beschreven in dit proefschrift maakt gebruik van de laatste methode.

Dit proefschrift maakt deel uit van een project waarin geprobeerd wordt om de structuur van de bulge bloot te leggen door middel van het bestuderen van de kinematica van sterren in gebieden met een relatief kleine extinctie. We hebben de radiële snelheid en eigenbeweging van een groot aantal sterren verspreid over de bulge verzameld om zo de fase-ruimte verdeling van de bulge te kunnen bepalen. Ook hebben we een zelf-consistent Schwarzschild model geconstrueerd dat de verdeling van sterbanen in het centrum van de Melkweg nauwkeurig beschrijft.

In Hoofdstuk 2 presenteren we ~ 3200 nieuwe radiële snelheidsmetingen in het galactisch centrum, gebaseerd op waarnemingen van de spectra van sterren langs 6 gezichtslijnen met een relatief kleine extinctie. Deze metingen werden gedaan met de VIMOS-IFU camera op de Very Large Telescope (VLT) in Chili. Het is vaak moeilijk om de contributies van verschillende individuele sterren, die vaak dichtoepengepakt staan, te identificeren in de spectraal waarnemingen. De spectraal waarnemingen werden daarom gecombineerd met opnames waarin de posities van de afzonderlijke sterren nauwkeurig konden worden bepaald. Deze opnames waren eerder gemaakt met de Wide Field and Planetary Camera 2 (WFPC2) camera die zich aan boord bevindt van de Hubble Ruimteteleskoop (HST). De zo verkregen positionele en spectrale informatie voor een groot aantal sterren werd met behulp van een deconvolutie algoritme omgezet in de eigenlijke snelheidsmetingen.

Het resultaat van dit proces is een spectrum voor elke ster gezien in de HST afbeelding. De nauwkeurigheid waarmee we met deze techniek radiële snelheden kunnen bepalen bedraagt zo'n 30 kilometer per seconde, welke veel kleiner is dan de waargenomen dispersie in snelheden in het galactisch centrum (zo'n 110 kilometer per seconde) en dus voldoende is voor een studie van de dynamica (zie Hoofdstuk 4). In drie velden waargenomen langs de korte as van de Melkweg (*Sagittarius I*, *Baade's Window* en nabij *NGC 6558*) hebben we zelfs nog een stap verder kunnen gaan door de nieuwe radiële snelheden te combineren met de eigenbewegingen gemeten door Kuijken & Rich (2002, *AJ*, 124, 2054). Zodoende hebben we dus de beschikking over een aantal sterren in elk veld met goed bepaalde, drie-dimensionale snelheidsinformatie. Deze laatste categorie sterren laat heel duidelijk een verschil zien in de snelheden van sterren die tot verschillende populaties in het kleur-magnitude diagram behoren. Sterren behorende tot de hoofdreeks, het afbuigpunt, en de rode reuzen tak hebben een duidelijke afwijking wat een directe indicatie is voor triaxialiteit (ofwel: niet-axisymmetrisch en dus een hogere graad van complexiteit) van de galactische bulge.

In tegenstelling tot bovengenoemde sterpopulaties vinden we dat de bewegingen van heldere, blauwe hoofdreekssterren voorbij het afbuigpunt duidelijk niet overeenkomen met de populaties in de bulge. We concluderen dus dat deze blauwe hoofdreekssterren behoren tot de populaties van sterren in de schijf van de Melkweg. Ook vinden we dat de mate van triaxialiteit minder wordt naarmate men zich verder vanaf het vlak van de Melkweg bevindt (zoals in het veld bij *NGC 6558*). Dit betekent dat we een belangrijke aanwijzing hebben gevonden voor de afmeting en de invloed van het zwaartekrachtveld van de balk in de binnenste kiloparsec in de Melkweg.

De studie van Spaenhauer et al. (1992, *AJ*, 103, 297) was een van de eerste die een betrouwbare catalogus van de eigenbewegingen van sterren in het galactisch centrum presenteerde. Zij maakten gebruik van fotografische platen met opnamen van sterren genomen met tussenpozen van enkele tientallen jaren in de richting van *Baade's Window* en bepaalden eigenbewegingen voor 432 sterren. Latere studies maakten gebruik van deze catalogus om de metaalabundanties van de sterren te bepalen met behulp van lage resolutie spectroscopie (Terndrup et al. 1995, *AJ*, 110, 1174; Sadler et al. 1996, *AJ*, 112, 171). In Hoofdstuk 3 hebben we dit monster van sterren nader bestudeerd, omdat het behalve drie-dimensionale snelheden ook abundanties bevat. De originele lage resolutie abundanties werden eerst opnieuw geïjkt volgens de hoge resolutie abundantie schaal van Fulbright et al. (2006, *ApJ*, 636, 821). Vervolgens hebben we de bewegingen van sterren geselecteerd op grond van verschillende criteria vergeleken. Het resultaat was dat we een significante afwijking vonden in de bewegingen van sterren behorende tot de populatie van sterren met een relatief hoge abundantie ($[Fe/H] > -0.5$), terwijl deze niet werd waargenomen in de populatie van sterren met een lage abundantie. Nadere inspectie liet zien dat de verandering in de kinematica van de sterren abrupt optreedt nabij een abundantie van $[Fe/H] = -0.5$, en dat deze verandering consistent is met de overgang van snelheden in een isotroop, oblaat lichaam naar die in een balkvormig lichaam. Ook vonden we een zwakke trend dat de snelheidsdispersies in de verticale richting afnemen naarmate de abundanties van de sterren toenemen.

In Hoofdstuk 4 presenteren we ons nieuwe Schwarzschild model voor het centrum

van de Melkweg. De Schwarzschild techniek houdt het volgende in. Eerst berekenen we een groot aantal representatieve sterbanen dat consistent is met een bepaalde verdeling van de sterren in een model voor de Melkweg. Vervolgens proberen we de waargenomen snelheden van sterren te verklaren door middel van lineaire combinaties van sterbanen uit het Schwarzschild model. Ons model reproduceert de waargenomen verdelingen van eigenbewegingen en afstanden (bepaald met behulp van de zogenaamde fotometrische parallax methode) voor sterren van de hoofdreeks en het afbuigpunt geselecteerd uit de drie stervelden in de richting van de korte as van de Melkweg. Behalve de eigenbewegingen en afstanden (parallaxen) is het belangrijk om ook de dichtheidsverdeling van de sterren te weten. Deze dichtheidsverdeling werd verkregen door gebruik te maken van de opnamen van het centrum van de Melkweg gemaakt met het Diffuse Infrared Background Experiment (DIRBE) aan boord van de Cosmic Background Explorer (COBE; Arendt et al. 1994, ApJ, 425, L85; Weiland et al. 1994, ApJ, 425, L81). We gebruikten hierbij verschillende methoden om de tweedimensionale COBE kaarten te deprojecteren in de drie ruimtelijke dimensies van de Melkweg.

In Hoofdstuk 4 hebben we een model gekozen dat het beste overeenkwam met de waarnemingen volgens de Schwarzschild methode. Dit simpele model van de Melkweg bestaat uit een balk, een schijf en een kern. We hebben 25 Schwarzschild modellen getoetst, waarbij elk model een verschillende combinatie had van twee belangrijke parameters die de balk beschrijven, de systematische balksnelheid, Ω_b , en de inclinatiehoek van de balk, ϕ_{balk} . De resultaten toonden aan dat voor een balk met een systematische balksnelheid van 30–40 km sec⁻¹ kpc⁻¹ er oplossingen bestaan voor balk inclinaties van zowel 0° als 40°. Om de onzekerheid in deze mogelijkheden op te lossen, hebben we de gegevens over de radiële snelheden uit Hoofdstuk 2 gebruikt. Dit leidde tot onze beste oplossing voor het balkmodel en deze komt overeen met recente metingen aan de galactische balk die gebruik maakten van andere technieken (zie bijvoorbeeld Benjamin et al. 2005, ApJ, 630, L149). Onze beste modelbeschrijving van de balk heeft echter tot gevolg dat we een significant aantal aan chaotische banen verwachten. De totale massa aan sterren dat zich in deze chaotische banen beweegt bedraagt een aanzienlijke fractie van de totale massa. Het is momenteel onduidelijk of deze voorspelling slechts een onjuiste bijwerking van ons model is, of dat deze de werkelijke situatie in de Melkweg beschrijft. Dit moet in de toekomst uitgezocht worden met behulp van betere waarnemingen.

Tot slot presenteren we in Hoofdstuk 5 zo'n 11000 nieuwe eigenbewegingen voor drie velden op positieve lengtegraden: *Veld 4-7* gelegen op een galactische lengte- en breedtegraad van (3.58°, -7.17°), *Veld 3-8* gelegen op (2.91°, -7.96°) en *Veld 10-8* op (9.86°, -7.61°). Deze eigenbewegingen gemeten over een periode van 8 tot 9 jaar zijn berekend met behulp van een aanpassing van de methode van Anderson & King (2000, PASP, 112, 1360). Deze methode is oorspronkelijk bedoeld voor waarnemingen met de WFPC2 gedaan volgens een speciaal stappenpatroon. Dit stappenpatroon, waarbij verschillende opnamen van hetzelfde veld worden gemaakt door steeds de camera tussen de opnamen in een klein stukje te verschuiven, zorgt voor een betere bemonstering van het radiële lichtprofiel van sterren in de opnamen. Dit heeft het voordeel dat

de posities van de sterren en dus hun bewegingen tussen twee perioden nauwkeuriger bepaald kunnen worden. Onze aanpassing van deze methode maakt gebruik van een analytisch model en de lichtverdelingsfunctie gemeten voor een groot aantal sterren in de opnamen gemaakt zonder stappenpatroon uit de eerste periode om zo toch nauwkeurige posities en eigenbewegingen te kunnen bepalen. Deze studie van de eigenbewegingen vertoont een grote mate van overeenkomst met die in de stervelden langs de korte-as van de Melkweg (Kuijken & Rich 2002). Ook vertonen de nieuwe velden een gradient in de richting van de gemiddelde eigenbewegingen ten opzichte van hoofdreekssterren, wat veroorzaakt wordt door de intrinsieke rotatie van de bulge. Dit laatste betekent dat zelfs ter hoogte van de lengtegraad van de nieuwe velden zich een significante fractie aan bulge sterren moet bevinden. Zoals verwacht ziet men ook dat de snelheidsdispersie van verder weggelegen sterren kleiner is, maar een significante verandering in de bewegingen als functie van afstand van het centrum werd niet gevonden. Dit is consistent met een voorgaande studie naar de eigenbewegingen van sterren in *Sagittarius I* met behulp van de Advanced Camera for Surveys, die zich ook aan boord van de Hubble telescoop bevindt (Clarkson et al 2008, ApJ, 684, 1110).

De nieuwe informatie over de bewegingen van sterren gevonden op grond van de velden bestudeerd in dit proefschrift heeft geleid tot een beter begrip van het galactisch centrum. Een vervolgstudie naar de kinematica van sterren aan de andere, verder weggelegen kant van de balk ($l < 0$) staat momenteel in de wacht tot na de geplande reparatie van de Hubble Ruimtetelescoop in 2009. Het is te verwachten dat dit uiteindelijk zal leiden tot een nog completer beeld van de interne kinematica van het galactisch centrum en de balk.

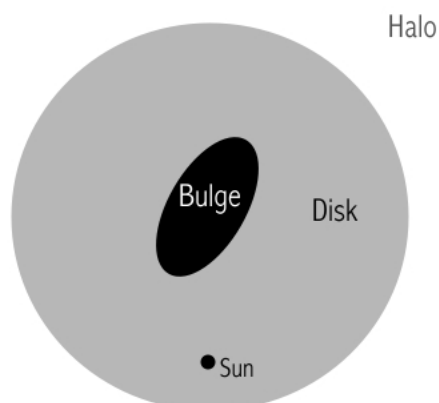
Resumen en Español

ESTA tesis es sobre la cinemática de nuestro bulbo galáctico; el movimiento de cúperpos estelares en el centro de la Vía Láctea. Durante una considerable cantidad de años el bulbo galáctico ha sido el foco de innumerables estudios, los cuales han producido como resultado el conocimiento de las características estructurales que reconocemos hasta el día de hoy.

Los primeros modelos de la Vía Láctea, debido principalmente a la ausencia de observaciones adecuadas, fueron eminentemente filosóficos. No obstante, con regularidad y en concordancia a sus tiempos, tales modelos incluían una concepción religiosa del Universo. Tal es el caso de los modelos formulados por Thomas Wright o Immanuel Kant durante el siglo XVIII. No fue sino hasta William Hershel que datos reales fueron introducidos a los modelos de nuestra galaxia. Hershel usando cuentas estelares formuló el primer modelo empírico de la Vía Láctea, el cual se basó en varios supuestos que no fueron probados si no hasta el siglo XX. Fue precisamente durante el siglo recién pasado que otros dos modelos de la Vía Láctea mantuvieron una fuerte controversia en la comunidad astronómica; los modelos de Kapteyn y Shapley. Ambos modelos diferían en un factor de 10 en el tamaño de nuestra galaxia. Sin embargo, la visión incompleta de la astronomía que se tenía en esos tiempos, que incluía el desconocimiento de la naturaleza de nebulosas espirales y el desprecio de los posibles efectos de la extinción, no permitieron la hegemonía de ninguno de estos modelos por sobre el otro si no hasta 1927. El modelo entonces asumido para la Vía Láctea, gracias a los descubrimientos de Hubble, Oort y Lindbland, consideraba nuestra galaxia como un par de muchas nebulosas espirales conocidas, y por consiguiente era más similar a las ideas de Shapley. Descubrimientos subsecuentes como la distinción entre poblaciones estelares de Walter Baade, quien distinguió entre las diferentes historias de las estrellas, y la emisión de Hidrógeno neutral en su línea con 21-cm de longitud de onda, mejoraron considerablemente el entendimiento de la naturaleza de nuestra galaxia.

Así, el modelo actual de nuestra galaxia reconoce varias componentes (ver Fig. 7.2). En términos generales, este modelo incluye un bulbo central con escasa presencia de gas y formación estelar. Este bulbo es rodeado por un disco que típicamente posee mayores índices de formación estelar que el bulbo, y gas en los brazos alimentando asociaciones de estrellas jóvenes. El bulbo y disco a su vez están rodeados por una componente esférica rotando lentamente, el halo. Es el halo donde las estrellas más viejas y pobres en metales se encuentran.

No obstante todo lo anterior, los modelos actuales de la Vía Láctea son aún incompletos. En particular, la estructura del centro de nuestra galaxia permanece velada a



Figuur 7.2: Diagrama esquemático de los componentes de la Vía Láctea.

observaciones ópticas debido a la alta extinción en el plano galáctico. Existe fuerte evidencia que el bulbo de la galaxia es en realidad una barra, sin embargo las dimensiones de tal barra no están en absoluto definidas. Para resolver las dificultades impuestas por la alta extinción hacia el bulbo galáctico, normalmente dos alternativas se presentan, observaciones en el infrarrojo cercano, donde se sabe la extinción es menor, y la observación de “ventanas” de baja extinción. Este proyecto se basa en la segunda alternativa.

Esta tesis, es parte de un proyecto que intenta develar la estructura del Vía Láctea a través del estudio de la cinemática de estrellas en ventanas de baja extinción del bulbo. A fin de efectivamente definir la función de distribución del espacio de fase del bulbo, hemos medido un considerable cantidad de velocidades radiales y movimientos propios en varias “ventanas” de baja extinción del bulbo. Adicionalmente, hemos desarrollado un modelo de Schwarzschild auto-consistente para estudiar la distribución de órbitas del bulbo.

En el **Capítulo 2** reportamos ~ 3200 nuevas velocidades radiales, las cuales han sido obtenidas en 6 ventanas de baja extinción del bulbo galáctico. Nuestras velocidades radiales fueron obtenidas usando la cámara VIMOS-IFU, la cual permitió la construcción de cubos de velocidades radiales en cada caso. La importancia de tales cubos de datos está relacionada con la existencia previa de imágenes del *Telescopio Espacial Hubble* (HST) en aquellos campos, obtenidas inicialmente de los archivos de HST. Los cubos de VIMOS-IFU, combinados con las posiciones estelares de las imágenes de HST, han sido usadas para separar la información espectral de cada estrella en un algoritmo de deconvolución. Los resultados de este proceso son los espectros estelares en las posiciones definidas por las imágenes de HST. Las velocidades radiales así obtenidas típicamente han alcanzado precisiones de $\sim 30 \text{ km/sec}$, lo cual es varias veces menor que la dispersión de velocidades del bulbo galáctico $\sim 110 \text{ km/sec}$, y por lo tanto apropiado para estudios en dinámica estelar. Aplicaciones de dinámica estelar son vistas en el capítulo 4.

En el caso de los tres campos cercanos a semi-eje menor de nuestra galaxia *Sagitario*

I, *La ventana de Baade*, y *near NGC 6558* ha sido posible avanzar adicionalmente y combinar las nuevas velocidades radiales con los movimientos propios de Kuijken & Rich (2002, AJ, 124, 2054). En estos casos, un pequeño subgrupo de estrellas por campo con cinemática 3-D ha sido construido. Los resultados de esta sub-muestra de estrellas claramente destaca una fuerte distinción entre la cinemática de las diferentes poblaciones presentes en cada diagrama color-magnitud (CMD). Secuencia principal (MS), punto de giro (turn-off), y la rama de gigantes rojas (RGB) muestran claramente la cinemática correspondiente con la triaxialidad del bulbo. Por el contrario, estrellas azules por sobre el punto de giro muestran cinemática consistente con el disco galáctico. Al mismo tiempo, se observa que esta traza de triaxialidad (i.e. la presencia de una barra) decrece a medida que nos alejamos del plano galáctico, siendo la más débil en el campo *near NGC 6558*. Lo último, otorga importantes pistas acerca de la verdadera extensión de la barra del bulbo, y la influencia del potencial de esta barra al interior de la galaxia.

El estudio llevado a cabo por Spaenhauer et al. (1992, AJ, 103, 297) fue uno de los primeros en obtener un catálogo de movimientos propios para estrellas del bulbo galáctico. El trabajo de Spaenhauer et al. utilizó placas fotográficas tomadas con varias décadas de diferencia para obtener 432 movimientos propios en una muestra de estrellas de la ventana de Baade. Esta muestra fue a su vez el punto de inicio de estudios posteriores que determinaron, por medio de espectros de baja resolución, abundancias en muchas de las estrellas originalmente medidas (Terndrup et al. 1995, AJ, 110, 1174; Sadler et al. 1996, AJ, 112, 171). En el **Capítulo 3** hemos explorado esta muestra, la cual además de contar con una cinemática en tres dimensiones bien definida, posee abundancias con una calibración confiable. Las abundancias originales provenientes de espectros de baja resolución fueron recalibradas usando una escala de abundancias obtenidas a partir de espectros de alta resolución (Fulbright et al. 2006, ApJ, 636, 821). Así por medio de esta muestra con cinemática en tres dimensiones bien definida y abundancias calibradas es que hemos estudiado los signos de triaxialidad a través de los elipsoides de velocidades en varias selecciones distintas. En primera instancia una fuerte señal de triaxialidad, la presencia de una barra, ha sido detectada para las estrellas más ricas en metales. Al analizar toda la muestra detalladamente en función de la metalicidad, una súbita transición en la cinemática es observada alrededor de $[Fe/H] = -0.5 dex$. Esta transición va desde la cinemática esperada en una distribución de estrellas de disco, a la de una barra. Al mismo tiempo, una tendencia más débil hacia dispersiones de velocidades más bajas (σ_b) a medida que las abundancias aumentan fue encontrada.

El **Capítulo 4** presenta nuestros avances en el desarrollo de un modelo de Schwarzschild para la Vía Láctea. Los modelos de Schwarzschild están basados en el cálculo de una librería de orbitas consistente con una distribución de densidades volumétrica, observables son entonces ajustados con una combinación lineal de las orbitas en la librería con todos los coeficientes positivos ($w_i \geq 0$). Nuestro modelo ha sido construido para reproducir la distribución de movimientos propios y paralajes fotométricos en los tres campos de nuestro proyecto cercanos al eje menor galáctico. En cada campo se ha seleccionado una sub-muestra de estrellas de secuencia principal y punto de giro que es incluida en el ajuste. Además de los movimientos propios y paralaje fotométrico

un perfil de densidades ha sido fundamental para obtener un set de restricciones, éste perfil ha sido construido a partir de deproyecciones de imágenes del bulbo galáctico del experimento COBE-DIRBE (Arendt et al. 1994, ApJ, 425, L85; Weiland et al. 1994, ApJ, 425, L81). En el capítulo 4 comenzando de una deproyección analítica con varios parámetros libres, hemos escogido un único modelo de barra el cual completa el set de restricciones a ajustar. El modelo desarrollado incluye entonces una barra, un disco, y una sobredensidad central. Así este modelo del bulbo fue usado para construir un potencial consistente por medio de una expansión multipolar, donde cada órbita (calculada a partir del potencial) fue integrada aproximadamente ~ 10000 periodos rotacionales. Un set de 25 modelos de Schwarzschild auto-consistentes han sido calculados, cada uno correspondiente a una combinación diferente de dos importantes parámetros de la barra, velocidad de rotación de la barra Ω_b , y ángulo de la barra ϕ_b . Resultados de este set de modelos muestran una aparente degeneración para el valor más bajo de χ^2 , que aparece para barras girando a $30 - 40 \text{ km sec}^{-1} \text{ kpc}^{-1}$ y con inclinaciones de 0° a 40° . Para discernir entre valores con similares χ^2 hemos introducido la información de velocidades radiales aparecida en el capítulo 2. Incluyendo tal información, hemos podido establecer que nuestro mejor modelo de barra es consistente con recientes determinaciones por diferentes métodos (e.g. Benjamin et al. 2005, ApJ, 630, L149). También, nuestro mejor modelo de barra, produce un significativo número de órbitas estocásticas, las cuales corresponden a un alto porcentaje de la masa total.

Finalmente, en el **Capítulo 5** reportamos ~ 11000 movimientos propios nuevos para nuestros campos en longitudes positivas. Field 4-7 ($l, b = 3.58^\circ, -7.17^\circ$), Field 3-8 ($l, b = 2.91^\circ, -7.96^\circ$), y Field 10-8 ($l, b = 9.86^\circ, -7.61^\circ$). Estos movimientos propios, calculados usando un tiempo de base entre primera y segunda época de 8-9 años, han sido fabricados usando una modificación del procedimiento de Anderson & King (2000, PASP, 112, 1360). Este proceso fue originalmente diseñado para trabajar en observaciones en WFPC2 con una patrón adecuado de desplazamiento (dithering). Por desplazamiento entendemos la observación consecutiva de imágenes desplazadas en fracciones de pixel que permiten resolver la carencia de puntos de muestreo al medir una PSF (Point Spread Function). La modificación del método original corrige los problemas derivados de la ausencia de imágenes con desplazamiento en la primera época de nuestros movimientos propios. Ésto es realizado por medio de un algoritmo que refina la PSF de las estrellas iterativamente en cada imagen comenzando desde una PSF analítica. Otra diferencia relevante entre estos movimientos propios y aquellos de los campos en el eje-menor galáctico, esta relacionado con los instrumentos usados en cada época. Mientras los campos en el eje-menor galáctico fueron observados en ambas épocas con el instrumento WFPC2, los movimientos propios en el capítulo 5 consisten de una combinación de WFPC2 y ACS WFC, para la primera y segunda época respectivamente. Este último detalle implicó varias modificaciones al procedimiento de movimientos propios. Los resultados de estos movimientos propios muestran una destacable similaridad con aquellos en los campos del eje-menor galáctico (Kuijken & Rich 2002). Los nuevos campos también muestran un gradiente perpendicular a la secuencia principal en el μ_l promedio, lo cual puede ser directamente relacionado con la rotación intrínseca del bulbo. Lo último significa que incluso a las longitudes de los

nuevos campos existe una fracción considerable de estrellas del bulbo. Consistentemente, un efecto de distancia puede ser observado en las dispersiones de velocidades, las estrellas más lejanas tienden a mostrar dispersiones más pequeñas. Una búsqueda más específica de cambios en el elipsoide de velocidades como función de las distancias no produjo resultados positivos, lo cual también es apoyado por otros estudios previos (e.g. Clarkson et al. 2008, ApJ, 684, 1110). Un estudio complementario, el cual tiene como objetivo el lado lejano de la barra en el bulbo ($l < 0$), está en espera de la reparación de HST. Estos últimos datos se esperaban mejorarán significativamente el modelo general y la visión de la cinemática interna del bulbo/barra. La información provista en nuestros cuatro campos en el lado cercano de la barra y el eje-menor galáctico proveen de información única para los nuevos modelos del bulbo galáctico.

Curriculum Vitae

I was born on February 14, 1979, in Santiago, the Chilean capital city. My childhood, surrounded by many cousins first, and by my younger siblings, was spent between the many activities of the Salesian School I attended, and unforgettable summers at the very south of Chile. There was a lot of fishing and excursions in those years, regularly to places where the sight of other people was more than scarce. The books in my house helped me then to develop a special fondness for encyclopedias, Earth Sciences books (my mother was a History and Geography teacher), Julio Verne's novels, and many others.

During High School I studied in the Salesian technical school which allowed me to study electronics and later work during a couple of summers at the IBM. I started to study Physics at the Universidad de Chile in 1997, where in my final year I worked on the low-energy particle accelerator of the University. During 2002 I started my Master at Universidad Católica. My Master thesis, under the supervision of Dr. Dante Minniti, was entitled *Spectroscopic Characterization of Bulge Microlensing events*, and was my first professional approach to the topics of Galactic Structure, and Stellar Dynamics. I started my PhD in Leiden in September of 2004, where I have pursued the study of the stellar structure of the Galactic Bulge through radial velocities and proper motions. During my years in Leiden I have participated of many astronomical gatherings, summer schools in Dwingeloo (The Netherlands) and Heidelberg (Germany), conferences in Blackenberge (Belgium), Terschelling (The Netherlands), La Palma (Spain), Prague (IAU General Assembly, Czech Republic), and Oxford (UK).

Acknowledgments

I remember vividly my first day as a PhD student at the Sterrewacht; the stress, and the stiff neck produced by the uncertainty of the enterprise I was about to start. Now, some years later, I would like to express my gratitude to those who helped me both to overcome the fear, and to enjoy my years at Leiden.

I would like to start thanking to Dr. Dante Minniti, Dr. R. Michael Rich and Dr. HongSheng Zhao, for showing me how much fun and interesting astronomy can be. The Leiden Staff also played an important role in my research the last years, with their diligent and efficient work they provided me the best environment to produce science.

Friends and family have been the most relevant part during my thesis work, with their love and companionship they gave me the strength to continue and to struggle till the end. Friends as Cyrill, Anne, Hugo, Tri, Rafael, Edouard, Marcelo, Claudio, Nienke & Joop, and Isa made me feel always at home; thanks for your sharp comments and interesting conversations. I have to thank specially to my friend Roderik, an excellent comrade who in addition has translated the summary of this thesis to Dutch. I am also grateful to Marcela and her big heart. Fernanda, eternal hostess of many gatherings; Arjan & Yannira whose friendship is priceless; and probably many others who my febrile mind does not recall while I write these lines.

Finally, the deepest gratitude goes to my family, to my wife Deisy for being as she is, and our little Agustina, for being pure and concentrated happiness everyday. Also to my brother and sisters, Manuel, Ximena, Rosa, Ana, and our father and mother, Mario and Ana Maria, always with me in spite of the distance.